MECHANICALLY MEDIATED GROWTH AND REMODELING OF COLLECTING LYMPHATIC VESSELS

A Dissertation
Presented to
The Academic Faculty

by

Mohammad S. Razavi

In Partial Fulfillment
of the Requirements for the Degree
Doctor of Philosophy in Bioengineering in the

Georgia Institute of Technology
December 2019

MECHANICALLY MEDIATED GROWTH AND REMODELING OF COLLECTING LYMPHATIC VESSELS

Approved by:

Dr. Rudolph L. Gleason, Jr., Advisor
School of Mechanical Engineering
Georgia Institute of Technology

Dr. Wei Sun
School of Biomedical Engineering
Georgia Institute of Technology

Dr. J. Brandon Dixon, Co-Advisor
School of Mechanical Engineering
Georgia Institute of Technology

Dr. David C. Zawieja
Department of Medical Physiology
Texas A&M University

Dr. Alexander Alexeev
School of Mechanical Engineering
Georgia Institute of Technology

Date Approved: Oct 3 2019

To my parents

ACKNOWLEDGEMENTS

I would like to thank my parents for their everlasting love and support. I would also like to thank Dr Rudy Gleason and Dr. Brandon Dixon, my committee members, and my lab mates for their many helpful insights.

TABLE OF CONTENTS

LIST OF TABLES

LIST OF FIGURES

LIST OF SYMBOLS AND ABBREVIATIONS

AHA	American Heart Association
AMP	Amplitude
cm	Centimeter
ECM	Extracellular matrix
EDD	End-diastolic diameter
EF	Ejection fraction
eNOS	Endothelial nitric oxide synthase
ESD	End-systolic diameter
H&E	Hematoxylin and eosin
FPF	Fractional pump flow
FREQ	Frequency
μg	Microgram
μL	Microliter
mL	Milliliter
mm	Millimeter
mmHg	Millimeters of mercury
NOS	Nitric oxide synthase
NIR	Near-infrared
PSS	Physiologic saline solution
SEM	Standard error of the mean
SHG	Second harmonic generation
SMA	Smooth muscle actin

SMC	Smooth muscle cell
SNP	Sodium nitroprusside
F	Deformation gradient
T	Cauchy stress tensor
C	Right Cauchy-Green strain tensor
I	Identity matrix
W	Strain energy function
α_k^1	k_{th} fiber family angle
C	Neo-Hookean material parameter
C_k^1	First k_{th} family material parameter
C_k^2	Second k_{th} family material parameter
p	Lagrange multiplier
P	Pressure
λ_θ	Circumferential stretch
λ_z	Axial stretch
μ	Kinematic viscosity
ρ	Fluid density
g	Gravitational acceleration
3D	3-dimensional

SUMMARY

Lymphatic dysfunction plays a key role in pathologies such as immune disorders, infection, cancer, obesity, and cardiovascular disease; regarding the latter, lymphatic dysfunction may exacerbate edema in myocardial infarction (MI) and chronic heart failure. Secondary lymphedema is a progressive and debilitating disease characterized by fluid retention and tissue swelling that can arise due to dysfunction in lymphatic pumping. Secondary lymphedema is a common complication in breast cancer treatment where the surgical removal of lymphatic vessels/lymph nodes can induce overloads that triggers lymphatic pathologies that can present months or even years after surgery. Although the local mechanical environment is known to regulate lymphatic function, the role of sustained mechanical overloads (e.g., high pressure and high flow) in lymphatic dysfunction has yet to be established. Towards this end, our long-term goal was to develop a mechanistic understanding of mechanically-mediated growth and remodeling (G&R) of collecting lymphatic vessels in health and disease and to ultimately identify novel therapeutic interventions to minimize the risk of occurrence, severity, or complications of lymphatic dysfunction. This PhD thesis focuses on developing a novel rat tail model to study lymphatic G&R and to employ a combined experimental-computational approach to quantify the modes by which sustained high pressure and high flow compromise the normal function of the lymphatic system via maladaptive remodeling. First, we introduced and used a novel rat tail model to study the effect of mechanical loads (specifically axial stretch) on the lymphatic contractility. Second, we developed a computational framework to study lymphatic pumping in the context of a lymphangion chain. Lastly, we developed and tested

the feasibility of a novel lymphatic ligation model to study lymphatic remodeling post-surgery. Lastly, the methods and results from this study can pave the way for future studies of lymphatic remodeling in health and disease.

CHAPTER 1. INTRODUCTION AND BACKGROUND

1.1 Lymphatic function and physiology.

The lymphatic system found in most soft tissues is fundamental to maintaining tissue fluid balance, immune function and absorption and transport of lipids [1]. A hierarchical architecture enables the lymphatic system to transport lymph from interstitial spaces through specialized lymphatic capillaries, towards pre-collecting, prenodal and postnodal collecting vessels that return lymph back to the great veins [2]. Since the lymphatic system does not have a central pump to propel fluid within the network, collecting lymphatic vessels have been equipped with specialized smooth muscle cells capable to generate intrinsic contractions. In addition, intraluminal valves that separate each functional unit, called a lymphangion, ensure unidirectional flow within the network. Since collecting lymphatic vessels serve as both a conduit and a pump, modulation of lymphatic pumping is subject to chemical [3–6], mechanical [7–10] as well as electrical regulations [11–14]. Mechanical regulation is known to be an integral part of spontaneous contractions of lymphatic vessels [10,15–17]. Generally, increases in pressure/stretch initiate spontaneous contractions while increases in flow/shear inhibit contractions[18]. However, there exists a regional heterogeneity in lymphatic structure and function to adapt to particular flow and pressure conditions in different regions[17].

Fluid shear and pressure forces have well-established roles in the regulation of lymphatic function[2,4,8–10]. It is well known that fluid shear stress modulates frequency and amplitude of phasic contractions as well as endothelial-dependent nitric

oxide synthesis [3]. In addition, it has been suggested that shear stress regulates the complex process of lymphatic vessel and intraluminal valve maturation and development [19,20]. Similarly, transmural pressure can regulate frequency and amplitude of contractions, lymphatic tone as well as active length-tension relationships. Further, transmural pressure modulates valve gating which dictates unidirectional flow within lymphatic vessels[21]. Although lymphatic vessels respond to alterations of flow and pressure overload to maintain normal function, prolonged overloads can trigger maladaptive remodeling which compromises normal function. The enlargement of collecting lymphatic vessels in the presence of growth factors such as VEGFC has been attributed to increased lymph flow[22]. Additionally, histological and morphological changes in collecting lymphatic vessels such as the growth of collagen fibers, phenotypic change in lymphatic MCs, sclerosis and lumen narrowing have also been reported to associate with intraluminal pressure and flow overloads[23].

1.2 Lymphatic dysfunction and Lymphedema.

A dysfunctional lymphatic system not only causes pathologies but it can also exacerbate other diseases. Lymphatic impairment has been implicated in numerous diseases such as atherosclerosis [24–26], myocardial infarction[27–29], heart failure [30], lung diseases [31,32], cancer [22,33–35] and most of the inflammatory [36,37] and edema related pathologies[38,39]. Secondary lymphedema is a chronic, debilitating condition due to an impairment of lymphatic function during cancer treatment. Since an impaired lymphatic system is not capable to effectively transport lymph, fluid retention and tissue swelling occur in patients afflicted with lymphatic pathologies. Recent reports have suggested that blockade of lymph flow due to

surgical procedures as well as high lymph drainage due to edema and fluid retention can play an important role in the pathogenesis and progression of lymphatic disorders [40,41]. Insufficiency of the lymphatic system is mainly attributed to impaired intrinsic contraction of lymphatic vessels to effectively transport lymph. Additionally, other complications such as fat and protein accumulation, increase in adipose tissue and immunosuppression are known to be associated with an impaired lymphatic system[38,42,43]. Since the lymphatic system is a dynamic complex that adapts to alteration in working conditions, remodeling of lymphatic vessels is regarded as an important factor that causes lymphatic dysfunction [35,44,45].

1.3 Current state of animal models in lymphatic research

To study lymphatic function a variety of both large animals and small animal models have been used [46–48]. Currently, rodents play a key role in lymphatic research and most results are generated based on these models. Specifically, available rodent's models have been extensively used to develop our understanding of the lymphatic system [49–52]. There are postsurgical models of lymphedema that closely simulate the human conditions of primary and secondary lymphatic insufficiency. To study lymphatic disease, specifically lymphedema, a combined approach of skin excision, lymph node removal and radiation has been successfully used. The incision and cauterization of hind limb and tail tissue beds have been used to induce lymphedema in rodents [53,54]. Large animal models have been successfully used to study acquired lymphedema in dogs, sheep, and pigs [55–57]. Such models will help to refine the assessment of various therapeutic approaches and their potential applicability to human disease interventions. One challenge with surgically induced lymphedema in rodents is the fact that swelling resolves if given enough time [58],

however, secondary lymphedema is permanent in humans and occurs months to years after surgery.

1.4 Emerging techniques in lymphatic imaging

Near-infrared (NIR) fluorescence lymphatic imaging has emerged as a successful tool and has gained attention in recent years. Using fluorescent dyes, NIR imaging technologies have provided a solution for functional imaging of the lymphatic system in clinical and research settings. Indocyanine green (ICG) has gained attention in optical diagnosis of lymphatic function, however, this dye first was approved in the 1950s to assess cardiac function. Additionally, several effluent dyes such as Evans blue and Trypan Blue have been tested via subcutaneous and intradermal injection to map and visualize lymphatic vessel and lymph nodes. Several groups have used the near infrared imaging technique (NIR) to study lymphatic function in rodents. In particular, this technique has been successful to provide insightful information regarding lymphatic function in post-lymphatic surgery [54,59].

Computational modeling has emerged as a useful tool to shed light on the salient features of lymphatic function. Several groups have developed models to study lymphatic pumping based on mathematical models and experimental observations for collecting lymphatic vessels [60,61,70,71,62–69]. These computational models have been used to provide insight into lymphatic pumping under optimal working conditions; however, most of these studies are based on a single experimental observation in an *ex-vivo* or *in-vivo* study and conflicting results have been reported [72,73]. There have been efforts to constitutively model the passive and active mechanics of lymphatic vessels based on the

hyperelasticity theory and *ex-vivo* experiments [70]. This framework has been successfully used to fit experimental data from the rat thoracic duct. Furthermore, an algorithm was developed to use this framework coupled with a valve model to perform parametric studies of lymphatic adaptation to different loading conditions [71,74]. Yet, computational models based on the specific experimental results to study lymphatic growth and remodeling is lacking. There is a need to develop computational models based on specific experimental data from the tissue bed being modeled in order to enable prediction of changes in lymphatic pumping in disease scenarios.

1.5 Specific Aims

A prime example of a lymphatic disorder is secondary lymphedema, a progressive and debilitating disease mainly associated with fluid retention and tissue swelling among patients having or undergoing treatment for malignancy. The surgical removal of lymphatic vessels/nodes is known to be a potential risk factor to develop lymphedema even months to years after surgery and this risk is further increased with radiation and/or particular chemotherapeutic treatments. An impaired lymph circulation can induce overloads, ultimately leading to microstructural remodeling prior to the onset of lymphatic pathologies.

Although mechanical stresses are known to be fundamentally important regulators of lymphatic function, the role of sustained overloads (high flow and high pressure) in lymphatic dysfunction has yet to be established. Our **long-term goal** was to develop a mechanistic understanding of the active role of mechanics in growth and remodeling (G&R) of collecting lymphatic vessels in health and disease, and to ultimately have a better

understanding of mechanical culprits in lymphatic dysfunction. The **general objective** of my thesis was to experimentally and computationally investigate the modes by which sustained high flow and high pressure compromise normal function of the lymphatic system. It's been proposed that growth and remodeling (G&R) due to to disruption of mechanical loading occurs in three time scales: First, an immediate mechanical response through which solid and fluid mechanics of collecting lymphatic vessel alter and second, an acute response to compensate for changes in vessel function due to overloads. This step has been proposed to be mediated by biochemical agents released in response to overloads that occurs in minutes to hours time-scale. Third, a long-term remodeling response that alters material properties, geometry and function of vessels in days to months time-scale.

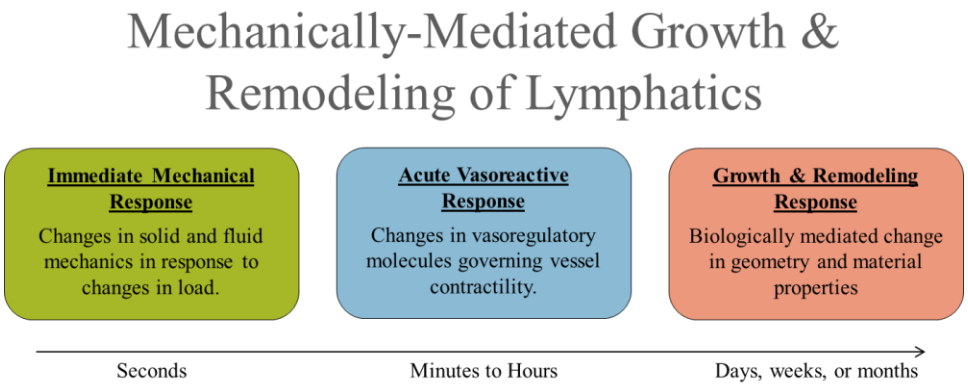

Figure 1. 1 A representation of the time course of lymphatic adaptation and G&R response to mechanical loads [70].

To develop a better understanding of the short-term and long-term remodeling response, we propose the following **Aims**:

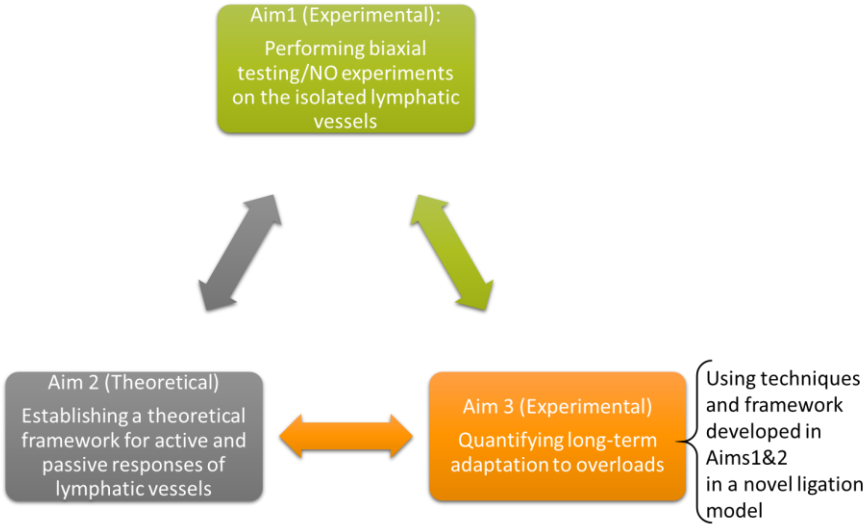

Figure 1. 2 An overview of the three aims to study lymphatic G&R. Aim 1 investigates biomechanical properties of lymphatic vessels via an experimental approach to study the contractile response of rat tail lymphatics to the immediate and acute perturbations in mechanical and biochemical stimuli. Aim 2 establishes a theoretical framework based on the constitutive modeling of lymphatic wall mechanics to study lymphatic pumping and alteration in contractile function in response to immediate and acute perturbation of mechanical and biochemical stimuli in the context of a lymphangion chain. Aim 3 investigates structural and functional remodeling of collecting lymphatic vessels in response to lymphatic injury via a novel rat tail ligation model.

Aim 1: To experimentally quantify the **acute response** of collecting lymphatic vessels to mechanical stretch (pressure and axial stretch) as well as biochemical agents (e.g., nitric oxide (NO)) via a novel rat tail model. There are two milestones for Aim 1 as follows:

Milestone 1.1: To characterize the effect of axial stretch under a controlled biaxial load on lymphatic contractility via ex-vivo experiments on the isolated rat tail lymphatic vessels.

Hypothesis 1.1: Acute perturbations in the axial stretch, as well as pressure, modulate lymphatic contractions in rat tail lymphatics.

Milestone 1.2: To characterize the effect of exogenously administered NO on lymphatic contractility via ex-vivo experiments on the isolated rat tail lymphatic vessels.

Hypothesis 1.2: Exogenous NO inhibits lymphatic contractility of rat tail lymphatics in a dose-dependent manner.

To achieve this aim, I used isolated vessel experiments on the rat tail lymphatics where a segment of a lymphatic vessel is dissected and mounted on opposing cannulas in a custom-designed vessel chamber that allows for control of both axial stretch and transmural pressures. Histology and two-photon imaging are also used to investigate the microstructure of isolated lymphatic vessels.

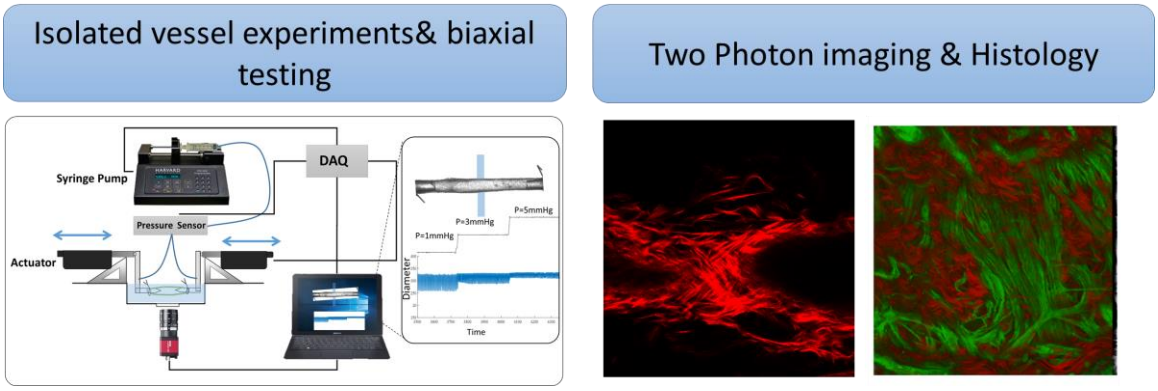

Figure 1. 3 An illustration of experimental setup (isolated vessel experiments) and histological approach used in Aim 1.

Aim 2: To establish **a microstructurally motivated chemo-biomechanical framework** based on the experimental observations in Aim1 to model the passive and active responses of rat tail lymphatic vessels to **mechanical/biochemical perturbation** (axial stretch and nitric oxide). There are three milestones for Aim 2 as follows:

Milestone 2.1: To determine the material parameters that describe the passive constituents of rat tail lymphatics and the variance of these parameters using a microstructurally-motivated model and a bootstrapping technique.

Hypothesis 2.1: Using the bootstrapping technique enables us to determine the unique intraspecific biomechanical properties of rat tail lymphatics

Milestone 2.2: To develop a computational framework to model the effect of exogenous NO and axial stretch on lymphatic contractility.

Hypothesis 2.2: Changes in lymphatic contractility due to axial stretch and NO administration can be modeled via the effects of NO on force production by lymphatic muscle cells and the effects of axial loading on circumferential stretch and length-tension relationships describing lymphatic force production in the circumferential direction.

Milestone 2.3: To develop an algorithm for modeling a chain of contracting lymphangions based on the constitutive modeling approach to characterize the maximal pressure generation capacity of the lymphatic chain.

Hypothesis 2.3: The maximal pressure generation capacity of the lymphangion chain depends on the number of lymphangions in the chain, the force generation capacity by the lymphatic muscle cells, and thus will be reduced by exogenous NO administration.

To achieve this aim, I use a constitutive framework to model passive biomechanics of lymphatic vessels, an active model for force production by lymphatic muscle cells, and a valve model to simulate the function of intraluminal valves. Ultimately, all these models are coupled into a custom-written matlab code to model contractions of a chain of lymphangions.

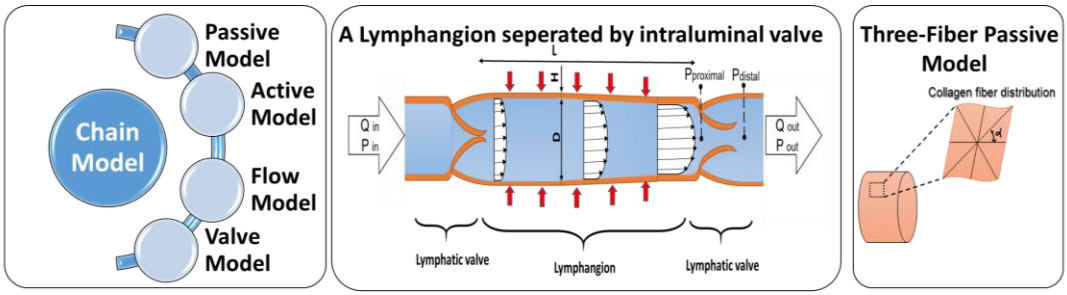

Figure 1. 4 A schematic figure of the computational frameworks used to model a lymphangion chain The constitutive equation is a four-fiber family model originally developed by Caulk et al [75].

Aim 3: To develop a novel **ligation model** in the rat tail to study the **prolonged adaptations** of collecting lymphatic vessels to mechanical overloads. There is one milestone for Aim 3 as follows:

Milestone 3.1: Developing a novel lymphatic injury model in the rat tail and testing the feasibility of using this animal model to study load-induced remodeling in collecting lymphatic vessels via in-vivo imaging and ex-vivo experiments on the isolated vessels.

Hypothesis I: I test whether the surgical removal of relatively large segments of lymphatic vessels from one side of the tail triggers a remodeling response resulting in a progressive decline in lymphatic function.

To achieve this aim, I use longitudinal functional near-infrared (NIR) imaging, ex-vivo experiments on the isolated lymphatic vessels and histology to study lymphatic remodeling via the novel rat tail model.

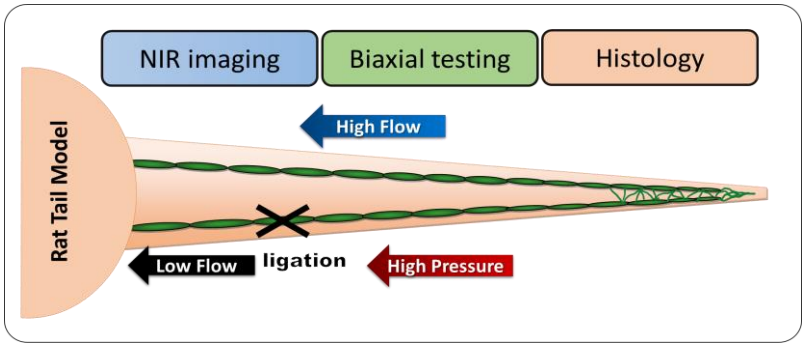

Figure 1. 5 A schema of proposed novel lymphatic ligation model and experimental approaches to study lymphatic remodeling post-lymphatic injury.

From these specific aims, I elucidate the role of sustained overloads in remodeling of collecting lymphatic vessels through both experiment and computation. To date, there has not been a specific quantitative or experimental framework to predict functional, microstructural and morphological consequences of non-compensatory/pathophysiological remodeling in lymphatic vessels. The goal of my PhD thesis was to provide a framework to study mechanically mediated G&R based on the specific data capturing the biomechanics and function of collecting lymphatic vessels over G&R time courses. Currently, most patients cannot be diagnosed until late into the progression of lymphatic dysfunction. The results of this work might provide a better understanding of the modes by which mechanics impairs lymphatic structure and function, and may provide insight into earlier diagnosis and improved therapeutic strategies for lymphedema disease.

CHAPTER 2. THE ROLE OF AXIAL STRETCH AND NITRIC OXIDE IN LYMPHATIC CONTRACTILITY

2.1 Aim 1

In this chapter, I experimentally quantify the ***acute response*** of collecting lymphatic vessels to mechanical stretch (pressure and axial stretch) as well as biochemical agents (e.g., nitric oxide (NO)) via a novel rat tail model. My ***hypothesis*** is that the axial stretch and exogenous NO are modulators of lymphatic contractility in these rat tail vessels. There are two milestones associated with this aim.

Milestone 1: To characterize the effect of axial stretch under a controlled biaxial load on lymphatic contractility via ex-vivo experiments on the isolated rat tail lymphatic vessels.

Hypothesis: Acute perturbations in the axial stretch, as well as pressure, modulate lymphatic contractions in rat tail lymphatics.

Milestone 2: To characterize the effect of exogenously administered NO on lymphatic contractility via ex-vivo experiments on the isolated rat tail lymphatic vessels.

Hypothesis: Exogenous NO inhibits lymphatic contractility of rat tail lymphatics in a dose-dependent manner.

2.1.1 Introduction

Lymphatic vessels serve as the major route to transport lymph from the interstitial space to the great veins [18,76,77]. Collecting lymphatic vessels play a key role in

lymphatic transport as they serve as a pump to propel lymph against an adverse pressure gradient [18]. These vessels have specialized smooth muscle cells (SMCs) that enable them to contract spontaneously [10]. The vessels' rhythmic and synchronized contractions are orchestrated to propel lymph in an efficient way along the chain of vessels [78,79]. In addition, lymphatic vessels exhibit tonic constrictions (maintained contractions) to control vessel caliber [18,80]. Mechanical stimuli (e.g., pressure and flow), as well as biochemical stimuli (e.g., vasoactive agents such as nitric oxide), are believed to be key regulators of lymphatic contractility.

Although mechanical regulation of lymphatic vessels in response to flow and pressure are well documented, less is known about the role of axial loading in the modulation of lymphatic function. To date, there is no information available on the role of axial stretch on lymphatic contractility. The majority of information on lymphatic contractility is based on isolated vessel experiments in which vessels are excised out of their natural environment. Although it has not been documented formally in the literature, from isolated vessel experiments it is known that a lymphatic vessel requires a level of axial pre-stretch to enable contractions. For the reasons mentioned above, it is important to consider the role of axial loading on lymphatic contractility and quantify the role of axial loading and axial contractility on lymphatic function.

The purpose of this chapter is to provide experimental evidence of the significance of axial pre-stretch on the modulation of lymphatic contractions through *ex vivo* isolated vessel experiments in rat tail lymphatics. I developed a novel rat tail model to test the hypotheses that lymphatic vessels are under pre-axial stretch *in situ* and that axial stretch modulates lymphatic contractions. Using isolated vessels experiments along with

immunostaining, I quantified the effect of axial stretch on lymphatic contractility and examined the organization of lymphatic SMCs and collagen fibers and their contributions to the physiological function of lymphatic vessels.

2.1.2 Methods

2.1.2.1 Animal model and vessel isolation procedure.

An incision (~1 cm) was made in one side (left or right side) near the base of the tail to gain access to the lateral tail vein of male Sprague Dawley rats (300-350 g), with care taken to avoid injury to the lateral vein or artery. Trypan Blue Solution 0.4% dye was injected upstream of the incision site to enhance the visibility of lymphatic vessels. Under a stereo microscope, a lymphatic chain that runs parallel to the lateral vein was visualized. Segments of lymphatic vessel (~2mm) were excised. Once isolated, vessels were placed in Dulbecco's Phosphate Buffered Saline (DPBS, Corning). After removing the surrounding fat and connective tissues, lymphatic vessels (containing approxiamtely1-2 valves) were mounted on opposing cannula in a custom-made vessel chamber [75]. The protocol for these experiments was approved by Georgia Tech's Institutional Animal Care and Use Committee (IACUC).

2.1.2.2 Experimental setup, protocol, and data acquisition.

We improved a previously developed perfusion device to measure and control transmural pressure, diameter, and axial stretch [81]. A custom program in LabVIEW was developed to control transmural pressure via a syringe pump (Harvard) and pressure sensors (1psi SSC series, Honeywell). Axial stretch was precisely controlled via linear

actuators and XYZ stages (Newport Precision, LTA series and M-461 series). This system was placed on an inverted microscope and the contractility response of the mounted vessel under different transmural pressures/axial stretches was measured. Using the LabVIEW program, the diameter of the vessel, obtained from an inverted microscope (2.5x magnification) and digital camera (Allied Vision Technologies, Marlin F-033B) capturing at 18 fps tracing, was recorded in real-time and saved to the hard drive for further analysis. In a temperature-controlled bath containing DMEM/F-12 (Dulbecco's Modified Eagle Medium/Nutrient Mixture F-12 plus Pen-Strep 1:100, pH=7.4 at 37℃) [82], the vessel was equilibrated for ~1hr to develop stable contractions. For the stretch protocol, the vessel was preconditioned and then the pressure was held constant at 2mmHg while three stretch steps of 10%, 20%, and 30% were used respectively. The axial stretch was measured with respect to the buckling length as described in the next section. These values were chosen based on a pilot study to determine the pressure at which contractions are maximum.

2.1.2.3 Measurement of axial stretch in-vivo.

To measure in-situ stretch, the animal was placed under a ZEISS dissecting microscope equipped with an AxioCam MRc 5 (ZEISS inc) camera. After removing the skin from the base of the tail, Trypan blue (0.4%) was injected to the tip of tail to enhance the visibility of a lymphatic vessel under the microscope. After removing the perivascular tissue, pins (0.2 mm diameter, Fine Science Tools inc) were used to mark the length of the segment prior to dissection. Using microsurgical scissors, a segment of lymphatic vessel located between two pins was dissected. Subsequently, ImageJ software was used to determine in-situ stretch. Further, to measure axial stretch in-situ under physiological

pressure a single vessel was tied off prior to the dissection and the same procedure was repeated.

2.1.2.4 Measurement of axial stretch ex-vivo.

To determine ex-vivo stretch, vessels were preconditioned in a temperature-controlled bath for ~1 hr. Once the vessels were preconditioned, buckling length was determined via an inverted microscope equipped with a camera(Marlin Allied vision) to measure the vessel's length as well as precision linear micrometer actuators (Newport) to linearly change position of the micropipettes. The buckling length was defined as the minimum axial length required to the keep vessel straight where the vessel is not collapsed at nearly zero pressure(~0-0.5 mmHg). Next, the vessel length was measured between two sutures on glass pipettes using a custom-written LabView code. Subsequently, stretch was increased to 10%, 20% and 30% using precision micromanipulators (Fig. 2.1), respectively. Ultimately, vessel contractions were recorded at different axial stretches at a transmural pressure of 2mmHg.

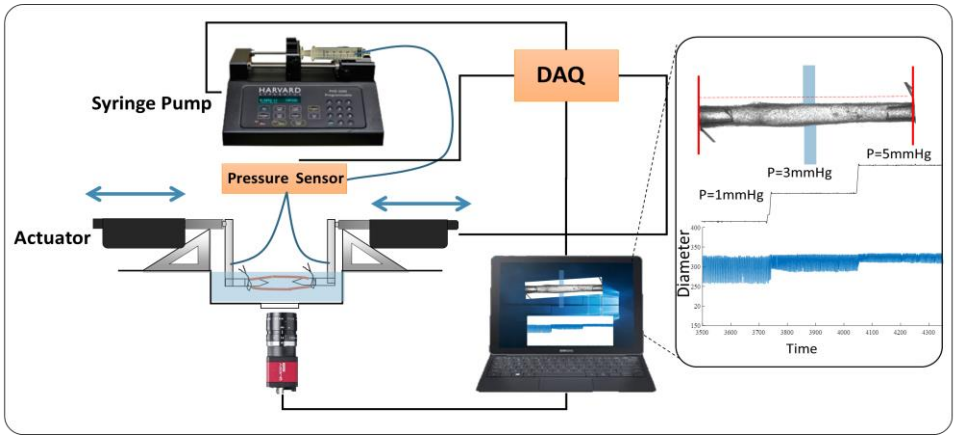

Figure 2. 1 A schematic diagram of ex-vivo measurement of axial stretch using ex-vivo setup. The vessel was pressurized at ~0.5mmHg to determine unloaded geometry. Axial stretch was determined with respect to the length at which vessel is not buckled.

2.1.2.5 Contractility metrics and statistics.

A custom-written MATLAB (MathWorks) program was used to calculate end-systolic diameter (ESD), end-diastolic diameter (EDD), and contraction frequency (FREQ) based on the raw data obtained during experiments. Subsequently, several metrics of lymphatic pumping were calculated including amplitude (AMP), ejection fraction (EF), fractional pump flow (FPF) as:

$$\text{Amplitude: (AMP)} = (\text{EDD}-\text{ESD}) \quad (1)$$

$$\text{Ejection fraction: (EF)} = [\text{EDD}^2-\text{ESD}^2]/\ \text{EDD}^2 \quad (2)$$

$$\text{Fractional pump flow: (FPF)} = \text{EF}\times\ \text{FREQ} \quad (3)$$

Data obtained from the stretch protocol were plotted as a function of stretch. To determine statistical significance, a one-way ANOVA in conjunction with Bonferroni's post hoc correction was used to make multiple comparisons. Prism 5 (GraphPad Software) was used

to perform all statistical analyses with significance set at $p < 0.05$ and results were reported as means (±SEM).

2.1.2.6 Whole-mount immunofluorescence staining.

Rat tail lymphatic vessels were isolated and fixed for two hours in 4% PFA at room temperature. After fixing, the vessel was washed three times with PBS and blocked with 5% goat serum in PBS and 0.5% Triton X-100 for 1-2 hours , followed by addition of the primary antibody (1:100; α-SMA Sigma) and incubation for 48 hours overnight at 4ºC (primary antibody was replaced with fresh one after 24 hours). After washing in PBSTx (0.3% Triton X-100 in PBS) three times, the sample was incubated in secondary antibody at room temperature for 2 hours (1:1000, Alexa Fluor® 488, goat anti-mouse antibody). After finishing the staining, the vessel was washed in PBSTx three times and mounted in Prolong Gold for imaging.

2.1.2.7 Confocal and SHG image acquisition.

Confocal images of collecting lymphatic vessels from rat tails were acquired using a Zeiss LSM 710 system with 40x/1.3 and Plan-Apochromat 63x/1.4 oil-immersion objectives. The images of z-stacks were imported in ZEN lite (Zeiss) software to obtain 3D reconstructions. The second harmonic generation (SHG) of collagen fibers were obtained under 800 nm excitation wavelength. The orientation of fibers in acquired images was obtained using CT_FIRE software that automatically extracts individual fibers by applying the curvelet denoising filter followed by an automated fiber extraction method [83]. The orientation of the nuclei was obtained from DAPI staining and analyzing the respective images with CellProfiler software [84].

2.1.2.8 Collagenase experiments

To test whether the axial collagen constrains the length of lymphatic vessels, the vessel was treated with collagenase (Collagenase Type II) for 30 minutes. Once mounted in the vessel chamber containing PBS (Ca free) and treated with collagenase, changes in the length and diameter of vessel were measured using a custom-written LabView program. In addition, pressure-diameter curves were obtained at different axial stretches before and after collagenase treatment. Both the length and diameter of vessel increased after collagen degradation. The results suggest collagen fibers plays a significant role in constraining longitudinal and circumferential dimensions.

2.1.3 Results

Rat tail lymphatic vessels are under axial pre-stretch in vivo and increased axial stretch decreases contractility ex vivo. The results showed that collecting lymphatic vessels from rat tails experience significant axial stretch ($\lambda_z = 1.24 \pm 0.03$) *in situ* (Figure 2.1). The amplitude of contractions decreased as the stretch increased from 10% to 20%, however, a more significant reduction (50μm equal to ~90% reduction) occurred for the higher stretch of 30% (Figure 2.2).

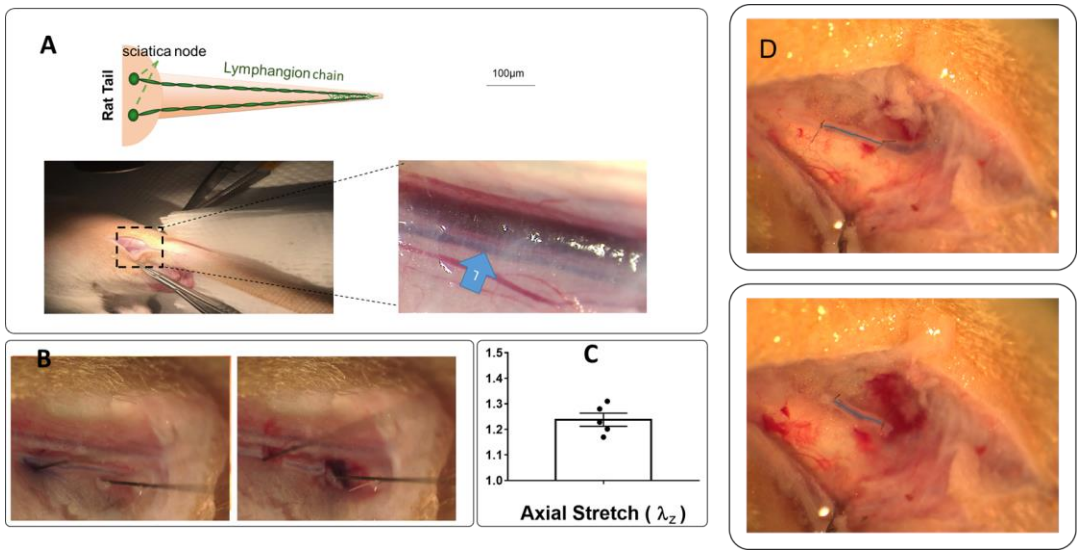

Figure 2. 2 A schematic diagram showing (Panel A) chains of lymphatic vessel in rat tails, an image of the location where an incision was made to gain access to the lymphatic vessel close to the base of tail, showing that the lymphatic vessel runs parallel to the tail vein and arteries, and (Panel B) an image showing lymphatic vessels from rat tails are under axial stretch *in situ* and (Panel C) a single measurement of axial stretch in-situ under physiological pressure (Panel D). The vessel has been tied off and is under 12% axial stretch.

Similar trends were observed for the frequency, which decreased from 15 min^{-1} to less than 5 min^{-1} (~80% reduction), the ejection fraction, which decreased from 46% to 9% (~80% reduction), and the fractional pump flow, which decreased from 6.8 min^{-1} to 0.58 min^{-1} (~92% reduction). Notably, contractility metrics, (e.g. ejection fraction) slightly decreased at 20% stretch, however, the 30% stretch significantly changed contractility and almost inhibited phasic contractions. The results demonstrate that collecting lymphatic vessels contractility is sensitive to axial stretch.

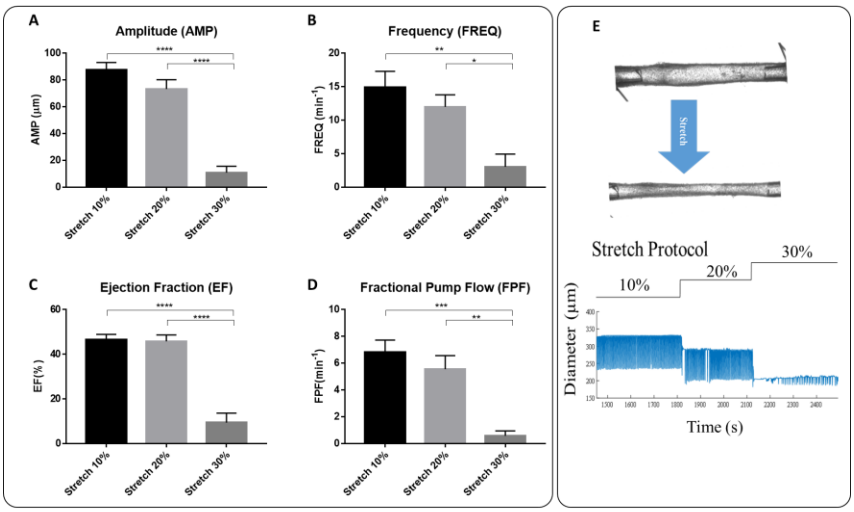

Figure 2. 3 Effect of axial stretch on contractile function of lymphatic vessels. The contractile parameters were plotted as a function of the axial stretch (n=5), including amplitude of contractions (AMP; Panel A), frequency of contractions (FREQ; Panel B), ejection fraction (EF; Panel C), fractional pump flow (FPF; Panel D)., Panel E shows an image of a rat tail lymphatic vessel cannulated on glass micropipettes along with respective raw traces of contractions at different stretches. The pressure was set to 2mmHg for all experiments. All data are presented as mean (±SE) and statistical significance was tested via ANOVA and Bonferroni post-hoc tests (* $p < 0.05$, ** $p < 0.005$)

Collagen fibers are predominantly oriented in the axial direction. The analysis of collagen fibers showed that the probability of fiber angle distribution was maximum in the axial direction while the minimum occurred in the circumferential direction (Figure 2.3). Further, imaging of collagen fiber orientation at high pressure ($p \cong 8$mmHg), and comparison of the results to images at low pressure ($p \cong 2$mmHg), revealed that increasing the pressure does not change the maximum probability of fiber alignment in the axial direction. However, the circumferential orientation slightly increased (< 5%) suggesting most collagen fibers are oriented in the axial direction even at high pressures. At physiological pressure, the distribution was normal with a maximum near the axial direction (~70% of fibers, $-30 < \alpha < 30$).

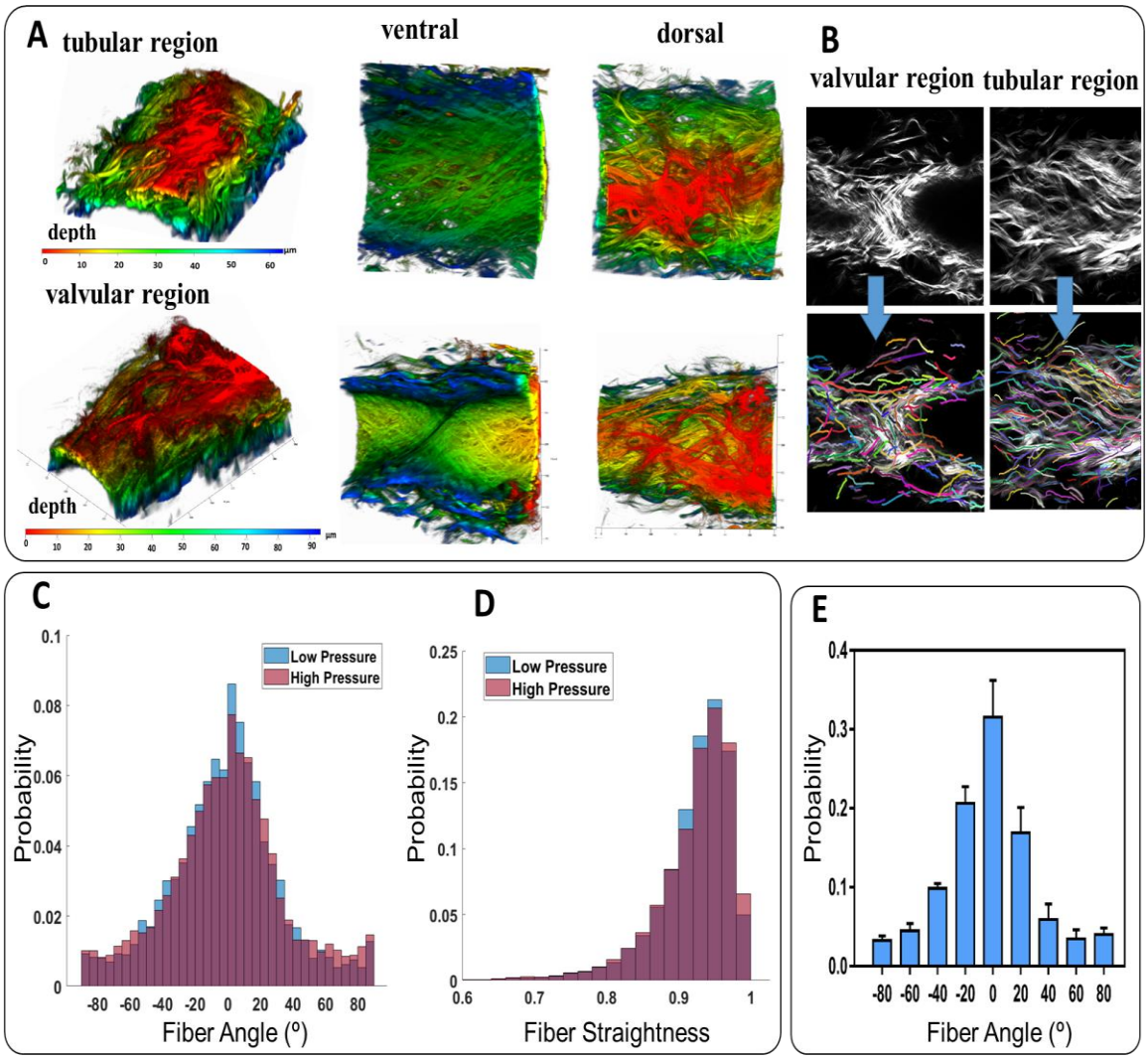

Figure 2. 4 Collagen fiber organization within the wall of a pressurized, unfixed rat tail lymphatic vessel in tubular and valvular regions including reconstruction of SHG imaging of collagen fibers along with dorsal view ventral views (Panel A), the z-stack images obtained from SHG imaging of collagen fibers and respective fiber extractions using CT-FIRE algorithm (Panel B), distribution of collagen fiber angles (Panel C), distribution of collagen fiber straightness within the vessel wall for low (~2 mmHg) and high (~8mmHg) pressure scenarios (Panel D), and the average distribution of collagen fibers obtained from five vessels plotted as the mean value along with the standard deviation (Panel E, the width of each bin is 20^0 and values of *x-axis* indicate the center of each bin). The vessels were excised from the base of the tail and mounted on glass pipettes in a custom-made

vessel chamber compatible with the microscope. The vessels were unfixed, the pressure was ~2 mmHg, and the axial stretch was ~10%.

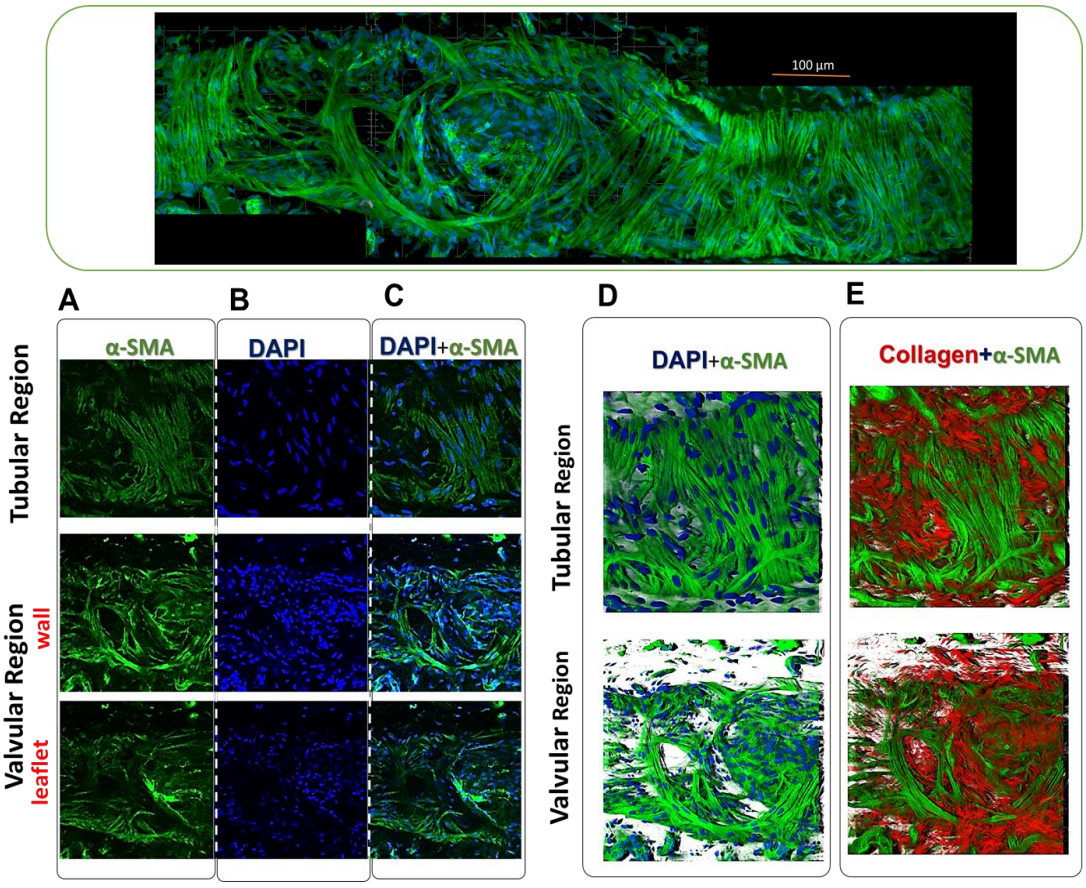

Figure 2. 5 Lymphatic smooth muscle coverage and fiber organization in collecting lymphatic vessel from rat tails. A representative image (z-stack) staining for smooth muscle actin (α-SMA; Panel A), nuclear staining (DAPI; Panel B), and merged SMA and DAPI (Panel C) for valvular and tubular regions of a lymphatic vessel from rat tails. The 3D reconstruction of actin fibers of SMCs with nuclear staining (DAPI and SMA; Panel D) and with collagen fibers were obtained from SHG imaging (collagen and SMA; Panel E). The vessel was fixed and flatted on a glass slide. The images were taken from the same vessel and the imaging window dimensions and depth were about 300µm×300µm and ~10µm respectively. The images from different locations were stitched together to obtain an image of the first panel.

Orientations of lymphatic SMCs are heterogeneous, covering both axial and circumferential directions. Whole mount staining for α-SMA and DAPI staining for nuclei revealed one dense layer of lymphatic MSc with the occasional second layer (Figures 2.4 and 2.5). The layers of lymphatic SMCs showed different patterns in tubular

and valvular regions. Tubular region was defined as 100µm distance from the valve. A closer look at SMCs coverage in the tubular the region showed a heterogeneous structure of strips in the circumferential direction with sporadic longitudinal bundles connecting different fibers, whereas the valvular region was predominantly composed of thick bundles in the longitudinal direction. That it is possible that the alignment is more circumferential as one moves further away from the valve. The analysis of actin fibers and nuclei orientation confirmed that most cells, as well as actin and collagen fibers in the valvular region, were aligned in the axial direction, whereas the tubular region's nuclei and actin fiber distributions are more heterogeneous (Fig. 2.6). The local maximum of nuclei and actin fiber orientations occurred in both axial and circumferential directions, but collagen fibers were predominantly oriented in the axial direction.

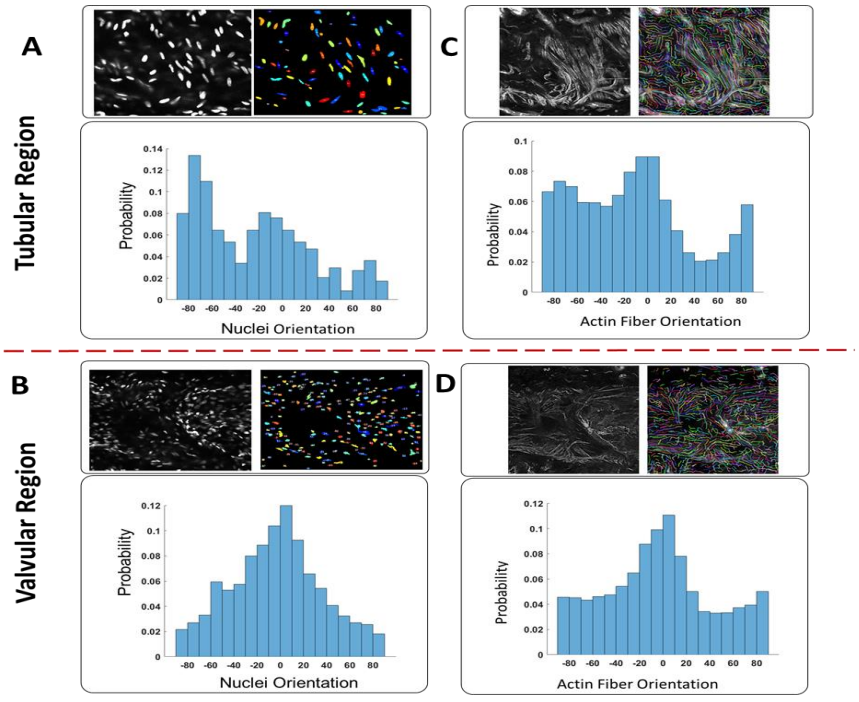

Figure 2. 6 Analysis of nuclei (Panel A and B), and actin fiber (Panel C and D), obtained for valvular and tubular regions. The histograms were plotted based on different z-stacks obtained from DAPI, α-SMA imaging in Fig. 2.4 (D & E).

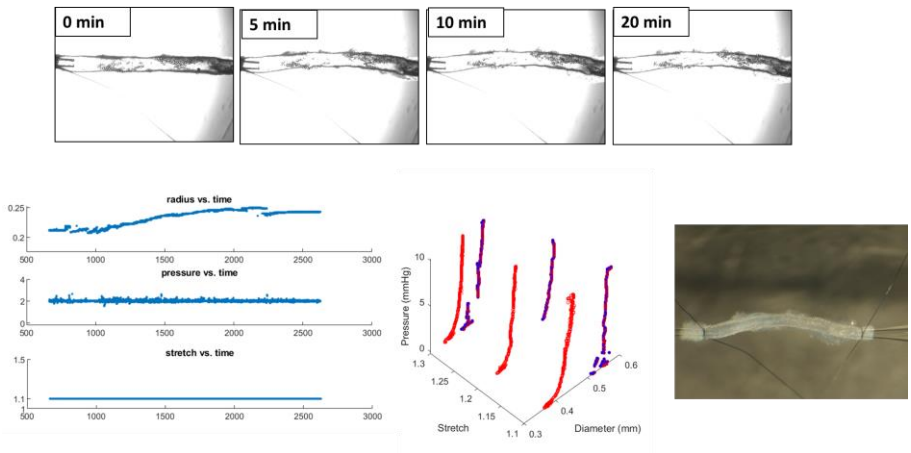

Figure 2. 7 Results of the collagenase experiment for a single vessel treated with Collagenase Type II for 30 minutes. Both the diameter and length of the vessel increase after degradation of collagen fibers suggesting that collagen fibers contribute to constraining vessel dimensions.

Effects of transmural pressure on lymphatic contractility. The amplitude of contraction decreased from 90.7µm to 29.9µm as the pressure increased from 2mmHg to 6mmHg (Fig. 2.7A). Similarly, the ejection fraction decreased 67% (from 44.6% to 14.7%) as pressure increased from 2mmHg to 6mmHg (Fig. 2.7B, *n*=5). In contrast, the frequency of contractions increased ~ 40% (from ~7.4 min^{-1} to ~12.3 min^{-1}) as the pressure increased from 2mmHg to 4mmHg; however, a further elevation of transmural pressure from 4mmHg to 6mmHg slightly increased frequency (~12.3 min^{-1} at 4mmHg to ~13.3 min^{-1} at 6mmHg, Fig. 2.7C). Consequently, the fractional pump flow increases from ~3.5 min^{-1} at 2mmHg to ~5.1 min at 4mmHg; however, an additional pressure increment (from 4mmHg to 6mmHg) resulted in ~ 47% reduction in pumping (~2.7 min^{-1} at 6mmHg, Fig (2.7D)). All functional experiments were performed at one axial stretch (~10%).

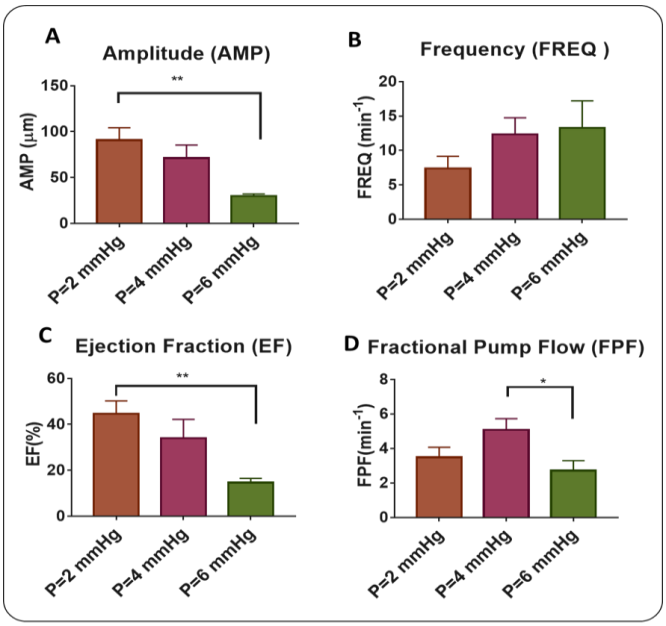

Figure 2. 8 Effect of transmural pressure on the contractile function of rat tail lymphatic vessels. The contractile metrics were plotted as a function of transmural pressure (n=5), including the amplitude of contractions (AMP; Panel A), frequency of contractions (FREQ; Panel B), ejection fraction (EF; Panel C), fractional pump flow (FPF; Panel D). The axial stretch was ~10% for all experiments. All data are presented as mean (±SEM) and statistical significance was tested via ANOVA with Tukey's post-hoc tests (* $p < 0.05$, ** $p < 0.005$)

2.1.4 Discussion

Mechanical loading plays an important role in lymphatic contractile function. Lymphatic vessels adapt their contractile function to various loading conditions (pressure, flow, and external forces from skeletal muscles) which is important in their function both as a pump and as a conduit to efficiently transport lymph [40,85–88]. The effect of pressure-induced stretch on lymphatic contractile function has been well-documented [87,89–97]. These experiments demonstrated the existence of a length-tension relationship in lymphatic vessels from different regions through *ex vivo* experiments on isolated vessels [10,17,98,99]. Although there is heterogeneity in the contractile force generated from different regions, these studies suggest that muscle cells produce a maximum force in a wide range of pre-load (circumferential stretch) conditions [100].

Similar to circumferential stretch, axial stretch can also be a modulator of lymphatic function. In some regions, such as lung and diaphragm, the length of the vessel changes due to applied external forces. For example, pleural and diaphragm lymphatics can be exposed to cyclic stretches which enhance lymph formation and transport [101,102]. In this study, we showed that lymphatic vessels from rat tails are under axial pre-stretch *in vivo*. The isolated vessel experiments demonstrate that lymphatic vessels are sensitive to changes in the axial stretch. An axial stretch of 30% significantly decreased lymphatic contractions. To our knowledge, our study is the first to demonstrate the significance of axial stretch in the modulation of lymphatic contractility. We characterized the response of rat tail lymphatics to the axial stretch to shed light on the contractile force adaptation of lymphatic SMCs to axial stretch. Change in calcium influx is one possible mechanism through which stretch can modulate lymphatic contractility. Since lymphatic vessels are very sensitive to changes in extracellular Ca^{+2}, e.g. too low a level or too high a level of Ca^{+2} ceases lymphatic contractions [92,103–105], the stretch might alter the extracellular calcium and thereby change the function of calcium channels such as voltage-gated L-type and T-type channels. There is also evidence that electrical activity of lymphatic vessels changes with the stretch. The higher stretch induces Ca^{+2} sensitization that increases the sensitivity of key contractile molecules to Ca^{+2} [106–108].

Smooth muscle shape and orientation may contribute to axial contractility. Another key factor that determines the effect of stretch is the shape and orientation of lymphatic SMCs. One study reports α-SMA positive cells (lymphatic SMCs) in rat diaphragm run longitudinally between intraluminal valves, but circumferentially in the valve regions [109]. Another study in guinea pig mesenteric lymphatics reports that some SMCs are

longitudinally orientated while others are orientated at approximately a 45° angle [110]. An investigation of lymphatic vessels in the diaphragm has suggested that active vessels showing rhythmic contractions have a dense mesh of actin fibers, but non-contracting vessels have longitudinal actin fibers [111]. Another investigation of lymphatic muscle cells via F-actin staining in human thoracic ducts has suggested that non-contracting thoracic vessels have an irregular organization of lymphatic SMCs and muscle bundles are heterogeneously oriented in the circular, oblique, and longitudinal directions [112]. Micrograph observation in monkeys has revealed cervical sections of the thoracic duct are less muscular compared to the abdominal and thoracic sections, suggesting the passive function of the cervical part [113]. As mentioned previously, it is believed that stretch modulates active contractions. Thus, axial stretch is also a candidate to alter active tension given the heterogeneous orientation of lymphatic SMCs. In the current study, immunostaining and imaging of fibers revealed the orientation SMCs are heterogeneous. In the tubular region, most fibers have circular orientation while some are longitudinally organized. In contrast, in the valvular region, most fibers have a longitudinal orientation. Analyzing the nucleus orientation of SMCs revealed a distribution similar to the actin fibers, suggesting that lymphatic SMCs are heterogeneously oriented. Thus, the axial stretch of SMCs may alter the active tension based on the orientation of lymphatic SMCs.

Collagen fiber orientation may play a role in axial contractility. In addition to the orientation and morphology of lymphatic SMCs, the organization of the extracellular matrix can influence lymphatic function. Particularly, collagen fibers play a key role in structural support and mechanics of lymphatic vessels. Currently, data on lymphatic vessel

wall mechanics and compositions are limited to a few measurements from rat thoracic duct, rat mesentery, and human pelvis [70,114,115]. Rat lymphatic vessels have been reported to be very distensible; a transition to a stiffer region occurs in response to an increase in transmural pressure [70]. It is thought that these vessels are very compliant in the physiological range (< 5 cm H2O) [115]. Observations from rat thoracic duct have shown the non-linear response and vessel stiffening occurs in response to both axial stretch and circumferential stretch [70]. It is believed that collagen, elastin, and SMCs are the main components that constitute the mechanical behavior of lymphatic vessels [70,114–116]. Collagen organization and fiber recruitment are important factors that not only determine the passive function but also influence the contractile function of lymphatic vessels. Recent multiphoton imaging of collagen fibers within the wall of the pelvic lymphatic vessel has shown that the fibers are predominately oriented in the axial direction [114]. Similar results were found for the bovine [116] and rat lymphatics, although there are some variations [70]. In the current study, we showed that collagen fibers are predominately oriented in the longitudinal direction, supporting our observation that the vessels experience pre-axial stretch *in situ*. Our results showed changing the transmural pressure from low to high pressure did not change the predominant orientation of collagen fibers in the longitudinal direction. The results suggest that vessels are under maintained longitudinal stretch *in situ*. The degradation of collagen fiber suggested that axial collagen contributes to constraining vessel dimensions. The other interesting finding is the sensitivity of vessels' spontaneous contractions to the level of pre-axial stretch. The *ex vivo* results suggest that vessel contractility is tightly regulated by the stretch level.

2.2 Milestone 2:

To characterize the effect of NO on lymphatic contractility via ex-vivo experiments on the isolated rat tail lymphatic vessels and administration of the exogenous NO.

Hypothesis II: Exogenous NO inhibits lymphatic contractility in a dose-response manner.

2.2.1 Introduction

The lymphatic system can adjust the contractile function in response to mechanical and biochemical stimuli. Mechanical stretch due to pressure is known to be a key modulator of lymphatic contractility (6–10). It is well documented that the frequency of contractions changes in response to pressure and the active tension changes with stretch for lymphatic vessels [122–124]. In addition, previous studies have demonstrated small molecules such as nitric oxide (NO), histamine, and endothelin-1 (ET-1) play key roles in the regulation of lymphatic contractility [4,125–129]. For example, the effects of endothelial-derived NO due to flow-shear sensation by lymphatic endothelium or NO production from iNOS-expressing cells surrounding lymphatic vessels in inflammatory scenarios have been studied [42,125,130–132]. The effect of endothelial-derived NO on lymphatic contractility is also well documented via pharmacological inhibition and genetic deletion of eNOS [125,132]. There are some studies that investigate the effect of exogenously administrated NO on lymphatic contractility [133]. Yet, there is a pressing need for specific experimental data to develop computational models capturing the effect of exogenous NO on lymphatic contractility in a dose-dependent manner.

2.2.2 Methods

2.2.2.1 Vessel isolation.

Segments of collecting lymphatic vessels from male Sprague Dawley rats (300-350 g) were isolated. Once isolated, vessels were immediately placed in Dulbecco's Phosphate Buffered Saline (DPBS, Corning) and the surrounding fat and connective tissues were carefully removed. Once cleaned, vessels were mounted on opposing cannulae in a custom-designed vessel chamber [75]. For the isolated vessel experiments, each vessel was harvested from a different animal. All animal protocols were reviewed and approved by Georgia Tech's Institutional Animal Care and Use Committee (IACUC).

2.2.2.2 Study of Active Contractility and its Response to Nitric Oxide.

After removing the surrounding fat and connective tissues, lymphatic vessels (containing approxiamtely1-2 valves) were mounted on opposing cannula in a custom-made vessel chamber. Once the vessels were preconditioned for ~ 1hr, four doses of SNP (10^{-7} , 10^{-6} , 10^{-5} , 10^{-4}) were administrated for 5 minutes at each dose. To quantify contractility response of lymphatic vessels, we used a custom-written LabView program to analyze images recorded during the protocol. Once data was analyzed, end-systolic diameter (ESD), end-diastolic diameter (EDD), and contractions frequency (FREQ) were calculated. Subsequently, several metrics of lymphatic pumping were calculated including amplitude (AMP), ejection fraction (EF), fractional pump flow (FPF), as defined previously. Data obtained from the stretch-pressure protocol were plotted as a function of stretch and pressure respectively. Additionally, to determine changes in the contractile response of lymphatic vessels to doses of SNP , changes in the contracile parameters and a change in lymphatic tone (Tone) were calculated as follows:

$$\text{Change in Tone} = (EDD - EDD_{control})/EDD_{calcium\text{-}free} \quad (4)$$

$$\text{Change in AMP} = (AMP - AMP_{control})/ AMP_{control} \quad (5)$$

$$\text{Change in EF} = (EF - EF_{control})/ EF_{control} \quad (6)$$

$$\text{Change in FPF} = (FPF - FPF_{control})/ FPF_{control} \quad (7)$$

$EDD_{calcium\text{-}free}$ indicates the end-diastolic diameter in calcium-free state at the same pressure. The subscript "control" represents the parameters before administration of SNP doses.

2.2.2.3 Statistics.

To determine the statistical significance between control and experimental groups, a one-way ANOVA in conjunction with Tukey's post hoc correction was used to make multiple comparisons. Prism 5 (GraphPad Software) was used to perform all statistical analyses with significance set at $p < 0.05$ and results were reported as means (±SEM).

2.2.3 Results

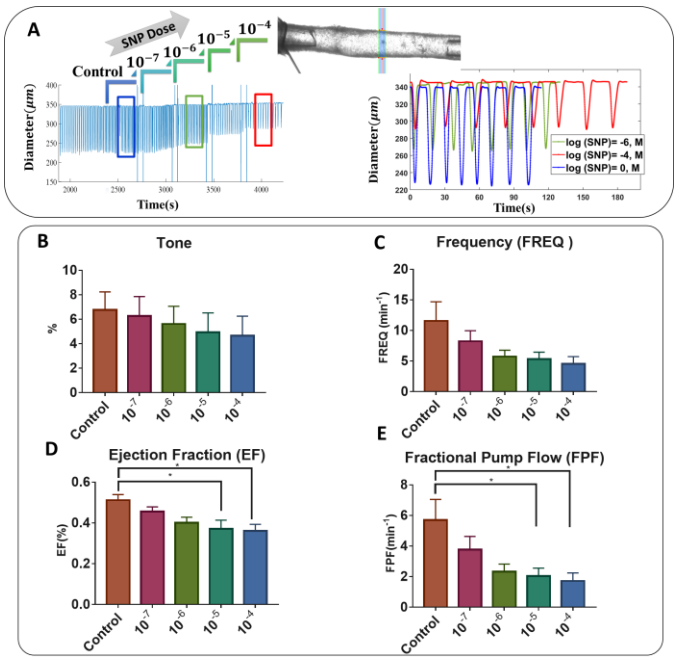

Figure 2. 9 Effect of exogenous NO via SNP administration on contractile function of isolated vessels from rat tail. A representative of diameter tracing from an isolated vessel experiment where different doses of SNP were administrated (Panel A). The change in contractile parameters were plotted as a function of SNP doses, including change in basal tone (Tone; Panel B), frequency of contractions (FREQ; Panel B), ejection fraction (EF; Panel C), fractional pump flow (FPF; Panel D). The pressure was set to 3mmHg and the axial stretch was ~10% for all experiments. All data are presented as mean ±SEM (n=4) and statistical significance was tested via ANOVA with Tukey's post-hoc tests (* $p < 0.05$)

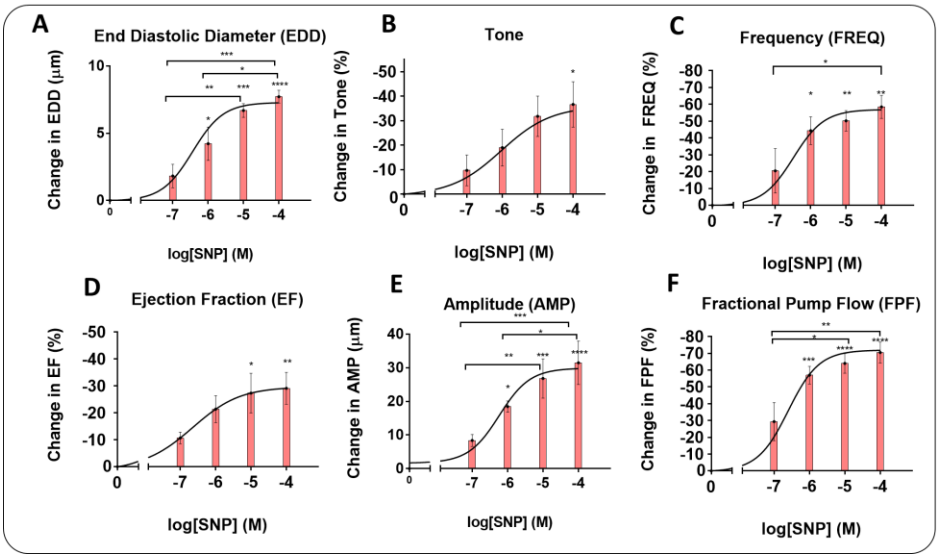

Figure 2. 10 Percent change in contractile metrics (from Fig.2.8) in response to different SNP doses including percent change in end-diastolic diameter (AMP; Panel A), percent change in basal tone (Tone; Panel B), percent change in frequency of contractions (FREQ; Panel C), percent change in amplitude of contractions (AMP; Panel D) percent change in ejection fraction (EF; Panel E),

percent change in fractional pump flow (FPF; Panel F). All data are presented as mean ± SEM (n=4) and statistical significance was tested via ANOVA and Tukey's post-hoc tests (* $p < 0.05$, ** $p < 0.005$, etc). The statistical significances were tested to compare changes with respect to control values (SNP dose=o) as well multiple comparison between different doses.

Exogenous NO inhibits lymphatic contractility in a dose-dependent manner. A representative isolated lymphatic vessel from rat tail along with respective diameter tracing in response to the administration of SNP doses to the bath is shown in Fig. 2.8. The contractile activity of the isolated vessels in response to the administration of SNP doses was quantified (Fig. 4 , n=4). The lymphatic tone decreased by 36.6% (from 6.8% to 4.6%) equivalent to ~8um increase in the diastolic diameter (Figs. 2.8B 2.9B). The frequency of contractions significantly decreased almost 60% (from ~11.6 min^{-1} to ~4.5 min^{-1}) at the highest dose; however, the maximum reduction occurred from 10^{-7} (M) to 10^{-8} (M), (Figs. 2.8 and 2.9C). Similar trends were observed for the ejection fraction and amplitude of contraction, however, the maximum reduction was around 30%. The ejection fraction decreased 31.4% (from 0.52 to 0.36) at the maximum dose respectively (Fig. 2.8D-E and 2.9D-E) . Consequently, the fractional pump flow decreased with increase in the SNP concentration up to ~70% (Fig. 2.8F and 2.9F). All experiments were performed at constant pressure (~3mmHg) and one axial stretch (~10%).

2.2.4 Discussion

The strong pumping capability of rat tail lymphatic vessels. The effect of the transmural pressure on the modulation of lymphatic contractility has been very well-documented. Gashev et al. [134] have previously characterized the regional heterogeneity of contractility in the rat mesentery, rat thoracic duct, rat neck, and rat hindlimb lymphatics. In the rat mesentery, rat neck, rat hindlimb the frequency continuously increases with the

incrementally increase in the pressure, while the rat thoracic duct shows a peak in the mid-pressure range and the frequency decreases for the higher pressures. The rat neck lymphatic vessels have the highest frequencies while the thoracic duct has the smallest frequency. In contrast, the rat mesentery and rat thoracic duct have the highest ejection fraction while the rat neck has the smallest ejection fraction values. Consequently, the rat mesentery has the highest values of fractional pump flow, the thoracic duct has the lowest values, while the rat neck and hindlimb have comparable values. Further, a peak is observed in the fractional pump flow for all the lymphatic vessel from all regions. Our characterization of rat tail lymphatic contractility, suggests that the values of the frequency response are similar to those of the rat mesentery; however, the ejection fractions are slightly smaller and are closer to those of thoracic duct. Ultimately, the fractional pump flow from the rat tail that represents the overall pumping is similar to the rat mesentery. The regional heterogeneity in lymphatic function suggests that some vessels mainly serve as a pump (e.g., mesenteric lymphatics) where a high pumping capacity is needed, and some mainly function as a conduit (e.g., thoracic duct) where the minimal pumping is required [17,134]. This idea is also supported by the shear-flow sensitivity response in lymphatic vessels, where a significant shear-inhibition is observed in the lymphatic vessels from rat thoracic duct [135,136]. Our results suggest that the collecting lymphatic vessels from the rat tail exhibit strong pumping capability similar to the rat mesentery. Functionally, the rat tail lymphatics are afferent (pre-nodal), where there is no lymph node upstream to the vessels. Hence, the strong contractility can be justified by their major pumping role in the tail tissue.

The physiological importance of NO and its inhibitory effect on lymphatic function. The nitric oxide (NO) is believed to be a key regulator in the modulation of

lymphatic contractile function [97,137–141]. There are several sources of NO in lymphatic systems including 1) production of NO via LECs (eNOS pathway) due to shear stress 2) production of NO via inducible NO synthase (iNOS pathway) in immune cells or lymphatic SMCs surrounding lymphatics 3) production via nerve tissues (nNOS pathway) in perivascular tissues [79,125,139,142,143]. The mechanism of NO action is believed to be through the cGMP pathway that leads to the relaxation of muscle cells [144–149]**.** Based on immunohistochemical studies and microelectrode measurement of NO, it has been suggested that NO is produced in response to flow in both valvular and tubular region of a lymphangion [4,131,150]. There is evidence that contractile metrics such as amplitude and frequency of contractions attenuate in response to NO synthesis due to imposed flow [9,97]. Similarly, inhibition of NO synthase has shown that contractions enhance under the basal conditions and that the inhibitory effect of imposed flow on contractions is inhibited [125,151,152]. It is widely accepted that the effect of NO can be context-specific. For example, high concentration of NO is believed to suppress amplitude and frequency of contractions; however, low concentration of NO is thought to enhance contractions by increasing amplitude at the expense of frequency reduction [4,125,131,132,141,142,153]. In contrast, comparing the *in-situ* measurements of lymphatic function in NO-deficient ($eNOS^{-/-}$) mouse, to the temporary inhibition of NO synthesis (via blockers infusion) have shown that diastolic diameter decreases but overall pump function is maintained [143]. As mentioned earlier, inducible NO (via iNOS) can be another significant source of NO; however, the studies in this area in the context of lymphatics are very limited [143]. It has been shown that NO released by endothelium with acetylcholine (ACh) stimulation inhibits spontaneous contractions of lymphatic vessels.

Sodium nitroprusside (SNP) is one of the most studied nitric oxide (NO) donors. It is believed that the capability of SNP to produce NO depends on its interaction with sulfhydryl-containing molecules available in-vivo [154]. Hence, we used sodium nitroprusside (SNP) to deliver exogenous NO to isolated lymphatic vessels at different doses. Our findings support the idea that NO effect is dose-dependent and the administration of higher doses of NO can suppress all aspects of contractility. Our experimental findings show exogenous NO has an inhibitory effect on lymphatic contractions; however, there is a dose response and higher doses of NO cannot completely abolish contractions. Interestingly, we showed that exogenous NO decreased the amplitude of contractions; however, the predominant effect was on the frequency of contractions. Further, we showed that exogenous NO reduced pumping up to 70% but it is not able to completely abolish contractions. The reduction in contraction frequency is almost twice the reduction in tone and amplitude. The results suggest the exogenous NO diminishes pacemaking activity in line with the established effect of SNP on the reduction of spontaneous transient depolarizations (STDs) frequency and amplitude in lymphatic SMCs [140,155]. The findings also suggest that overproduction of NO production beyond the physiological range, (e.g., NO production from iNOS-expressing cells located surrounding lymphatic vessels in inflammatory scenarios [156]) can inhibit lymphatic contractions, a possible mechanism that may lead to the lymphatic dysfunction in pathological scenarios.

2.2.5 Conclusions

In conclusion, the current study demonstrates the significance of the axial pre-stretch and exogenous NO in lymphatic contractile function and provides new insights into the physiological function of collecting lymphatic vessels. These findings suggest the rat

tail may serve as a useful animal model to test new hypotheses regarding lymphatic health and disease.

CHAPTER 3. A MICROSTRUCTURALLY MOTIVATED CHEMO-BIOMECHANICAL FRAMEWORK FOR LYMPHATIC VESSELS

3.1 Aim 2

To establish **a microstructurally motivated chemo-biomechanical framework** based on the experimental observations in Aim1, to model passive and active responses of rat tail lymphatic vessels to **mechanical/biochemical perturbation** (axial stretch and nitric oxide). There are three milestones for Aim 2 as follows:

3.2 Milestones 1&2:

Milestone 1:

To determine the material parameters that describe the passive constituents of rat tail lymphatics and the variance of these parameters using a microstructurally-motivated model and a bootstrapping technique.

Hypothesis I: We test our hypothesis that a three-fiber family constitutive model including one axial and two symmetric diagonal family of fibers along with a bootstrap technique provides a reliable technique to fit lymphatic multi-axial data and to determine material properties and their respective confidence intervals.

Milestone 2:

To develop a computational framework to model the effect of exogenous NO and axial stretch on lymphatic contractility.

Hypothesis II:

Changes in lymphatic contractility due to axial stretch and NO administration can be modeled via the effects of NO on force production by lymphatic muscle cells and the effects of axial loading on circumferential stretch and length-tension relationships describing lymphatic force production in the circumferential direction.

3.2.1 Introduction

The lymphatic system is composed of a hierarchical network of lymphatic vessels working in parallel to the circulatory system to transport lymph from the interstitial space back to the great veins [18]. The lymphatic network plays a key role in maintaining tissues hemostasis, transport of macromolecules, dietary fat and serves as a route for immune cell surveillance [157]. Once lymph is formed, the network of lymphatic capillaries (initial lymphatics) absorb lymph and ultimately converge to collecting lymphatic vessels that unidirectionally transport lymph back to the great veins [18,79]. The primary lymphatic valve prevents the leakage of absorbed lymph back to the interstitium due to prevailing pressure gradients across the valve [118]. Collecting lymphatic vessels (lymphangions) actively transport lymph via a series of orchestrated contractions.The collecting lymphatic vessels are covered by specialized lymphatic smooth muscle cells that enable the vessels

to propel lymph against an adverse pressure gradient from the interstitium to the great vein [158]. The secondary lymphatic valves separate these collecting ducts to ensure unidirectional flow and to break the hydrostatic pressure [118].

The lymphatic system can adjust the contractile function in response to mechanical and biochemical stimuli. Mechanical stretch due to pressure is known to be a key modulator of lymphatic contractility. It is well documented that the frequency of contractions changes in response to pressure and the active tension changes with stretch for lymphatic vessels [122–124]. In addition, previous studies have demonstrated small molecules such as nitric oxide (NO), histamine, and endothelin-1 (ET-1) play key roles in the regulation of lymphatic contractility [4,125–129]. For example, the effects of endothelial-derived NO and NO production from iNOS-expressing cells have been studied [42,125,130–132]. The effect of endothelial-derived NO on the lymphatic contractility is also well documented via pharmacological inhibition and genetic deletion of eNOS pathway [125,132].

In addition to *ex-vivo* and *in-vivo* studies of lymphatic pumping, computational modeling has emerged as a useful tool to shed light on the salient features of lymphatic function. Several groups have developed models to study lymphatic pumping based on the mathematical models and experimental observations for collecting lymphatic vessels [60,61,70,71,62–69]. These computational models have been used to provide insight into lymphatic pumping in the context of the optimal working condition; however, most of these studies are based on a single experimental observation in an *ex-vivo* or *in-vivo* study and conflicting results have been reported [72,73]. Caulk *et al* developed a computational framework to constitutively model the passive and active mechanics of lymphatic vessels based on the hyperelasticity theory and *ex-vivo* experiments [70]. This framework was

successfully used to fit experimental data from rat thoracic duct. Further, an algorithm was developed to use this framework coupled with a valve model to perform parametric studies of lymphatic adaptation to different loading conditions [71,74].

Given the complexity and regional heterogeneity of the lymphatic system, the regional specificity of experimental data (e.g., contractile and biomechanical data) is crucial to develop reliable models. There is still a pressing need to provide a validated model capturing both biomechanical and biochemical function of lymphatic vessels based on the regional specific data; specifically, experimental data on the dose-dependent effect of exogenous NO on the lymphatic contractions has yet to be incorporated into computational models. This section characterizes the passive biomechanical properties and active contractile function of the rat tail lymphatic vessels in response to transmural pressure and the exogenous NO, and ultimately provides a validated constitutive framework to recapitulate the experimental observations.

3.2.2 Methods

Study of Passive Biomechanical Properties. We used an improved biaxial device that precisely controls transmural pressure, diameter, and axial stretch [81]. A custom LabVIEW program was developed to control transmural pressure via a syringe pump (Harvard) and pressure sensors (1psi SSC series, Honeywell). Linear actuators and XYZ stages (Newport Precision, LTA series and M-461 series) were used to precisely control axial stretch. Using an inverted microscope (2.5x magnification) and a digital camera (Allied Vision Technologies, Marlin F-033B), the active and passive response of vessels to different transmural pressures and axial stretches were captured and save for further

analysis. Axial forces were measured using a 50mN force transducer (Aurora Scientific, Model 400A). Vessels were given ~45-60 min to equilibrate at DMEM/F-12 (Dulbecco's Modified Eagle Medium/Nutrient Mixture F-12 plus Pen-Strep 1:100, pH=7.4 at 37℃) to establish stable contractions. For passive biaxial testing, the solution was changed to Ca^{2+}-free PBS solution (Corning® Phosphate-Buffered Saline, 1X without calcium and magnesium, PH 7.4 ± 0.1) containing 3mM EDTA [70,159]. All vessels were preconditioned by ramping the transmural pressure from 0 to 10 mmHg while at three stretch steps of 10%, 20%, and 30%. A pilot study was used to determine the range of pressure and stretch values for the testing protocols. The pressure-diameter and force-pressure responses at these values resemble the physiological biaxial response of vessels.

Thickness measurement. An inverted microscope (Objective 2.5x) equipped with a camera (Allied Vision Technologies, Marlin F-033B) was used to acquire images of vessels. The vessels were pressurized at ~0.5mmHg and axial stretch was set to one. Images were analyzed using ImageJ software to calculate thickness. The thickness was calculated based on the measurement of internal and external diameters.

Constitutive Modeling. To capture salient features of lymphatic vessel mechanics (e.g., structural stiffness) and to reveal their contribution to lymphatic contractility, we employ a two-dimensional constitutive framework to fit experimental data obtained from the biaxial testing. The mechanical stress within the wall of a lymphatic vessel originates from passive elasticity and active force production by lymphatic smooth muscle cells, namely:

$$\sigma = \sigma_{pas} + \sigma_{act} \tag{1}$$

where σ is totall mechanical stress response, σ_{pas} is the passive component of stress resulting from vessel's elasticity and σ_{act} is the active component exerted by smooth muscle cells. Based on the two-dimensional equiblirium equations for a straight and cylinderical segment, circumferental (θ) and axial (z) components of stress tensor are given as:

$$\sigma_\theta = \frac{Pr}{h} \tag{2}$$

$$\sigma_z = \frac{f}{\pi h(2r + h)} \tag{3}$$

where σ_θ, and σ_z are circumferential and axial stresses respectively; P is the transmural pressure; r is the luminal radius; h is the wall thickness; f is the applied axial force. Based on hyper-elasticity theory, the passive stress tensor can be approximated using the Cauchy stress as:

$$\sigma_{pas} = -p\mathbf{I} + \boldsymbol{F}\frac{\partial W}{\partial \boldsymbol{F^T}} \tag{4}$$

where $\boldsymbol{F}$ is the deformation gradient tensor; W is a scalar function representing the stored energy density for elastic deformations. The deformation gradient components ($F = diag(\lambda_r, \lambda_\theta, \lambda_Z),\ where\ \lambda_r = h/H\ ,\ \lambda_\theta = r/R\ ,\ \lambda_z = l/L$ and (h, r, l) *and* (H, R, L) are thickness, radius and length for the loaded and unloaded vessel respectively) represent

circumferential and longitudinal stretches respectively. Motivated by the recent observation of collagen organization in the rat tail lymphatic vessels, where the collagen fibers are normally distributed with a peak in the axial direction, we chose a three-family stored energy function as:

$$W = b(I_C - 3) + \sum_{i=1,2,3} \frac{b_1^i}{4b_2^i}\{exp[b_2^i((\lambda^k)^2 - 1)^2] - 1\} \quad (5)$$

where b, b_1^i and b_2^i are material parameters, I_C is the first invariant of the right Cauchy-Green strain tensor ($I_C = tr(\boldsymbol{C}),\ \boldsymbol{C} = diag(\lambda_r^2, \lambda_\theta^2, \lambda_z^2)$), $(\lambda^i)^2$ is the stretch of the i^{th} fiber family ($\lambda^i = C_{\theta\theta} sin^2(\alpha^i) + C_{zz} cos^2(\alpha^i)$), where α^i is the fiber angle (please see Ref. ([160]) for details). We tested different number of family fibers (e.g., 2, 3, and 4) and a 3-fiber model (one longitudinal and two symmetric diagonal family of fibers) was found to best capture the data.

To model the active contractile force generated by lymphatic smooth muscle cells, we modified a model proposed by Caulk *et al.* [161] to incorporate the effect of SNP doses on the contractile force generation, namely:

$$\sigma_{\theta,active} = C(SNP) * T_{act} * \lambda_\theta \left[1 - \left(\frac{\lambda_M - \lambda_\theta}{\lambda_M - \lambda_0}\right)^2\right] \quad (6)$$

$$\mathrm{C(SNP)} = \left(\mathrm{b} + \frac{1 - \mathrm{b}}{1 + 10^{(\log(\mathrm{SNP}) - \log(\mathrm{IC50}))}}\right)$$

where T_{act} is a scaling parameter, λ_θ is the circumferential stretch, λ_M and λ_0 are the stretches at which the active force is maximum and minimum respectively. The parameres λ_M and λ_0 were prescribed as the maximum stretch achieved during the passive testing (λ_M =1.85) and the minum circumferential stretch (λ_0 =0.85) during the active testing. As shown by Caulk et al. [70], T_{act} is a function of pressure that is minimum at diastole ($\mathrm{T_{dia}} = \mathrm{T_{act,min}} = f(\mathrm{P}) = \mathrm{a} * \mathrm{P}$) and becomes maximum at systole ($\mathrm{T_{sys}} = \mathrm{T_{act,max}} = \mathrm{T_{act,min}} + \mathrm{a} * \mathrm{P}$) . Parameter b is the maximum due to SNP dose, IC_{50} (inhibitory concentration, 50%) is the dose value where the dose response is half maximal value.

Bootstrapping and Parameter Estimation. Since the lymphatic system shows regional heterogeneity it is crucial to have a robust parameter estimation to identify biomechanical properties and their confidence intervals [100,134]. To determine *best-fit* parameters, a nonlinear regression using function lsqnonlin in MATLAB 2015b (MathWorks, Inc) was used to minimize objective functions as follows

$$error = \frac{\sum_{i=1}^{n}\left[\left(\log\left|\sigma_\theta^{th}\right| - \log\left|\sigma_\theta^{exp}\right|\right)^2 + \left(\log\left|\sigma_z^{th}\right| - \log\left|\sigma_z^{exp}\right|\right)^2\right]}{\sum_{i=1}^{n}\left[\left(\log\left|\sigma_\theta^{exp}\right| - \log\left|\bar{\sigma}_\theta^{exp}\right|\right)^2 + \left(\log\left|\sigma_z^{exp}\right| - \log\left|\bar{\sigma}_z^{exp}\right|\right)^2\right]},$$

where *th* indicates a theoretical value and *exp* denotes an experimental value, σ_θ^t, σ_z are circumferential and axial stress respectively, and overbar indicates the mean value. Since the objective function is the residual sum of squares to the total sum of squares, the cofficient of determination with each specimen are present as R^2 *=1-error*. This means minimizing the error function results in maximizing the R-squared (R^2) value. It should be noted that different groups have defined different error functions [162], however, we

experimented with different objective functions and the above objective function provided better fits both visually and quantitavely.

We also used a non-parametric bootstrapping technique to estimate the confidence interval of nonlinear regression as well as the uniqueness of nonlinear regression. The details of the bootstrap technique for parameter estimation can be found in ref. [163–165]. In brief, to apply the bootstrap technique to biaxial data, a resampling with replacement is used to generate bootstrap replicants that have the same number of observations as the original data set while each data has the same probability to be chosen and thus each data point may be included more than one time. To estimate 95% bootstrap confidence intervals, we used the Bias-corrected and accelerated percentile method (the BCa intervals) which is a second-order accurate interval that corrects for bias and skewness of bootstrap estimates. The number of bootstrap replicants above 1,000 typically provides an accurate estimate. The function bootci in (MathWorks, Inc*)* with 2,000 bootstrap samples was used to calculate the respective confidence intervals of parameters in nonlinear regression. The mathematical details of the BCa correction can be found in [166,167].

3.2.3 Results

Quantification of passive and active biomechanical properties. The three-fiber family constitutive model yielded a good-fit (R^2=0.90±0.03) for the rat tail lymphatic vessels (Figure 3.1, Table 3.1). Supporting the previous experimental observation, our modeling results indicate that a three-fiber family model was sufficient to provide a good fit of biaxial data [168]. Based on the estimated parameters, the axial collagen fiber family (C_1^1= 2.05±1.76 (kPa), C_2^1=1.2×10^{-3}±1.0×10^{-3} (kPa)) and two symmetric diagonal fiber

families (C_1^2 = 1.21±0.82 (kPa), C_2^2 =1.5×10^{-3}±6.7×10^{-4} (kPa), and α =31.6°±4.9°) significantly contribute to the load bearing function of lymphatic vessels; however, the amorphous matrix had a much smaller contribution (C=5.4×10^{-7}±4.4×10^{-8} (kPa)). This suggest the longitudinal and diagonal fibers show a comparable contribution to the load bearing function; however, the amorphous matrix has a smaller contribution (Fig. 3.2A). The mentioned values are based on the average values of best fits for parameter estimation and the avarage of bootstrapping values for the respective confidense intervals (Fig. 3.2A and Table 3.1). In addition, a representative estimation of respective confidence intervals using bootstrapping via 2,000 bootstrapping is shown in Fig. 3.2B. Note that we also considered a four-fiber family model, following previous studies ref. [75,160,169]), allowing an additional family of collagen fibers beyond the axial and diagonal collagen families (e.g., circumferential collagen). However this does not improve the descriptive capability of the constitutive model (results not shown).

Table 3. 1 Passive material parameters estimations respective confidence intervals for rat tail lymphatic vessels using a three-fiber family constitutive model. The objective function for the optimization was defined as Error=1- R^2 value, calculated based on the biaxial data and estimated parameters. The best fit values along with the bootstrapped confidence intervals are presented for each specimen. The estimated parameters and associated R^2-values exhibit consistency indicating reasonable fits.

Specimen		Elastic Fiber	Axial Collagen		Diagonal Collagen			
		$c(kPa)$	$c_1^1\ (kPa)$	$c_2^1\ (kPa)$	$c_1^2\ (kPa)$	$c_2^2\ (kPa)$	$\alpha(degree)$	R^2
1	*best fit*	5.02E-07	4.94E+00	5.78E-04	1.90E+00	5.93E-04	25.28	0.9258
	BCa interval	5.00E-07	2.93E+00	4.27E-04	1.71E+00	5.43E-04	25.04	
		6.27E-07	7.71E+00	7.44E-04	2.60E+00	6.23E-04	25.73	
2	*best fit*	6.03E-07	1.69E+00	1.15E-03	3.14E-01	1.99E-03	31.14	0.9184
	BCa interval	5.31E-07	1.20E+00	7.11E-04	1.96E-01	1.87E-03	30.948	
		9.95E-07	7.50E+00	1.25E-03	4.06E-01	2.16E-03	31.31	
3	*best fit*	5.66E-07	1.74E+00	8.30E-04	1.50E+00	2.12E-03	34.87	0.8768
	BCa interval	3.75E-07	1.23E-01	1.92E-04	1.15E-01	3.29E-10	34.44	
		9.31E-07	1.62E+01	1.89E-03	8.94E+00	4.70E-03	66.68	
4	*best fit*	5.41E-07	1.78E+00	4.67E-04	3.67E-01	1.95E-03	37.92	0.9116
	BCa interval	5.10E-07	1.13E+00	3.29E-04	2.91E-01	1.85E-03	37.73	
		7.78E-07	2.32E+00	5.71E-04	4.12E-01	2.03E-03	38.03	
5	*best fit*	5.00E-07	1.18E-01	2.99E-03	1.98E+00	1.10E-03	28.95	0.8605
	BCa interval	4.69E-07	1.71E-12	1.30E-03	9.40E-02	2.67E-04	28.95	
		1.00E-06	2.49E+00	1.56E-02	4.46E+00	2.68E-03	28.95	
	Average	5.43E-07	2.05E+00	1.20E-03	1.21E+00	1.55E-03	31.63	0.8986
	SE	4.41E-08	1.76E+00	1.03E-03	8.17E-01	6.70E-04	4.94	0.0284

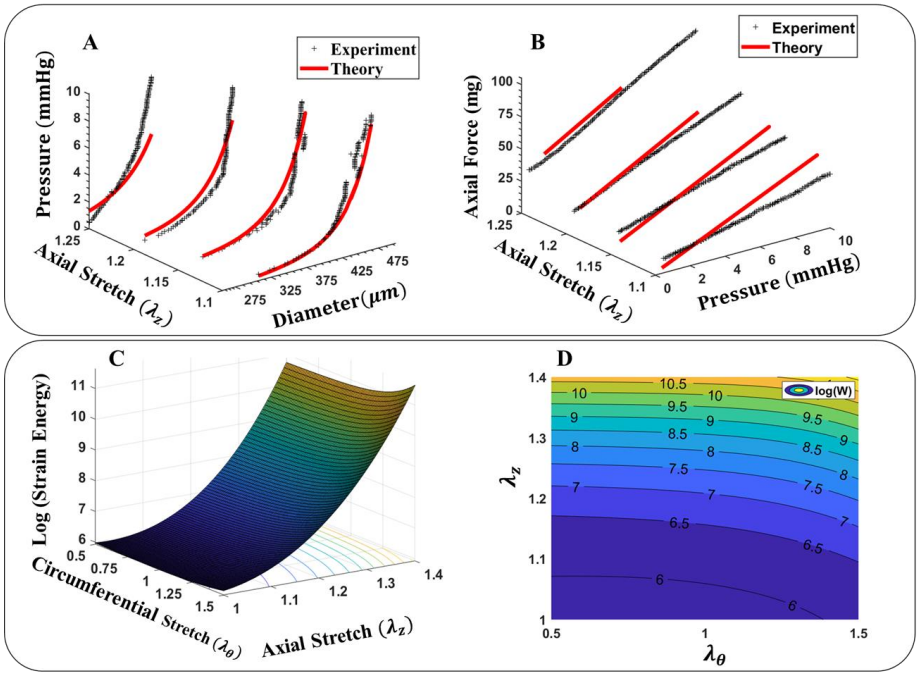

Figure 3. 1 A representative plot of experimental biaxial testing and respective fitting results using a three-fiber family constitutive model including pressure-diameter measurements at different axial stretches and their respective theoretical values (Panel A), axial force-pressure measurements at different axial stretches and their respective theoretical values (Panel A), the stored strain energy was calculated based on the estimated parameters from sample 1 (Panel C) and a 2-D iso-contour representation of strain energy as a functional of circumferential and axial stretches (Panel D). The plus symbols indicate experimental data and solid lines denote theoretical values based on the *best fit* values (sample 1 in Table 3.1).

Table 3. 2 Structural parameters associated with the unloaded geometry for rat tail lymphatic vessels presented in Table 1. The diameter, thickness, and length were estimated based on images obtained using an inverted microscope 2.5X-10X and analyzed using the LabView and ImageJ.

Specimen	Length (mm)	Diameter (µm)	Thickness (µm)	Thickness/Diameter Ratio
1	2.76	252	19	0.08
2	3.40	231	11	0.05
3	2.64	252	25	0.10
4	2.65	315	24	0.08
5	2.03	206	20	0.10
Average	2.70	251.20	19.89	0.08
SE	0.48	40.38	5.55	0.02

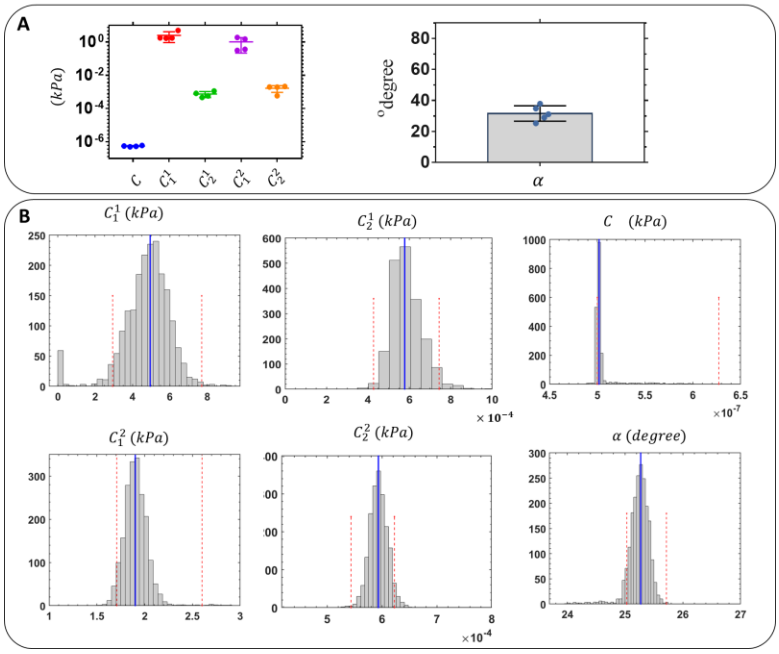

Figure 3. 2 Material properties based on the fitted experimental biaxial data using a three-fiber constitutive model for rat tail lymphatic vessels (n=5) including best-fit values of model parameters for five samples (Panel A), and a representative estimation of respective confidence intervals using bootstrap technique showing the results of 2,000 bootstrapping along with the best fit-values (blue line) and the BCa confidence intervals for each parameter (red dashed lines) based on the specimen 1 in Table 1 (Panel B).

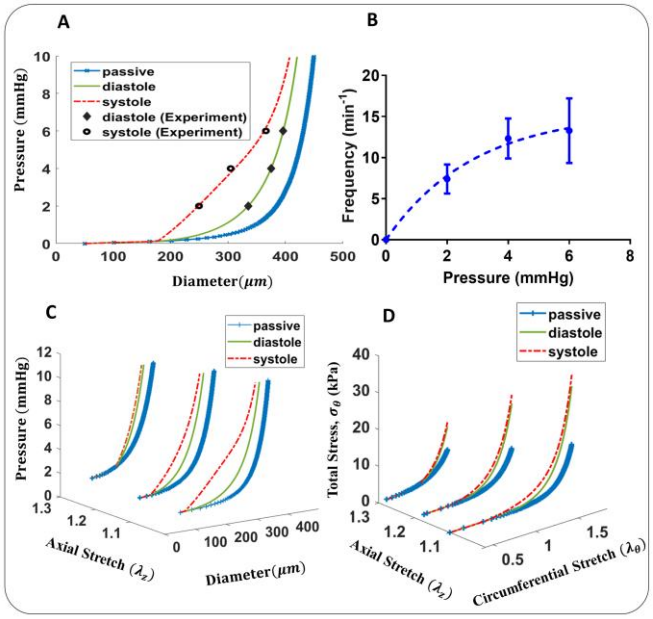

Figure 3. 3 Modeling active contractile function of rat tail lymphatics based on the passive biomechanical data and active contractile data. The pressure-diameter curves for passive behavior including passive, diastolic and systolic curves were plotted for three different values of axial stretch (Panel A) and fitting results of contraction frequency in response to the transmural pressure (Panel B). The passive parameters were obtained based on the constitutive model (Eqs. (8-12)) using the fitted parameters from sample 1 in Table 1, and active diastolic and systolic curves were computed based on the active-tension model, Eq. (6) where parameter T_{act} was determined to be T_{sys}= T_{dia} + 1.6498 (kPa) at systole and T_{dia}=0.87*P(mmHg) at diastole, estimated based on an algorithm to fit the contractile data for three pressures of 2, 4, and 6 mmHg at 10% stretch in Fig.2 7. An exponential equation using nonlinear regression (FREQ= 15.51*(1-exp(-0.3493*Pressure), R^2=0.52) was used to fit experimental data. The pressure-diameter curves for passive behavior including passive, diastolic and systolic curves were plotted for three different values of axial stretch (Panel C) and the respective computed total circumferential stresses were plotted as a function of circumferential and axial stretches (Panel D).

Constitutive modeling of active contractile function and its response to NO.

As shown by Caulk et al [75], diastolic tension increase with increased pressure and hence a the diastolic T_{act} is a function of pressure. We used the average tone (Tone=7.6% at 3mmHg, Fig. 2.8B) to fit the linear relation between the diastolic T_{act} and transmural pressure ($T_{dia} = 0.87 * \mathrm{P(mmHg)}$ (kPa)). Similarly, the average ejection fractions (44.6% at 2mmHg, 34% at 4mmHg, 14.7% at 6mmHg, Fig. 2.7C) were used to obtain systolic T_{act} ($T_{sys} = 0.87 * \mathrm{P(mmHg)} + 1.6498$ (kPa)). Modeling results including

systolic, diastolic and passive diameter-pressure curves along with respective experimental data are shown in Fig. 3.3A. In addition, a nonlinear regression ($\mathrm{FREQ}(\mathrm{min}-1) = 15.51 * (1-\exp(-0.3493 * \mathrm{P(mmHg)}), \mathrm{R}^2 = 0.53$) was used to fit the frequency data (Fig.3.3B). In addition, modeling results at different axial stretches were shown in Fig.3.3C. Pressure-diameter curves showed that an increase in the axial stretch from 10% to 30% results in the reduction of systolic diameter and consequently the ejection fraction decreases from ~45% to less than 1% (Fig. 3.3C). Further, respective stress-strain curves showed the total circumferential stress decreased with increased axial stretch (Fig. 3.3D). Similarly, to model the effect of SNP on active stress, changes in contractile data due to SNP doses (Fig. 2.8B and D) were used to fit a dose-response curve (Fig. 3.4A). The correction parameter (C(SNP)) was calculated at each dose and finally, nonlinear regression was used to fit a dose-response curve (C(SNP)=0.80+0.2/(1+10^(log(SP)+6.42)), R^2=0.98). The results suggest that the half maximal effective concentration is~ 10^{-6} (M) and approximately 20% change in active stress results in a ~30% reduction in diastolic and systolic diameters (Fig. 3.4B).

Parametric simulations of the effect of axial stretch and SNP on lymphngion contractions. The constitutive model was incorporated into a previously developed algorithm of lymphangion contraction. The details can be found in Caulk et al [71]. Matlab codes are provided in the Appendix as well. Parametric simulations predict that an increase in the axial stretch results in a decline in amplitude of contractions, pressure and lymphatic flow (Fig. 3.5 A-D). This prediction is supported by our experimental observation that axial stretch decreases lymphatic contractility. Interestingly, computational simulation predicts that an axial stretch equal to 30% significantly decreases the amplitude of contractions

which is line with experimental observations. Similarly, the modified constitutive framework was used to model the effect of SNP at a dose of 10^{-4} on contractions (Fig. 3.6 A-D). Pressure-volume and flow-time curves show that flow significantly decreases after SNP administration.

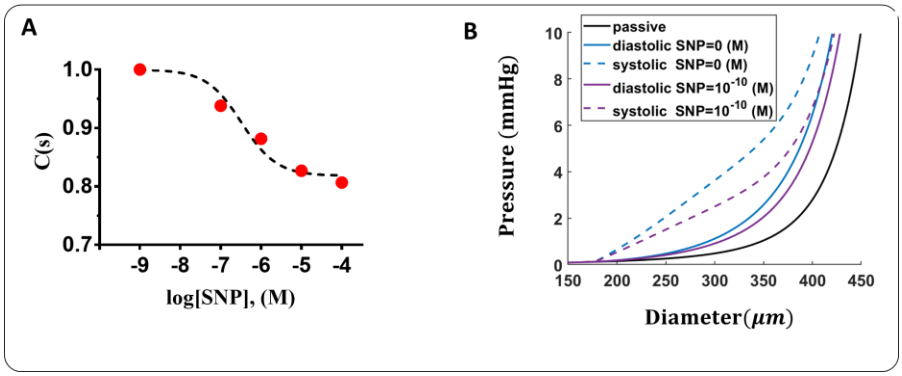

Figure 3. 4 Modeling the effect of SNP on the active contractile behavior of rat tail lymphatic vessels. A dose-response curve using a dose-dependent equation fits the correction factor (Eq. (13)) modeling the decrease in active contractile stress C(SNP)=0.80+0.2/(1+10^(log(SP)+6.42)), R^2=0.98) due to SNP administration (Panel A). Modeling results show the maximal changes in systolic and diastolic diameters in response to a 10% decrease of active stress at SNP=10^{-4} (M) (Panel B).

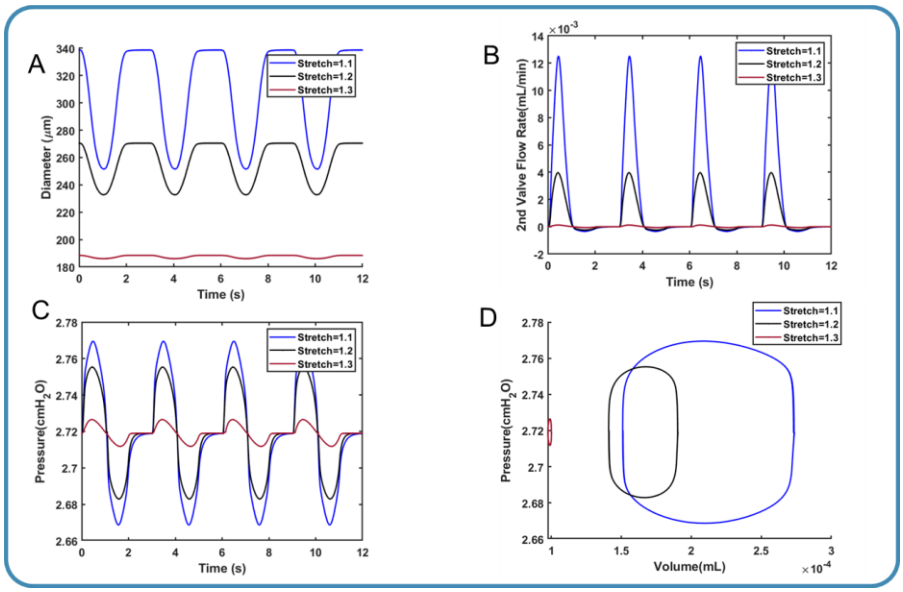

Figure 3. 5 Parametric simulations for a contracting lymphangion using the constitutive modeling. Simulation results show amplitude (Panel A), flow (Panel B), pressure (Panel C) and ejected volume (Panel D) decreases with the increase in axial stretch.

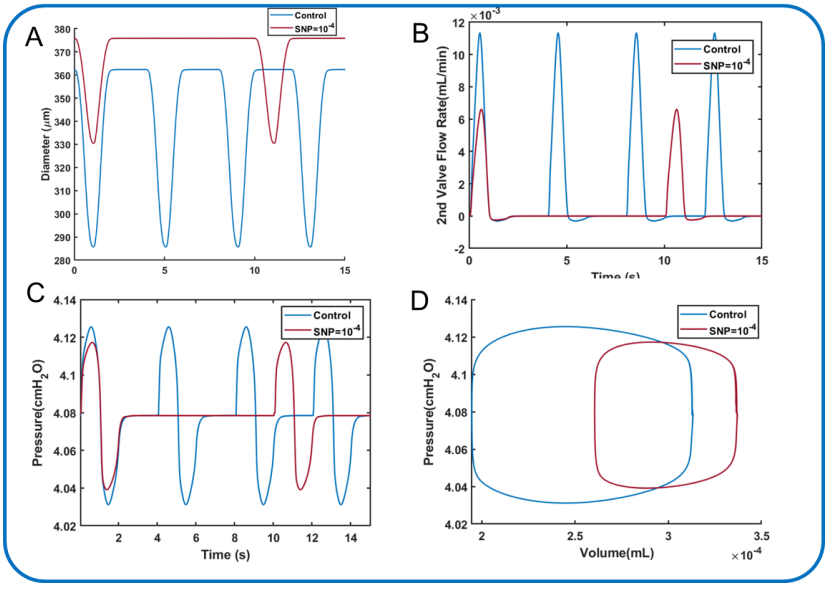

Figure 3. 6 Modeling the effect of SNP on a contracting lymphangion. Amplitude and frequency of contractions decrease with SNP (Panel A) and flow and pressure, and ejected volume decrease with SNP administration (Panels B-D)

3.2.4 Discussion

Passive mechanics of lymphatic vessels and its contribution to lymphatic transport. It is essential to develop a basic knowledge of lymphatic vessel mechanics to have a better understanding of lymphatic transport in the context of lymphatic physiology and pathophysiology. Some efforts have been made to study the role of passive mechanics of lymphatic vessels for elucidating the modes of lymphatic regulations [75,114,115,120]. Ohhashi et al. [120] have shown that lymphatic vessels from the bovine mesentery manifest a nonlinear relationship between pressure and diameter, being very distensible at lower pressures and less distensible at larger pressures. More recent studies report similar findings in the rat mesentery [115], rat thoracic duct [75], and human pelvic vessels [114]. Based on the passive pressure-diameter relationship in the rat mesentery, the normal operating pressure is estimated to be between 0 to 5cm H_2O, a range in which the vessel is very distensible [115]. Caulk et al. performed biaxial testing on the lymphatic vessel from rat thoracic duct and shown that the nonlinear transitional response is a function of the axial stretch and pressure [75]. They show that at the lower axial stretch the transition occurs at low pressures (<5cm H2O); however, the pressure-diameter relationship in rat thoracic lymphatic vessels transitions to a linear shape at the axial stretch above 60%. Similar trends are observed for the human pelvic lymphatic vessels with some variations [114]. Our biaxial characterization of passive biomechanical properties of rat tail lymphatic vessel is qualitatively similar to those of rat mesentery and thoracic duct; however, the rat tail

lymphatic vessels are very sensitive to the level of the axial stretch and for the values above 30%, the vessel becomes stiff and doesn't noticeably change the passive diameter over physiological ranges of transmural pressure. The axial forces in the rat tail lymphatic vessel can reach ~1mN at 25% stretch ($p=10$mmHg) comparing to ~1mN at 50% stretch ($p=10$mmHg) for the rat thoracic duct [75]. Similarly, the human pelvic lymphatic vessel is very sensitive to the axial stretch (~1mN at 20% stretch versus ~ 4mN at 30% stretch, $p=5$ cm H_2O) [114].

We fit the passive biaxial data using a fiber-family constitutive framework, originally adapted from Baek et.al and Caulk et. al [75,169], but adapted to including one axial and two symmetrical parallel collagen fiber families, as well as one component for amorphous matrix contribution. In addition, the estimated parameters for the axial and diagonal collagen fibers implies the axial fiber family plays a significant role in the load-bearing function. The significance of axial stretch in passive behavior of lymphatic vessels is in agreement with our recent quantification of collagen fiber orientation in the rat tail lymphatic, where the vessels have a predominant organization of collagen fibers in the axial direction and experience the axial prestretch ~20% in-situ [168].

Further, bootstrapping was used to obtain the confidence intervals of estimated parameters. Our approach for parameter estimation suggests that a three-fiber family along bootstrapping technique can be used to estimate intra-specific biomechanical parameters. Particularly, this is important because the variability in lymphatic properties is not uncommon. The variability in the estimated parameters from different rat tail lymphatic vessels have smaller variations and represent a predictive improvement comparing to those computed by Caulk et al [75], which had variations that ranged…. Previously, the

constitutive approach along with bootstrapping has been successfully used to determine changes in the biomechanical properties in the context of vascular remodeling in aging, and aneurysm [163,165]. Our results suggest that a three-fiber family along with the bootstrapping technique can be a useful tool not only to establish a descriptive framework to study the regional heterogeneity in the material properties of lymphatic vessels but also to study changes in those properties in the pathological scenarios.

The rat tail as a novel lymphatic system to study NO effect on lymphatic contractions. Modeling approaches have been used to investigate the regulatory mechanism of NO on lymphatic contractility [72]. Kunert et al [72] presented a model describing two complementary feedback mechanisms to modulate lymphatic contractions involving: (i) a contraction triggered by Ca^{+2} rise due to a stretch (ii) a shear-mediated response to inhibit contractions via NO production. Specifically, this model predicts that NO is essential for the phasic contractions and without NO production phasic contractions are completely abolished; however, the modeling results have been questioned based on the ex-vivo studies of NO synthesis blockade showing spontaneous contractions develops and even improves in the absence of endothelial-derived NO [170,171]. The rat tail has previously been used to study the effect of dermal NO donor (GTNO) on the pumping function of the lymphatic vessels [172,173]. Using *in-vivo* experiments, it was shown that the pumping pressure, that is the maximum pressure that can be achieved along a lymphatic chain to maintain lymphatic flow, decreases with the administration of dermal NO [172]. Computational simulations and parametric studies based on the rat thoracic biomechanical properties suggested that the decrease in the amplitude of active contractions can explain the reduction in pumping pressure. In addition, we have recently used the rat tail to show

that the lymphatic vessels experience axial pre-stretch [168]. This study provides the *ex-vivo* experimental data on the isolated lymphatic vessels and complements our previous knowledge regarding the effect of exogenous NO on lymphatic contractility. We showed that the administration of exogenous NO suppresses all aspects of lymphatic contractility in a dose-dependent way. Further, the constitutive framework and estimated parameter support the significance of the axial stretch in the lymphatic function. The constitutive framework and specific experimental data for the rat tail lymphatic vessel pave the way for the future experimental and computational studies both in the context of lymphatic physiology and pathophysiology. In particular, the recent results from rat tail lymphatics suggests that the rat tail is a promising option to develop animal models of lymphatic dysfunction. Specifically, the study of lymphatic remodeling due to the surgical interventions in the context of lymphatic pathologies such as lymphedema or other inflammatory scenarios remains an exciting area for future studies. The presented specific experimental data along with the constitutive framework provide a basis for such studies.

CHAPTER 4. THE RELATIONSHIP BETWEEN LYMPHANGION CHAIN LENGTH AND MAXIMUM PRESSURE GENERATION ESTABLISHED THROUGH IN VIVO IMAGING AND COMPUTATIONAL MODELING

4.1 Aim 2: Milestones 3

To establish **a microstructurally motivated chemo-biomechanical framework** based on the experimental observations in Aim1, to model passive and active responses of rat tail lymphatic vessels to **mechanical/biochemical perturbation** (axial stretch and nitric oxide). The third milestone is as follows::

Milestones 3: To study the response of a lymphangion chain to different loading conditions based on the constitutive modeling approach.

Hypothesis III: We test the hypothesis that the maximum pressure that can be achieved along a lymphangion chain correlates with lymphangion number and lymphatic muscle contractility in the chain.

4.1.1 Introduction.

Computational models have provided new insight into the mechanical, material, biological and geometric parameters that influence the effectiveness of the lymphatic pump under different physiologic scenarios [62,65,174–176]. Computational models are useful tools to help integrate observations made across different experimental platforms and can guide experimental design by identifying key parameters that are likely to have the most

profound effect on pumping for further validation. For example, computational studies have predicted that a longer chain of lymphangion can pump against higher opposing pressure gradients, a phenomenon that has also been reported in isolated vessel studies. However this relationship between chain length and pumping pressure has yet to be established in vivo. The major objective of this study was to determine if the relationship exists in vivo and to use a computational model to test the hypothesis that the increase in maximum pressure generation along a chain of lymphangions correlates with lymphangion number and active tension of lymphatic smooth muscle cells.

To bridge the gap between the precise functional measurements that can be made in isolated vessels with the physiologic relevance of in vivo approaches, we have developed a computational model of lymphatic pumping populated with experimental data of lymphatic vessel biomechanics taken from isolated vessels. We then challenge this model in vivo using near infrared imaging of lymphatic pump function under normal conditions and with treatment by a dermally delivered nitric oxide donor. By combining both computational modeling and a new near-infrared imaging (NIR) imaging approach in which we measure lymphatic pumping pressure at multiple locations along a lymphangion chain, we establish an approach to approximate lymphatic muscle force generation in vivo. We establish an approach to approximate lymphatic muscle force generation in vivo through non-invasive measurement of maximum pressure generation along a chain of lymphangion.

4.1.2 Methods

Pressure Measurement System

To evaluate the maximal pressure generation of lymphangion chains in-vivo, we utilized a previously described method to quantify lymphatic pumping pressure [177]. Briefly, these methodologies involve a closed-loop lymphatic pressure measurement system that was designed utilizing a commercially available pressure cuff (Kent Scientific, Torrington, CT). The pressure cuff was attached to a 5 mL BD luer-lock syringe via plastic tubing and to a pre-calibrated pressure transducer (Honeywell Sensing and Control, Morristown, NJ). The pressure transducer was connected to a data acquisition (DAQ) device (National Instruments (NI), Austin, TX) and pressure values were read into a LabView virtual instrument (VI) (NI, LabView 2014 32-bit). These real-time pressure readings were used to control the serial command output to the syringe pump (Harvard Apparatus PHD 2000 Infusion/Withdraw 70-2001). The difference between the desired pressure and the sampled pressure was used to control the flow rates on the syringe pump to subsequently inflate or deflate the pressure cuff.

To determine the presence or absence of lymph flow at various occlusion pressures, the vessels were imaged with a lymphatic near-infrared (NIR) imaging system as described previously [177,178]. In brief, a diode driver and temperature control box powered a 1 W 808 nm laser diode and a 20° beam diffuser (Thorlabs, Newton, NJ), which provided excitation light. This achieved a uniform excitation field of approximately 75 cm^2 with less than 1.9 mW/cm^2. An Infinity K2/SC video 2.15x magnification microscope lens (Edmund Optics, Barrington, NJ) and a bandpass filter (CW: 840 nm, FWHM: 15 nm, Omega Optical, Brattleboro, VT) were attached to a PIXIS 1024B back-illuminated CCD camera (Princeton Instruments, Trenton, NJ) to capture fluorescence emission centered at 840 nm.

Experimental Protocol

All animal procedures were carried out at the Georgia Institute of Technology, Atlanta, Georgia and were reviewed and approved by the Georgia Institute of Technology Institutional Animal Care and Use Committee. A standardized procedure to quantify pumping pressure was carried out on nine week old male Sprague Dawley (Charles River, Wilmington, MA) rats. To minimize light scattering, a depilatory lotion was used to remove hair in the region of interest on the tail one day prior to experimentation. Rats were anesthetized with an intramuscular injection of diazepam (2.5 mg⁄kg) followed by a cocktail of fentanyl (0.12 mg⁄kg) and droperidol (6 mg⁄kg). After waiting for approximately 10 minutes for the anesthetics to take effect, the rat was positioned under the camera. Animals in the nitric oxide treatment group received a topical application of 500 mg glyceryl trinitrate ointment (GTNO, 0.2% wt⁄wt, Rectogesic, Care Pharmaceuticals) applied to the entirety of the tail.

The proximal edge of the pressure cuff was placed 4 cm, 8 cm, or 12 cm from the distal tip of the tail. The rat was positioned so that the field of view was immediately proximal to the cuff (Figure 4.1). A mixture of 30 µL of ICG/albumin solution (150 µg/mL ICG (Acros Organics, Geel, Belgium) and 60 g/mL bovine serum albumin (MP Biomedicals, Auckland, New Zealand) dissolved in deionized water was injected intradermally at the tip of the tail.

Image acquisition began just prior to intradermal injection of the dye with a field of view that included the edge of the cuff and the proximal region (Fig. 4.1). Once steady-state fluorescence was established, a predetermined sequence of pressure cuff applications was administered to the tail. Specifically, the pressure was increased to 80 mmHg for 10 minutes to allow for the proximal vessel to completely empty its contents. After holding

for 10 minutes at 80 mmHg, the pressure was quickly decreased to 55 mmHg and then subsequently decreased in decrements of 2.5 mmHg, holding at each pressure step for 60 seconds, until the pressure value reached zero.

Images of the tail were captured by the NIR imaging system throughout the experiment at a frame rate of 1 fps with a camera exposure time of 50 ms. After the first frame was captured, a region of interest (ROI) was selected that was positioned just proximal to the pressure cuff, over the fluorescent collecting vessel. The mean intensity within the ROI was recorded and used in conjunction with the pressure data to evaluate lymphatic pumping pressure. Effective pumping pressure was calculated using two points as described previously [177]: the minimum intensity value during occlusion at 80 mmHg and the maximum intensity value after flow was restored during deflation. The average of these two values was the intensity threshold for flow restoration. The pressure at the time where the intensity rose to equal this intensity threshold was the effective pumping pressure of the collecting lymphatic vessel. Animals were euthanized at the end of experiments using carbon dioxide (CO2).

Statistical Analysis.

Statistical significance between measurement taken at various locations was determined through a Kruskal-Wallis with a post-hoc Dunn's test for multiple comparisons. The significant difference between the control and GTNO data sets was evaluated using the extra sum of squares F-test on the quadratic best-fit regressions of the data. For this test, the restricted model was a single quadratic regression for both data sets, corresponding to the null hypothesis that the control and GTNO sets can be sufficiently described by a single

quadratic regression. The full model was two quadratic equations for control and GTNO respectively, corresponding to the hypothesis that control and GTNO data sets were best described with two distinct quadratic regressions. The F-statistic was computed from the sequential sum of squares for the two models. To determine statistical significance, P-value was computed from the F-statistic with a $P < 0.05$ corresponding to a rejection of the null-hypothesis. All statistical computations were performed in Prism software (GraphPad Software, La Jolla, CA).

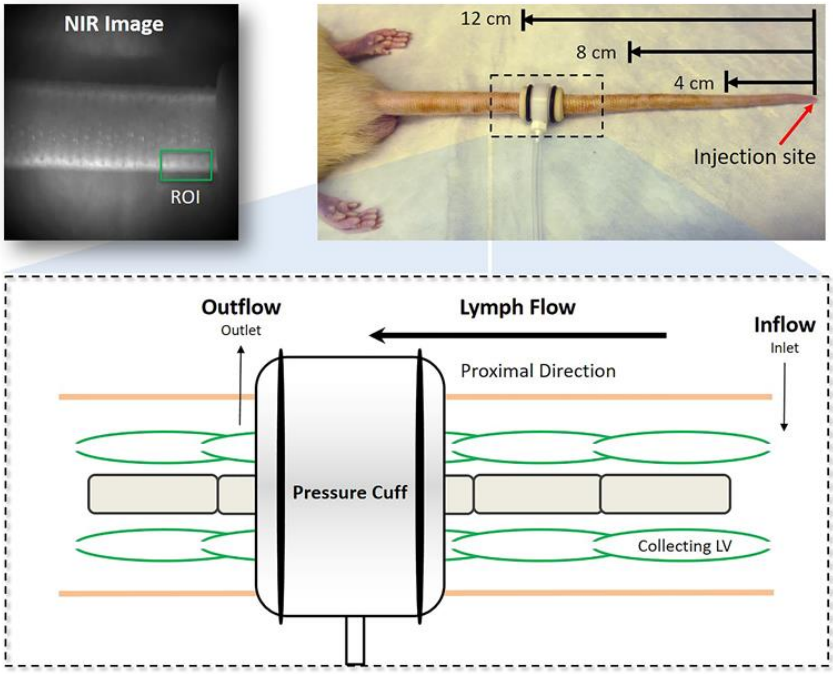

Figure 4. 1 Experimental set-up for measuring lymphatic pumping pressure. The pressure cuff is positioned at various locations measured from the tip of the tail. Flow restoration is imaged by capturing the return of fluorescence into the collecting vessel in a region proximal to cuff. The pressure at which flow restoration is observed is reported as the effective lymphatic pumping pressure and compared to Pb in the computational model.

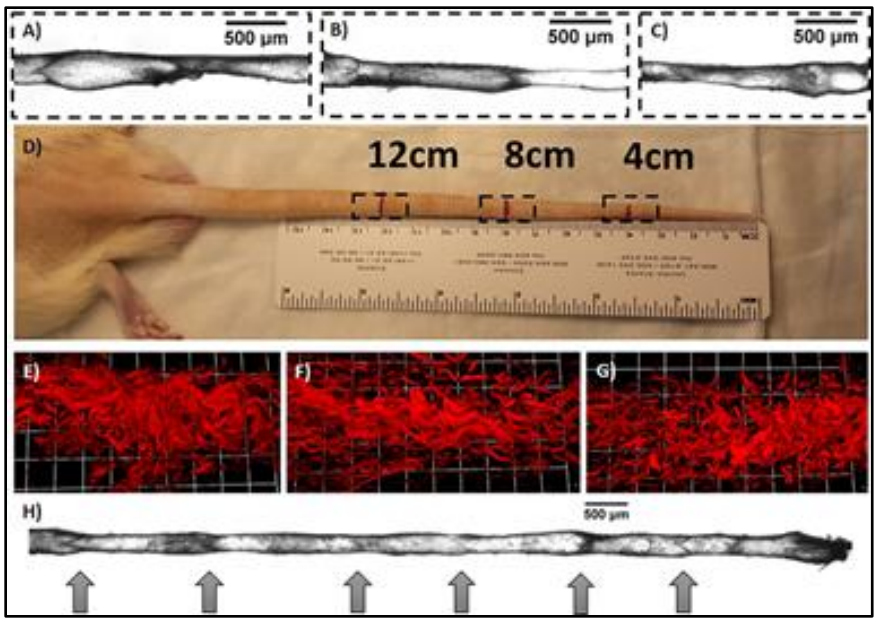

Figure 4. 2 Geometric and micro-structural properties of rate tail lymphatics along various regions of the tail. A) – C) Cannulated lymphatic vessels isolated from regions 12 cm, 8 cm, and 4 cm from the tip of the tail respectively as shown in D). E) – G) Second harmonic generation images of collagen microstructure of vessels isolated from regions 12 cm, 8 cm, and 4 cm from the tip of the tail respectively. H) A chain of lymphangions showing typical valve spacing along the length of the chain.

Model Theoretical Framework. Our theoretical framework consists of a lump-parameter model for lymph transport, a 2D, non-linear, elastic, homogeneous, anisotropic model over finite deformation for the passive mechanics of the vessel wall, and a Rachev-Hayashi model for the active, contractile behavior of the vessel wall.

Lymph Transport and Valve Function. Lymph is transported through chains of lymphangions, separated by intraluminal one-way valves. Assuming fully-developed Newtonian flow, the Poiseuille law is used to calculate flow rate, which has been shown to be a good approximation in regions away from valves. The lymphatic valve imposes a variable resistance to flow during leaflet movements. This resistance becomes minimum during valve opening and maximum during the closure, while the opening/closure behavior is a function of trans-valvular pressure. The lumped model of valve resistance originally

proposed by Bertram et. al. is used to simulate the role of one-way valves. The valve resistance is a sigmoidal curve, which is a function of pressure drop along the valve, defined as:

$$R_V = R_{Vn} - R_{Vx}\left[\frac{1}{1+exp\left(-s_o\left(\Delta p_V - \Delta p_o\right)\right)} - 1\right] \tag{7}$$

where R_{Vn} is the resistance of fully open valve, R_{Vx} is the resistance of fully closed valve, s_o is a parameter associated with the rate of opening and closure of valves, Δp_V is the pressure drop across the valve; Δp_o is the pressure drop at which the valve opens or closes.

Passive contribution of extracellular matrix

The passive circumferential and axial components of the 2-D Cauchy stress in the framework of 2D finite elasticity of an incompressible solid are expressed as:

$$\sigma_{\theta\theta}^{pas} = 2C_{\theta\theta}^{e}\frac{\partial W}{\partial C_{\theta\theta}^{e}} - 2C_{rr}^{e}\frac{\partial W}{\partial C_{rr}^{e}} \tag{8}$$

$$\sigma_{zz}^{pas} = 2C_{zz}^{e}\frac{\partial W}{\partial C_{zz}^{e}} - 2C_{rr}^{e}\frac{\partial W}{\partial C_{rr}^{e}} \tag{9}$$

where $\mathbf{C}^{e}$ is the right Cauchy-Green strain tensor defined as $\mathbf{C}^{e} = diag\{\lambda_r^2, \lambda_\theta^2, \lambda_z^2\}$, where $\lambda_r = h/H$, $\lambda_\theta = d/D$, and $\lambda_z = l/L$, h and H are the loaded and unloaded thickness, d and D are the loaded and unloaded diameter, and l and L are the loaded and unloaded

length of the lymphangion, respectively; W is the strain energy density function which is adapted from the four-fiber family strain energy density function as:

$$W = b(I_{C^e} - 3) + \sum_{k=1,2,3,4} \frac{b_1^k}{4b_2^k}\{exp[b_2^k((\lambda^k)^2 - 1)^2] - 1\} \qquad (10)$$

where b is a constant associated with elastin-dominated amorphous matrix; $I_C = C_{rr}^e + C_{\theta\theta}^e + C_{zz}^e$ is the first invariant of $\mathbf{C^e}$; b_1^k, and b_2^k are material parameters associated with locally parallel collagenous fibers, $(\lambda^k)^2 = C_{\theta\theta}^e \sin^2(\alpha^k) + C_{zz}^e \cos^2(\alpha^k)$ and α_k is the direction of k^{th} fiber. In this framework, the average circumferential and axial stresses are

$$\sigma_{\theta\theta} = \frac{Pd}{2h} \qquad \text{and} \qquad \sigma_{zz} = \frac{f + \pi P d^2/4}{\pi h(d + h)} \qquad (11)$$

where *P* and *f* are transmural pressure and axial force, respectively.

Active contribution of smooth muscle cells

The lymphatic smooth muscle cells modulate contractile force generation in response to changes in transmural pressure of the vessels. A modified length-active tension relationship which was originally proposed for arteries by Rachev and Hayashi was adapted as described previously [70]. In this framework, active circumferential stress is expressed as

$$T_{\theta\theta}^{act} = T_{act}(t)\lambda_\theta \left[1 - \left(\frac{\lambda_M - \lambda_\theta}{\lambda_M - \lambda_0}\right)\right] \quad (12)$$

where $T_{act}(t)$ is the activation parameter as a function of time that depends on the degree of muscle activation in response to variation in intensity of stimuli (e.g., intracellular calcium), which contributes to phasic contraction and tonic constriction, λ_θ is elastic circumferential stretch, λ_M is the stretch at which force generation is maximum and λ_0 is the stretch at which force generation ceases.

Assuming a cosine function for time-dependency of stimulation (e.g., intra-cellular calcium response) during phasic contraction and a constant parameter for contribution to tonic contractions, parameter $T_{act}(t)$ is written as:

$$T_{act}(t) = \begin{cases} \frac{T_{phasic}}{2}\left[1 - \cos\left(\frac{2\pi}{t_c}t\right)\right] + T_{tonic} & \text{during phasic contractions} \\ T_{tonic} & \text{during tonic constrictions} \end{cases} \quad (13)$$

where T_{phasic} and T_{tonic} regulate the magnitude of maximum phasic contractions and tonic constrictions, respectively; t is time and t_c is period of contraction. Additionally, a parameter t_r is defined as the refractory period to separate consecutive contractions.

Morphological and Biomechanical parameters

Since circumferential stress depends on the unloaded configuration of lymphangion, the mean unloaded morphological parameters (diameter, thickness and length) in rat tail lymphatics were quantified from dissected collecting vessels (Figure 4.2, Table 4.1). Male Sprague–Dawley rats weighing between 300 and 350 g were used for experiments, similar to those used for the in vivo measurement of effective pumping pressure. The rats were anaesthetized with a combination of a solution of fentanyl plus droperidol (0.3 mL kg−1 I.M.) and diazepam (2.5 mg kg−1 I.M.). To isolate lymphatic vessels from a tail region, an incision was made in the tail skin under the lateral caudal vein at the base of the tail to ligate lymphatic vessels to prevent them from leakage and keep them under pressure for easy identification. Tail skin with attached lateral caudal veins, arteries and lymphatics was removed from both sides of tail, the bone was discarded but tip of the tail was kept intact. Two stripes of skin with the vessel bundle were placed in a Petri dish (150x15mm) coated with Sylgard and filled with DPBS. The skin was pinned down to the bottom of the dish to expose vessels bundle on top. Lymphatic segments located at 4cm, 8cm, and 12cm from the tip of tail were identified usually lateral to the lateral caudal vein, as vessels were filled with near transparent fluid inside (lymph). Then they were carefully separated from blood vessels and nerves under a stereoscope using microsurgical forceps and scissors and cleaned (with caution not to grab or pinch vessels) from adipose and other connective tissue. The segment of tail lymphatic vessels without branches was cut and transferred to a vessel chamber, where it was cannulated and tied with 11 sizes of the surgical suture to ~200um glass cannulas and used for imaging. Collagen distribution was imaged with three-dimensional multiphoton imaging using second harmonic generation as described previously. Given that the microstructure and

Table 4. 1 Parameters associated with biomechanical properties, geometry and valve models. The active parameters were taken from published values of thoracic duct in rats, valve parameters were taken from published measurements in rat mesenteric lymphatics, while geometric properties where measured directly in rat tail lymphatics.

Biomechanical Parameter (Rat Thoracic Duct)				***Geometrical Parameters (Rat Tail)***	
Passive parameters		**Contractile parameters**		***Unloaded***	
$b\ (Pa)$	66.16	$T_{act}(Pa)$	10.9	*Diameter*(μm)	220
$b_1^1\ (Pa)$	199.0	$T_{phasic/}T_{ton}$	0.4	*Thickness* (μm)	7.85
$b_1^2\ (Pa)$	0.14624	λ_m	1.4575	*Length* (cm)	0.33
$b_2^1\ (Pa)$	0.000011	λ_0	0.6641	**Valve parameters (Rat Mesentery)**	
$b_2^2\ (Pa)$	0.48137			$R_{vn}\ (Pa/ml)$	60
$b_3^2\ (Pa)$	189.9			$R_{vx}\ (Pa/ml * cm^2)$	12e+10
$b_3^1\ (Pa)$	0.46244			s_o	0.01
$\alpha^1(degree$	90			Δp_o	0
$\alpha^2(degree$	0			**Flow parameter**	
$\alpha^3(degree$	27.7			*Viscosity (cP)*	0.01
$\alpha^4(degree$	-27.7				
λ_z	1.1				

Table 4. 2 Values of maximum active tension and associated geometrical properties of lymphangions for various organs in various species The active tension has been quantified using the wire myograph technique in which biaxial mechanical testing has been used.

Species and Organ	**Mean Diameter (*μm*)**	**Mean thickness (*μm*)**	**Maximum Active Tension (*mN/mm*)**
Human Thoracic Duct	2210	-	6.24±0.75
Rat Thoracic Duct	404.5±10.1	10.8±0.9	0.59±0.03
Rat Thoracic Duct	259.7±53.0	-	0.128±0.011
Rat Thoracic Duct	480±21.8	32.2±1.6	0.52±0.14*
Rat Cervical	236.0±19.5	8.10±0.6	0.37±0.03
Rat Femoral	203.0±10.7	7.8±0.5	0.39±0.03
Rat Mesentery	149.±14.1	6±0.7	0.34±0.02
Rat Mesentery	105.9±0.00	-	0.380±0.02

the geometry of lymphatic vessels were directly obtained from tail while the measurements for biomechanical properties of lymphatic vessel and lymphatic valves were obtained from thoracic duct and mesenteric lymphatic vessels, respectively (please see Table 4.1 and 4.2). Collagen distribution in rat tail lymphatics were qualitatively similar to that of the rat

thoracic duct, the active and passive parameters were obtained from previously experimentally quantified parameters. All those parameters are listed in Table 4.1. The model material properties that were used, specifically the passive parameters associated with collagen and elastin organization in lymph vessels and active parameters associated with the lymphatic smooth muscle cells, were selected within the range of what has been quantified previously through biaxial testing of rat thoracic duct and are summarized in

Integrative Modeling

To obtain the flow rate generated by intrinsic contractions of lymphangions, an algorithm in Matlab 2010 was used to simultaneously solve constitutive equations of lymphangion's wall mechanics, lymph flow as well as intraluminal valve models. This algorithm has been previously discussed in detail [71]. In brief, lymphangion constitutive equations of wall mechanics are composed of both passive model, which accounts for structure-function relationship of lymphatic vessel's wall, and an active model, which constitute a framework to model active force generation of lymphatic smooth muscle cells that incorporates both tonic constrictions and phasic contractions. Both active and passive model parameters were informed by ex-vivo isolated lymphatic vessel experiments in rat thoracic duct (see Table 4.1). A parameter (T_{act}) that dictates the contraction and relaxation of lymphatic smooth muscle cells is prescribed to stimulate the phasic contractions and tonic contractility of smooth muscle cells. The contractile activity of a lymphangion is regulated by both mechanical stimuli (e.g. stretch response) and biochemical stimuli (e.g. calcium dose-response). The stretch-dependency of the lymphatic contraction model accounts for length-tension relationship of the muscle, while cyclic changes in amplitude of active tension (Tact) prescribes the time-dependent response. The parameter T_{act} can

oscillate between basal (diastolic) and maximum (systolic) values that ultimately determine systolic and diastolic diameters respectively. It should also be noted that the parameter T_{act} only determines the maximum amplitude of active-stress (regardless of stretch-response) at each time point of contraction. When comparing the model to in vivo data, the parameter T_{act} was changed to find the best fit to experimental measurements. For the purposes of this study T_{act} was assumed to be constant along the length of the chain. In addition, parameters associated with the valve and flow models were adopted from previous studies (see Table 4.1). The solving algorithm is based on an optimization routine to find diameter and pressure that satisfy mass conservation for each lymphangion (see Fig. 3.7.).

Since the computational model was used to recapitulate the in-vivo lymphatic pressure-length relationship of a rat tail model, the geometrical parameters were measured from tail (see Table 4.1). To determine the number of lymphangions in the tail, the skin was removed from the tail region and upon application of trypan blue dye (0.4%) to identify lymphatic vessels, a long chain of lymphangions was observed. Based on the measurement of the distance between two lymphatic valves under a streomicroscope (Zeiss SteREO Lumar.V12) using segments of a lymphangion chain at three different locations (4, 8, and 12 cm from tip of tail), the average lymphangion number was approximated to be 3 lymphangions/per centimeter in the rat tail. Since occlusion pressures were measured at three locations from the tip of tail (4 cm, 8 cm, and12 cm), three locations along the tail were modeled as chains with 12, 24, and 36 lymphangions based on the average number of lymphangions per centimeter of tail (3 lymphangion/per cm), respectively. The pressure at inlet of chain was set to 6mm Hg (an approximate pressure at the injection site near the tip of tail), which was based on an approximation of the y-intercept of a curve fitting the

experimental data where the number of lymphangions is mathematically zero. The outflow pressure was elevated until the flow rate dropped below 0.01 mL/min (equivalent to pressure applied through pressure cuff to occlude lymphatic flow).

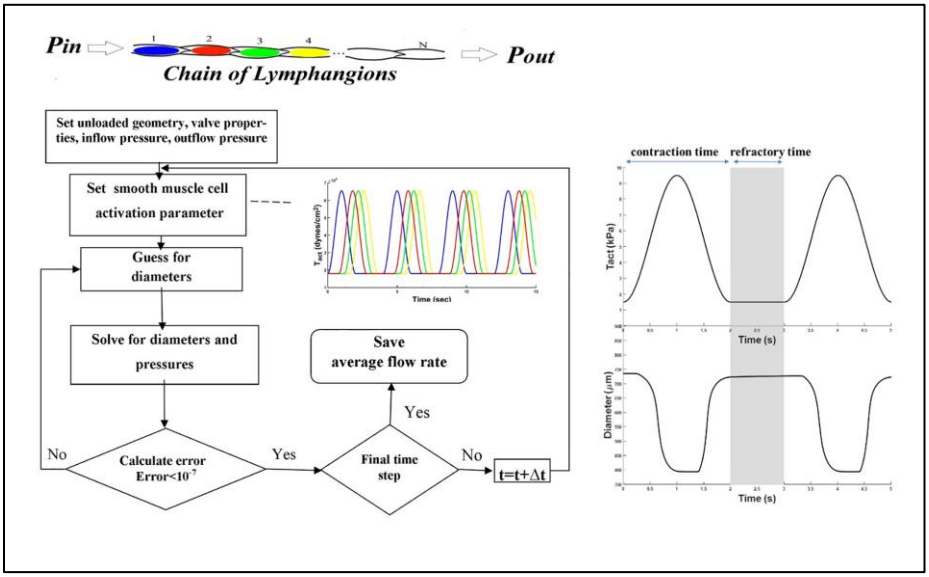

Figure 4. 3 The schematic of the solving routine for computational framework used to model a chain of lymphangions in a series arrangement.

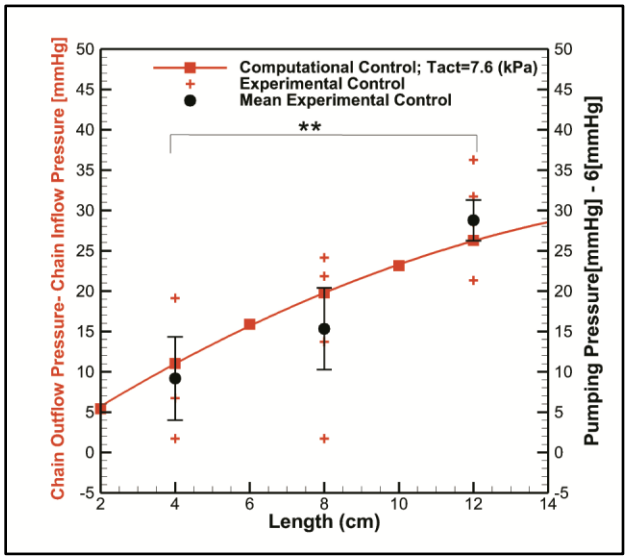

Figure 4. 4 The maximum outflow pressure at which flow can be achieved as a function of chain length using in vivo NIR measurements and computational modeling. The activation parameter (Tact) which is associated with the degree of smooth muscle cell activation is the sum of phasic and tonic activation parameters (see Eqs. (7)) and was iteratively solved for to provide the best fit for the experimental data. SEM along with the mean at 4cm (n=3), 8cm(n=4), and 12 cm(n=5)

distance from the tip of tail were plotted. Statistical significance was determined through a Kruskal-Wallis with a post-hoc Dunn's test for multiple comparisons (p-value<0.05).

4.1.3 Results

Experimental and computational modeling results show that pumping pressure increases with chain length. The effective pumping pressure in the rat tail progressively increases along the length of the tail as one moves from the tip of the tail towards the base (Figure 4.4). Specifically, the average pumping pressure for each group of rats was (15.2 +/- 5.17) mmHg (*n=3*), (21.3 +/- 5.06) mmHg (*n=4*), and (34.8 +/- 2.52) mmHg (*n=5*) and distances of 4 cm, 8 cm, and 12 cm from the tip of the tail respectively ($p < 0.05$). As the measurement site from the tip of tail increases the maximum occlusion pressure at which flow can be achieved increases. This phenomenon is also observed in the computational model where optimization of the activation parameter to provide the best fit to the data suggests a value of $T_{act}=7.64$ (kPa), which can be converted into a tension by multiplying by the vessel thickness to yield a value of 0.06 mN/mm. This is within the range but smaller than tension values reported in the literature for isolated rat lymphatics from other tissue beds (Table 4.1). The Pearson correlation coefficient between mean experimental data and computational data is $r=0.914$.

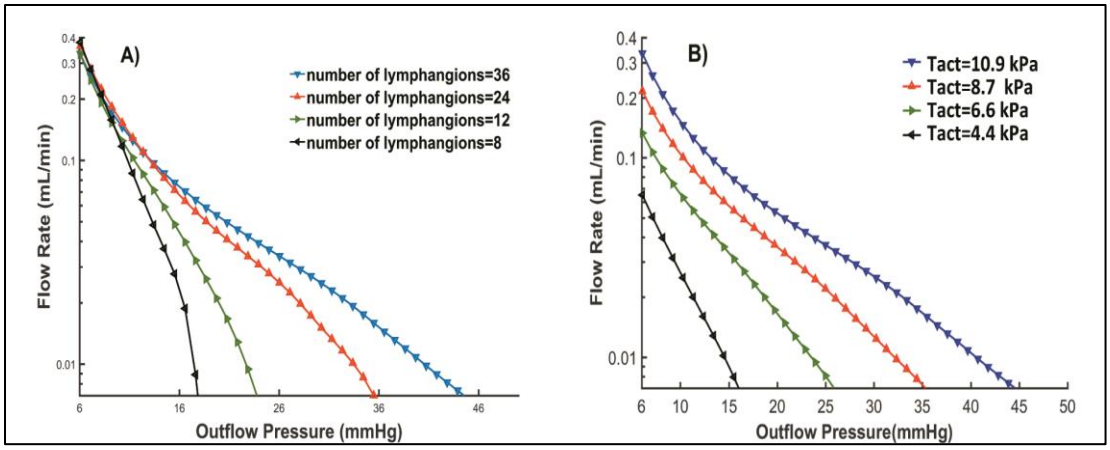

Figure 4. 5 Flow rate as a function of outflow pressure in the lymphangion chains: A) for different number of lymphangions in a chain with an activation parameter of Tact=10.9 (kPa) B) for different values of the activation parameter of smooth muscle cells in a chain with 36 lymphangions.

Parametric studies: Contractility strength and number of lymphangions modulate pumping pressure and flow rate. To explore further how the number of lymphangion in a chain and the stimulation of smooth muscle cells might influence this observed pressure-length relationship, we utilized the computational model to plot the relationship between flow rate and outflow pressure for a lymphangion chain with different numbers of lymphangions and varying activation parameters (Figure 4.5). As the number of working lymphangions within a chain increases (while holding T_{act}=10.9 kPa) a non-zero flow rate can be achieved at higher opposing pressure gradients (Fig. 4.5A). Additionally, an increase in contractile strength via a larger activation parameter in a chain with 36 lymphangions results in sustaining flow at a higher confronting pressure gradient (Fig. 4.5B). Ultimately when there are many lymphangions in series there appears to be a nonlinear relationship between occlusion pressure and the number of lymphangions in a chain (e.g., for a chain with 36 lymphangions and Tact=8.7 kPa, the empirical fit of occlusion pressure = $-0.0089n^2 + 1.0431n$ provides a better fit than a linear one (R^2 = 0.9986)). At a lower lymphangion number the relationship appears to be reasonably

approximated by a linear fit (e.g., for a chain with 6 lymphangions and Tact=8.7 kPa, R^2 = 0.9609) that is dependent upon the contractility of the smooth muscle cells (Figure 4.4). This implies that the lymphangion chain with higher degree of smooth muscle cell activation is more capable to overcome higher pressure along the chain and that each lymphangion contributes to build up a pressure gradient to propel flow against an adverse pressure gradient.

The theoretical maximum flow that can be achieved under the pressure scenarios modeled here occurs when no adverse pressure gradient is present (i.e. the outlet pressure of the chain equals the inlet pressure). While increased smooth muscle cell activity increases the maximum flow rate that can be achieved through the network, the total number of lymphangions within the chain has very little effect on maximizing flow in the absence of an adverse pressure gradient (Figure 4.6). Stated another way, increasing the number of lymphangions within a given length of vessel would enhance that vessels ability to overcome adverse pressure gradients, but would not have a substantial benefit for enhancing lymphatic flow.

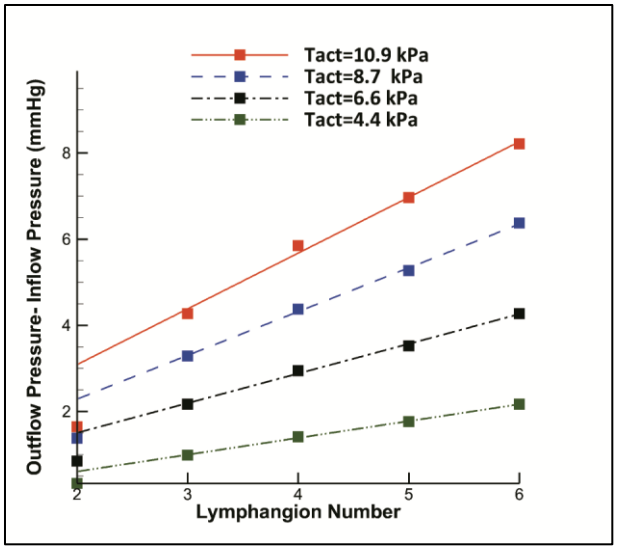

Figure 4. 6 Muscle activation (Tact) and the number of lymphangions in a chain, both serve to increase the maximum pressure generation capacity of a lymphatic chain. Tact and lymphangion number are both varied over ranges that have been measured in vivo. Tact=10.9 kPa (y =1.3733x ; R^2 = 0.947); Tact=8.7 kPa (y = 1.0526x;R^2 = 0.9609); Tact=6.6 kPa (y = 0.7026x; R^2 = 0.9517) ; Tact=4.4 kPa (y = 0.3619x; R^2 = 0.908), where x and y denotes outflow pressure – inflow pressure and lymphangion number respectively.

Parametric studies: Contractile frequency has little effect on maximum pumping pressure. Many in vivo studies that utilize NIR imaging rely primarily on lymphatic contractile frequency as a measure of lymphatic function, yet it is unclear how exactly contractile frequency changes lymph flow in different physiologic scenarios. To investigate the effect of lymphatic contractile frequency on both flow rate and maximal pumping pressure, the computational model was used to vary the refractory period between contractions (Figure 4.8). A contraction cycle is composed of a contraction time (rhythmic contraction) as well as a refractory time (time at which the diastolic diameter is held constant). Thus, the frequency of contraction is the reciprocal of the sum of these two contraction times. Under a minimal adverse pressure gradient, increased contraction

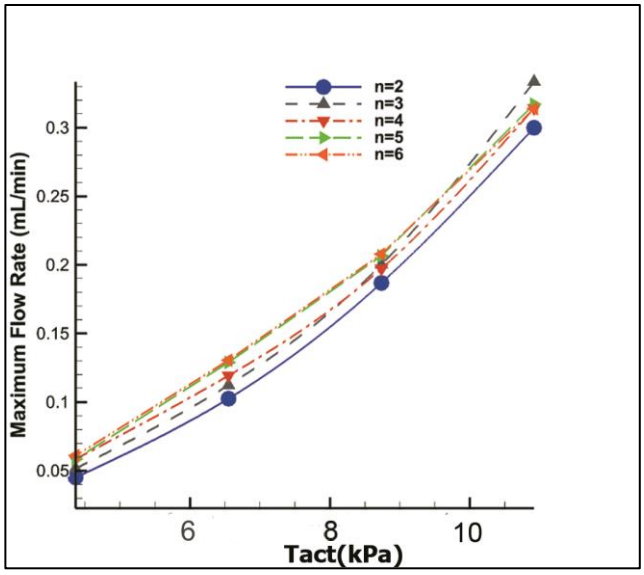

Figure 4. 7 Maximum flow rate that can be achieved, when there is no adverse pressure gradient present, due to the intrinsic contraction of lymphangions with a different number of lymphangions in the chain as a function of lymphatic smooth muscle activation (Tact).

frequency (i.e. decreased refractory time) enhances lymphatic flow, unless there is an adverse pressure gradient. However, in the presence of an adverse pressure gradient, the benefit of increased pumping frequency is diminished. Increased contraction frequency increases lymphatic pumping pressure for frequency ranges less than 10 cpm, however, the benefit of contraction frequency to pumping pressure is diminished at values larger than this (Fig. 4.9). Interestingly, when compared to in vivo data there is no correlation between the contraction frequency of a lymphatic pre-occlusion and the resulting pumping pressure. However, it should be noted that the current experimental set-up does not allow one to track packet frequency distal to the occlusion while pumping pressure measurements are

being made, making it unclear whether this frequency - pressure generation relationship occurs in vivo.

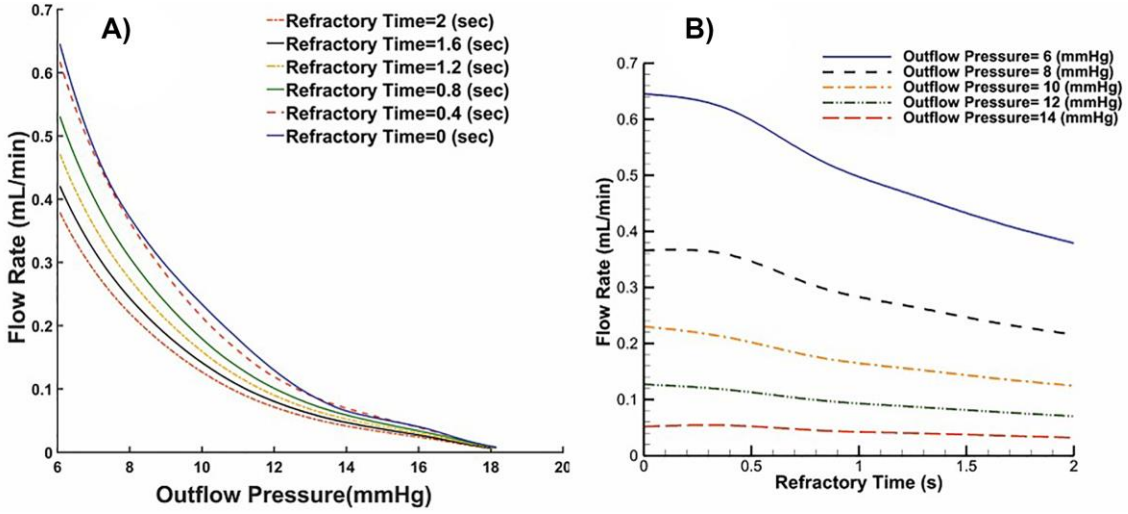

Figure 4. 8 The effect of refractory time on A) flow rate and maximum pressure in a chain of 8 lymphangions, B) flow rate generated by intrinsic contraction of lymphangions for chains exposed to different opposing outflow pressures.

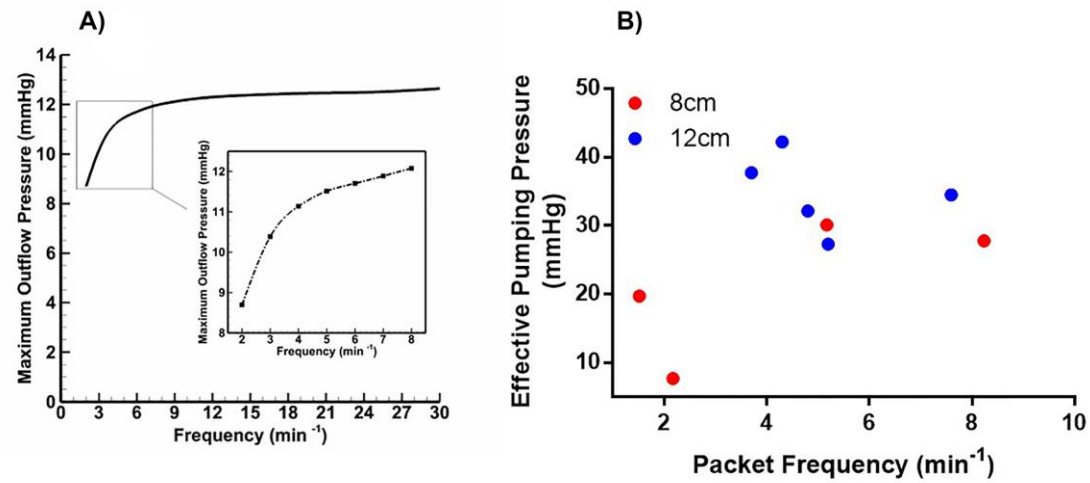

Figure 4. 9 The effect of frequency on maximum pressure that can be overcome by a lymphangion chain to maintain flow rate. A) computational results for a chain of 8 lymphangions, T_{act}=10.9 *(kPa)*. B) experimental results from the rat tail model demonstrate that there is no correlation between the baseline packet frequency and the effective pumping pressure.

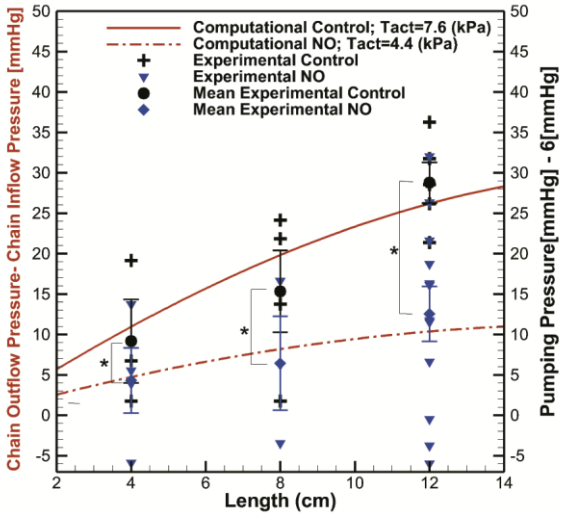

Figure 4. 10 The effect of dermal nitric oxide delivery on the relationship between maximum outflow pressure and length from the tip tail using in vivo NIR pumping pressure measurements and the computational model. The activation parameter which is associated with the degree of smooth muscle cell activation that best fits the in vivo NO experiments was found to be Tact=4.4 (*kPa)*. SEM along with the mean at 4cm (n=4), 8cm(n=3), and 12 cm(n=12) distance from the tip of tail were plotted. Significant difference between the control and GTNO data sets was determined using the extra sum of squares F-test on the quadratic best-fit regressions of the data (p-value<0.05).

Experimental and computational modeling results concur that dermal nitric oxide donor diminishes maximum pumping pressure. Given the model's prediction that the maximum outflow pressure is highly dependent on lymphatic muscle activity, we sought a method to experimentally alter T_{act} in vivo by treating the tails of rats with a dermal cream (GTNO) containing a nitric oxide donor.

The average pumping pressure for each group of rats was found to be (10.3+/-4.02) mmHg (n=4), (12.43+/- 5.80) mmHg (n=3), (18.54+/-3.4) mmHg (n=12), and distances of 4cm, 8cm, and 12 cm from the tip of the tail, respectively. Comparing to control and GTNO data sets using the extra sum of squares F-test on the quadratic best-fit regressions of the data revealed that the two groups are statistically different. This relies on the fact that

application of NO resulted in the attenuation of the pumping pressure that was more pronounced as one increases the number of lymphangions in the chain. Thus, treatment of the lymphatic chain with dermal NO compromises its capability to maintain flow rate in the presence of a confronting pressure. Using the computational framework, decreasing contractile strength via a reduction of the activation parameter by approximately 40% (from 76.4 to 43.7) can capture these experimental observations (Fig. 4.10).

4.1.4 Discussion

While significant advances have been made towards understanding the molecular regulation of lymphatic contractility both in isolated vessels and in small animal models, there remains a significant gap in our understanding of how networks of lymphangions work across long distances to move fluid against the unfavorable pressure gradient that exists in vivo. Recent advances by several groups have demonstrated the ability to measure lymphatic pumping pressure in both clinical and animal research settings. Similar to blood pressure, which provides a measurement of cardiac pump function, the technique has been suggested to be indicative of the combined capacity of the intrinsic and extrinsic lymphatic pumps. However, unlike the cardiovascular system, in the lymphatic system the vessels themselves are the primary source of pressure generation and vascular resistance. This would suggest that any measurement of lymphatic pumping pressure will be highly sensitive to the number of lymphangions that are contributing to pressure generation and thus the location on the appendage that the measurement is made. By combining computational modeling built on experimental measurements of lymphatic vessel mechanical properties, with in vivo measurements of lymphatic pumping pressure along various locations in the rat tail, we show that pumping pressure changes over the length of

the vessel and that this change in pumping pressure depends on both the number of lymphangions engaged in pumping and the contractile force of the muscle generating the contractions. In the rat tail model, this allows one to record a direct measurement of the intrinsic pump, although it remains to be seen if the intrinsic pumping capacity can be decoupled from the extrinsic pump (e.g. skeletal muscle contraction in a human arm) where extrinsic contractility is thought to significantly contribute to the transport capacity.

In addition to enabling the in vivo measurements of lymphatic muscle contractility, the computational model also allows for the investigation of how various parameters affect the maximum outflow pressure that can be achieved for a given lymphangion chain. This is important since the lymphatic system is typically exposed to hydrostatic pressure gradients that oppose flow from the interstitial space to the venous system, and thus lymphatic smooth muscle cells must impart energy to propel flow through the network. Although intrinsic pump activity enables lymphatic vessels to pump over a larger range of transmural or outflow pressures, the further elevation of outlet pressure outside of this range induces pump incompetency. The simulations show that flow rate declines with an increase in maximal outflow pressure as exposing a lymphangion chain to higher outflow pressure results in the progressive inability of lymphangions to empty, an observation that is consistent with isolated vessel experiments is also in agreement with other computational models of lymphangion chains. The simulation results suggest that both the degree of smooth muscle cell activation and the number of working lymphangions directly influence this relationship between flow and outflow pressure. In the context of lymphedema, it has been suggested that patients with a higher lymph load are predisposed to disease, motivating the need for further studies that explore how prolonged elevated demand on the

intrinsic lymphatic pump might drive fatigue of lymphatic muscle force generation and thus lymphedema. While, smooth muscle force generation of lymphatics likely exhibit regional and species variations, the values for the model that best fit the in vivo data are within the range of those measured experimentally from other tissues tested ex vivo (Table 3.3).

Frequency of lymphatic pumping has become a very common measurement that is suggested to be indicative of lymphatic function. However, if the ultimate function of lymphatics is to generate flow, contraction frequency by itself may not always accurately reflect function. This has been suggested by both in vivo experiments, where flow can be observed in certain situations even when the vessel is not contracting and in isolated vessel experiments in which imposed flow actually serves to inhibit lymphatic contraction and conserve energy [179]. This is also evident through the in vivo experiments reported here, where the baseline contraction frequency of an animal does not necessarily reflect the maximum pressure generation capacity of the lymphangion chain (Fig. 11). The computational model suggests that the benefit of contraction frequency to pressure generation by a lymphangion chain plateaus at values above 10 cpm. These results raise doubt as to whether focusing on contractile frequency as the primary metric of lymphatic dysfunction is a clinically relevant endeavor for explaining lymphatic failure in lymphedema.

It is important to note that isolated vessel studies have demonstrated that contraction frequency increases under an elevated outflow pressure [121]. This pressure dependence on the contractile frequency is not incorporated into the current model and would be a valuable feature to include in future iterations. However the model and the in

vivo data still support the idea that the generated pressure gradient along a chain confronted with a high adverse pressure is mainly due to the contractile strength of lymphatic smooth muscle cells and the number of lymphangions present. While T_{act} contains both the effects of tonic constriction and phasic contractions, the current study assumes that the ratio between these two is constant and thus cannot decouple the independent effects of the two. Although we include intraluminal valve function through modeling variable resistance to lymph flow from opening to closure as a function of transaxial pressure gradient along the valve, there is a known dependency of the valve resistance behavior on the transmural pressure (or circumferential stretch) [118], which is neglected in this model. Including this feature in future iterations of the model would likely further enhance the benefit of Tact on enhancing the effective pumping pressure, as the elevated myogenic constriction under a large transmural pressure would improve valve function.

This study has several limitations that should be noted. First, although the microstructure-based model captures many of the salient features of pumping function in a lymphangion chain, the comprehensive experimental quantification and validation of model parameters in the specific anatomical region of interest are still needed. There is experimental evidence that lymphatic vessels from different regions have adapted their contractile force in line with the particular in vivo pressure experienced by the lymphatic vessel [122,180]. An example in rat is the femoral lymphatic vessel which shows the highest capability to adapt its contractile force to withstand high pressure, while thoracic duct exhibits the lowest capacity to overcome elevated pressure [122]. In contrast, the thoracic duct is known to be very sensitive to wall shear stress and thereby is able to switch between pump and conduit modes. The ideal computational approach requires

experimental measurements of valve resistance and biomechanical material properties across a chain of vessels within the tail, as it is unknown how these parameters vary along the length of a chain of lymphangions. Additionally, the extent that the surrounding matrix provides structural support and the mechanical properties of said matrix vary from one tissue bed to another, could be salient features to include in the model. This is particularly important in the context of lymphedema where fibrosis of the interstitium is known to alter the surrounding matrix. In the absence of such information, we have invoked experimentally derived parameters form other lymphatic tissue beds including a valve-model which has been validated previously in rat mesenteric lymphatic vessels and passive biomechanical properties quantified in rat thoracic duct. In addition, the heterogeneity of biomechanical properties, as well as the complex topology of the lymphatic network (e.g., branches in region near tip of tail), are neglected in this study. Thus, the direct measurement of model properties along with a better understanding of network properties in the lymphatic vasculature to validate intraspecific (e.g, tail, mesentery, thoracic duct, limb and popliteal vessels) and interspecific (e.g, rat, sheep and human) pressure-length relationships remains an area for future studies.

Lastly, it is difficult to narrow down the specific mechanism by which NO is decreasing lymphatic pumping pressure. Previous studies in isolated vessels have shown that excess nitric oxide lowers both the frequency of contraction, vessel tone, and contraction amplitude [121,181]. In vivo studies involving fluorescent tracers have shown that NO decreases frequency of contractile events and/or tracer clearance rate [173,182–184]. However, NO is also known to alter microvascular permeability [185], and thus it is difficult with in-vivo experiments to pin down the exact mechanism by which NO is

altering function. Our computational model and experimental results show that the reduction in effective pumping pressure is likely not primarily due to its effects on contraction frequency or interstitial fluid pressure, but rather be captured by its influence on Tact. However, since T_{act} includes both the combined effects of tonic constrictions and phasic contractions, it is not clear in this study whether NO effects on tone (and indirectly valve function) or contraction amplitude are primarily responsible.

In summary, through computational modeling and a novel implementation of lymphatic pumping pressure measurements using NIR imaging, we show that the maximum outflow pressure that a lymphangion chain can overcome is a function of the number of lymphangions in the chain and the active tension generation by the lymphatic muscle cells. By fitting our computational model to experimental measurements of the pumping pressure at multiple locations along the tail, we can estimate the average force generation for the chain of lymphatics, decoupling the intrinsic function of that vessel from other extrinsic factors such as interstitial fluid pressure at the injection site. Although measurement of the maximum pumping pressure is known to have the potential as a clinical diagnostic approach for lymphedema [186,187], this study suggests that any measurement of the maximum pumping pressure should be interpreted in the context of chain length; and hence, measurements should be performed at multiple locations to provide sufficient information on lymphatic muscle activity in the limb of interest. Since this approach is non-invasive, the potential as a clinical diagnostic in lymphatic health is promising and future trials in humans are warranted to establish feasibility. The ability to obtain a direct measurement of lymphatic muscle health in a clinically relevant scenario remains lacking, and would be a substantial benefit to future diagnostic capabilities.

CHAPTER 5. LYMPHATIC REMODELING IN RESPONSE TO INJURY

5.1 Aim 3:

In this chapter, I test and show the feasibility of developing a microsurgical ligation model in the rat tail to study the prolonged adaptations of collecting lymphatic vessels to mechanical overloads. There is one milestone for Aim 3 as follows:

Milestone: Developing a novel lymphatic injury model in the rat tail and testing the feasibility of using this animal model to study load-induced remodeling in collecting lymphatic vessels via in-vivo imaging and ex-vivo experiments on the isolated vessels.

Hypothesis I: I test whether the surgical removal of relatively large segments of lymphatic vessels from one side of the tail triggers a remodeling response resulting in a progressive decline in lymphatic function.

5.2 Introduction

The lymphatic system is found in almost all soft tissues and plays a fundamental role in maintaining tissue's fluid balance, immune function and absorption and transport of lipids [1]. The lymphatic system has a hierarchical architecture that enables lymph transport from the interstitial space through specialized lymphatic capillaries and ultimately larger collecting ducts that returns lymph back to the great veins [2]. Contractile units of the lymphatic system called lymphangions have been equipped with specialized muscle cells that enable the vessels to spontaneously contract to propel lymph against the gravity and

an adverse pressure gradient from the interstitial space to the venous system. Since the long chain of contracting lymphangions need to be orchestrated to efficiently transport lymph, lymphatic vessels are tightly regulated by biochemical (e.g., vasoactive agents such as NO, histamine, etc), mechanical (e.g., stretch due to pressure) [3–6,10,15–17].

Not surprisingly, impaired lymphatic pumping has been implicated in debilitating diseases such as lymphedema where the stagnation of lymph drives tissue swelling, chronic inflammation, fibrosis, and infections. It has been suggested the damage to the lymphatic system during modalities of cancer treatments induce microstructural remodeling in collecting lymphatic vessels [188]. In particular, morphological changes in different stages of lymphedema development suggest that the lymphatic dysfunction may be a result of a gradual remodeling that might occurs months to years prior to the onset and progression of lymphedema [189]. This idea is support by the incident rate of lymphedema and variability in the disease onset. Typically, the incidence of lymphedema increases with time and most patients develop lymphedema months to years post lymph-node dissection. Although minor swelling after the initial surgery resolves spontaneously, the persistent swelling recurs in lymphedema patients 8-24 post-surgery [190]. Generally, it is hypothesized a gradual remodeling response in the lymphatic system and abnormal development of lymphatic contralateral lymphatic are the major drivers of lymphedema progression [191].

Mouse models of lymphedema have provided valuable information regarding lymphatic growth and remodeling (G&R) post-lymphatic injuries [54,177]. In the typical mouse tail lymphedema model, all initial and collecting lymphatic vessels are cauterized around the tail circumference to occlude pathways of lymph transport [192].

Currently, there is the scarcity of small animal models available to mimic human lymphatic dissection where relatively large segments of lymphatic vessels are removed while most initial lymphatics remain functional except at the incision site. There are both single and double ligation models to induce lymphedema via the surgical model of lymphatic injury [54,193]. One challenge with the mouse model is the small size of mouse tail lymphatic vessels, which makes the isolation of these vessels difficult. To tackle this challenge, we develop a novel rat tail model of lymphatic injury where relatively large segments of collecting lymphatic vessels are ligated via a small incision to the skin and microsurgical ligation of collecting vessels while contralateral in the opposite side of the tail is being kept intact. The size of the rat tail is an advantage that makes it possible to study morphology and material properties of isolated vessels post-surgery. The collecting lymphatic vessels exposed to prolonged pressure/flow overloads respond to negative feedback of the lymphatic muscle cell's (MCs) hypertrophy/hyperplasia, ECM remodeling, and altered contractility that ultimately leads to the gradual attenuation of lymphatic pumping.

5.3 Methods

Animal model and surgical procedure. Sprague Dawley (SD) male rats (Charles River, Wilmington, MA, 280-350 gr) were used in this study. Rats were anesthetized using ketamine (40mg/kg), DEXDOMITOR® (dexmedetomidine hydrochloride) (0.13.mg/kg). Once the animal reached a surgical plane of anesthesia, an incision (~1 cm) was made in one side (left side) near the base of tail to gain access to the lateral tail vein. Trypan Blue Solution 0.4% dye was injected downstream of the incision site to enhance the visibility of lymphatic vessels. Upon identifying two chains of the rat tail lymphatic vessel (size~ 250µm-350µm) under a dissecting microscope, two large segments of the collecting

lymphatic vessels (~1-2 cm) were surgically ligated using the microsurgical scissors (Fine Science Tools, Inc). The incision site was sutured using Suture 4-0 Silk Black (ETHICON SUTURE, Inc). Once the procedure is completed, ANTISEDAN (1.3 mg/kg) was injected for the reversal of the sedative and analgesic effects of DEXDOMITOR®. To perform the isolated vessel experiments post-surgery, we use a similar approach where the dissected vessels were placed in Dulbecco's Phosphate Buffered Saline (DPBS, Corning). Once the surrounding fat and connective tissues were removed, the lymphatic vessels (containing approximately ~2-3 cm and containing 1-2 valves) were mounted on opposing cannula in a custom-made vessel chamber [75]. All the protocols were approved by Georgia Tech's Institutional Animal Care and Use Committee (IACUC).

Near-infrared imaging and metrics. We utilized a previously developed lymphatic near-infrared (NIR) imaging system to quantify functional lymphatic transport in-vivo. This system uses a shutter Instruments Lambda LS Xenon arc lamp, an Olympus MVX-ZB10 microscope, a 769 nm bandpass excitation filter (49 nm full-width half maximum, FWHM), an 832 nm bandpass emission filter (45 nm FWHM), and an 801.5 nm longpass dichroic mirror [54]. A volume of 20 μL of a NIR fluorophore 475 IRDye 800 CW NHS Ester (929-70020, LI-COR Biotechnology, Lincoln, NE) bound to 40kDa 476 methoxypolyethylene glycol (mPEG) (JenKem Technology USA, Plano, TX) was injected into the tip of rat tail. This volume was chosen based on the previous experiments and tail experiments to provide sufficient dye volume to image the collecting lymphatic vessels in the rat tail. A Photometrics Evolve Delta 512 EM-CCD camera was used to acquire images at a frame rate of 10 fps with a camera exposure time of 100 ms throughout experiments.

To analyze functional NIR metrics, we used previously reported metrics including packet frequency, packet amplitude, and packet transport as follows [54]:

Packet frequency: the number of peaks in the fluorescence signal per minute in vivo

Packet amplitude: the amplitude of NIR signal packet

Normalized packet amplitude: the normalized amplitude of NIR signal packet

Filling time: the time needed the dye fills vessels from baseline value to the maximum value prior to the contraction

Light Sheet Microscopy. To perform light sheet microscopy images were acquired using a Zeiss Lightsheet Z.1 microscope equipped with dual PCO.Edge sCMOS cameras and dual side illumination with pivot for multiview acquisition that allows high-resolution imaging of samples with minimal photobleaching. Two laser line of 488nm (50mW) and 638nm (75mW) were used for acquisition in the combination of 5X/ 0.16 N. A. with 5X 0.1 N.A. illumination objectives. Vessels were filled with 1% Agarose, low gelling temperature, Type VII-A, (Sigma-Aldrich #A0701) in temperature of 38 ^{0}C prior to imaging. After agarose has polymerized in room temperature, vessel was with 1% agarose and mounted on the glass capillaries (BRAND 701904 volume 20 µL) using the plunger (Brand #701932) for suction. Capillary was mounted in microscope holder and specimen chamber filled with diH2O. After the gel has polymerized the plunger was used to push out the specimen.

Thickness Measurement. Light sheet images were analyzed using Image J software to calculate average thickness based on the thickness at different sections along the vessel length (6 sections).

Immunostaining. The protocols are the same as the previous protocols presented in Chapter 2 (section 2.1.2.7).

Biaxial testing system. We used our previously developed and improved biaxial testing device customized to study the biomechanics of lymphatic vessels [81]. A custom-written program in LabVIEW was used to control transmural pressure via a syringe pump movement (Harvard) and the precise pressure sensors (1psi SSC series, Honeywell). Linear actuators and XYZ stages (Newport Precision, LTA series and M-461 series) were used to control the axial stretch. Axial forces were measured using a 50mN force transducer (Aurora Scientific, Model 400A). Using an inverted microscope and a custom-made chamber. Using the LabVIEW program, the diameter of the vessel, obtained from an inverted microscope (2.5x magnification) and digital camera (Allied Vision Technologies, Marlin F-033B) capturing at 18 fps tracing, was recorded in real-time and saved to the hard drive for further analysis. For the passive biaxial testing, Ca^{2+}-free PBS solution (Corning® Phosphate-Buffered Saline, 1X without calcium and magnesium, PH 7.4 ± 0.1) containing 3mM EDTA [70,159] was used to inhibit vessel contractility. All vessels were preconditioned by ramping the transmural pressure from 0 to 10 mmHg while at three stretch steps of 10%, 20%, and 30%. Those values were chosen based on our previous study to quantify the biaxial properties of rat tail lymphatics.

Statistics. To determine the statistical significance between injured and contralateral and sham groups, a one-way ANOVA in conjunction with Dunnett's post hoc test was used to make multiple comparisons. The statistical analyses were performed using Prism 5 (GraphPad Software) with significance set at $p < 0.05$. All results were reported as means (±SEM).

5.4 Results

Surgical ligation of lymphatic vessels in the rat tail mimics lymphatic injury in clinical settings. Most surgical interventions that result in lymphatic dysfunction such as lymph node dissection involve lymphatic injury. To investigate how collecting lymphatic vessels respond to surgical injury, large segments of lymphatic vessels from one side of the tail were ablated to disrupt transport while contralateral vessels on the opposite side of the tail were kept intact. All animals were monitored to have properly ablated lymphatic vessels and the incision site was sutured at the end of the procedure. Since the surgical procedure was minor, the animals undergoing the procedure shows a very high survival rate (99%>) with minimum symptoms post-surgery. It remains possible that in some cases the ligation procedures cause acute inflammation rendering vessel harvesting challenging. To address this concern, the procedure was only limited to animals with properly ligated lymphatic vessels and excluded animals in which blood vessels were accidentally ligated (Fig. 5.1).

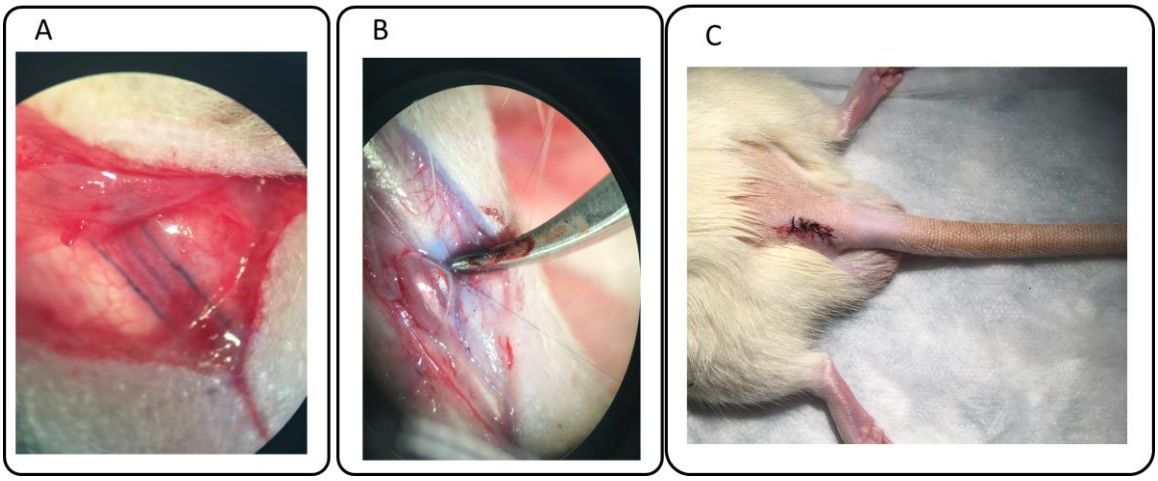

Figure 5.1 A representation of surgical procedure. (A) Lymphatic vessels were visualized via injection of Trypan blue dye (B) Large segments of lymphatic vessels were removed (C) The skin was sutured at the end of the procedure.

A remodeling/lymphangiogenic response reroutes ligated collecting vessels to dermal initial lymphatics following lymphatic injury. Near-infrared (NIR) imaging allows the assessment of lymphatic function and regeneration *in-vivo*. Our imaging data demonstrate a remodeling response as early as two weeks post-surgery showing the generation of dermal lymphatics to bypass the injured vessel. Interestingly, NIR data suggest this remodeling response connects the injured vessels to intact contralateral vessels on the opposite side via the network of dermal lymphatics. Further, functional imaging suggests that contraction frequency of the vessel distal to injury site increases but returns to the baseline value four week post-surgery (Fig. 5. 3 A). Average packet amplitude of injured vessels decreased postsurgery, however, the baseline value of injured vessels is larger (Figs. 5. 3 B and D).

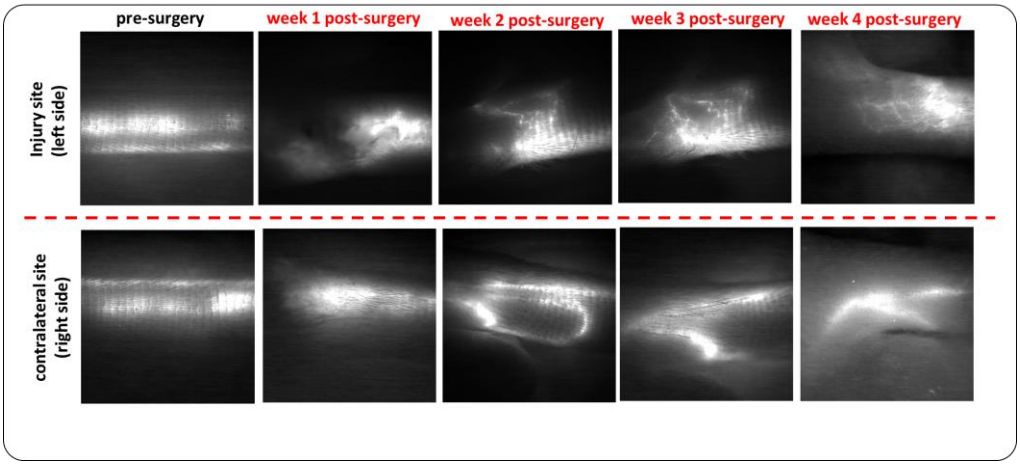

Figure 5. 1 Longitudinal NIR imaging for both injured and intact contralateral lymphatic vessels. The imaging data suggest that injured vessels reroute to the dermal lymphatic to connect to intact contralateral.

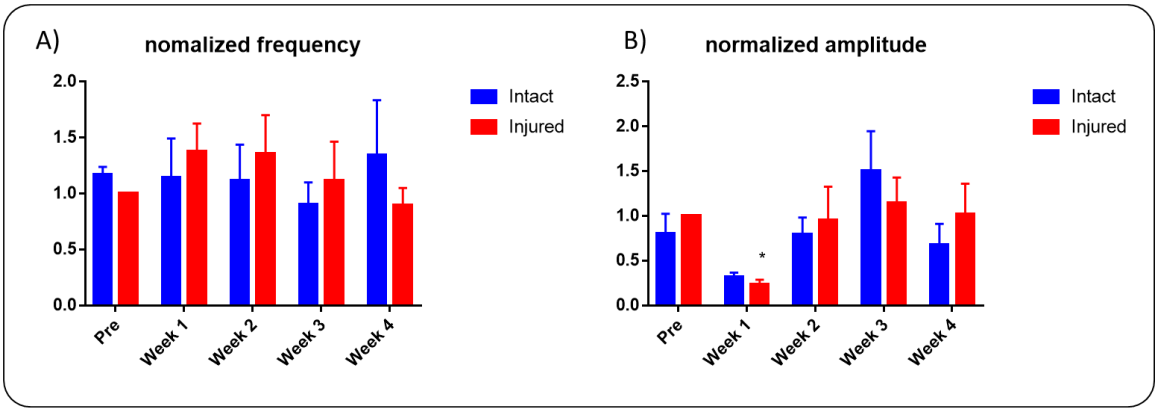

Figure 5. 2 Longitudinal functional NIR imaging for both injured and intact contralateral lymphatic vessels. A) Frequency of contractions B) Average amplitude of packets. * Indicates significance between experimental groups and presurgery group (n=6, $p<0.05$). Values were normalized with presurgery baseline.

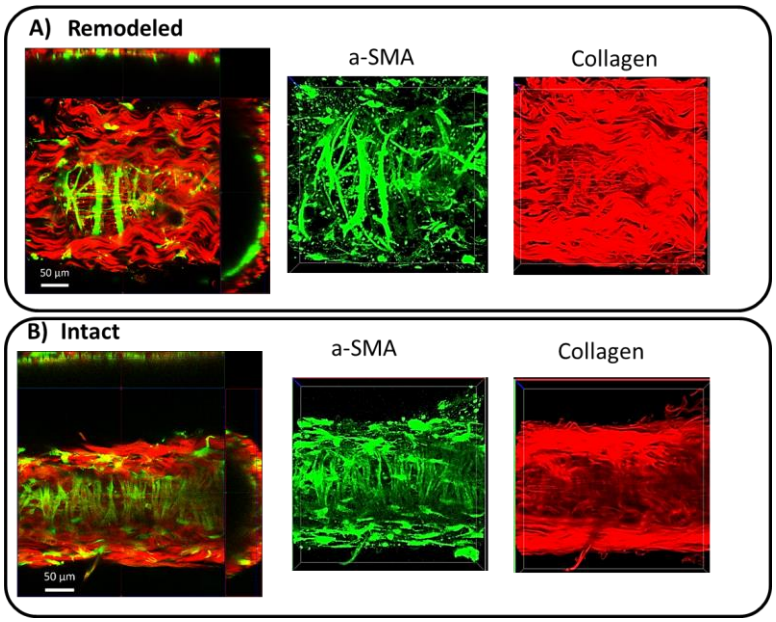

Figure 5. 3 Immunostaining of an injured and the intact contralateral lymphatic vessel from the rat tail. Vessels were stained for lymphatic smooth muscle cell and collagen and images were obtained using confocal microscopy.

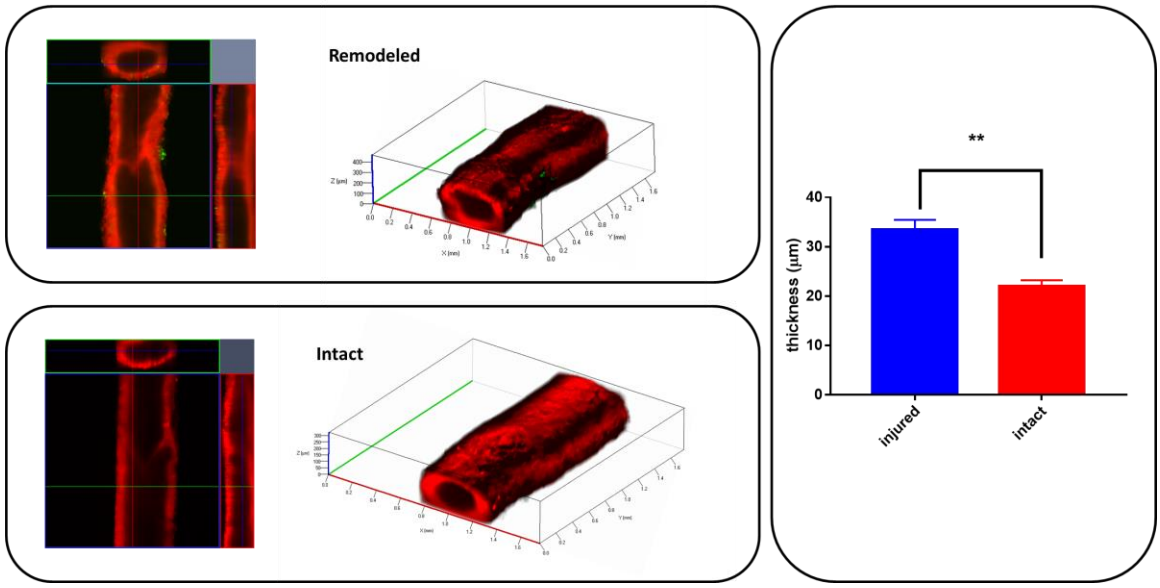

Figure 5. 4 Light-sheet microscopy of lymphatic vessels for injured and intact vessels. Vessels were stained using Alexa Fluor™ 633 Hydrazide to stain elastin and collagen. The average thickness of the injured vessel is thicker compared to the intact vessel. The thickness was obtained based on the average thickness along the length of the vessel. This measurements were performed on a single pair of lymphatic vessels from a single animal. Statistical significance was assessed using a non-parametric t-test and ** indicates $p<0.005$.

Histological assessments reveal altered lymphatic function in both ligated and intact vessels following lymphatic injury. Immunostaining for two vessels from the injured site and intact site suggests that the structure of contralateral and injured vessels are different. Staining for lymphatic muscle cells (a-SMA) suggests that the injured vessel has irregular and thicker muscle bundles compared to the intact vessel (Fig. 5.4). The experiments were performed on a single pair of lymphatic vessels from a single animal. Further, based on the light sheet microscopy for whole immunostaining of the same vessels with Alexa Fluor™ 633 Hydrazide, ligated vessel looks to be fibrotic and thicker compared to the intact vessel (Fig. 5.6). Collagen deposition is observed in the valvular region in the injured vessel while in the intact vessel less collagen is observed.

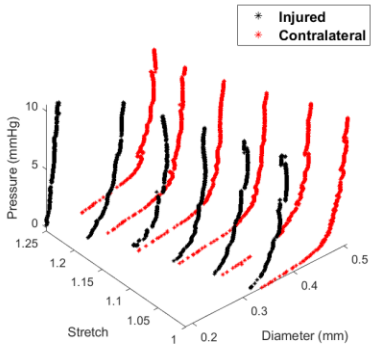

Figure 5. 5 A representation of pressure-diameter biaxial testing from injured and contralateral vessels from the rat tail.

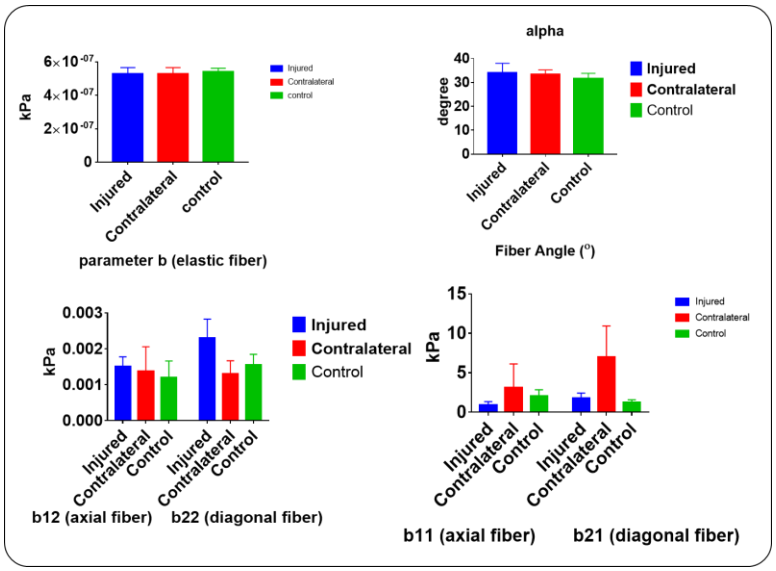

Figure 5. 6 Biomechanical properties of rat tail lymphatic vessels from injured and intact contralateral vessels using a three-fiber family model (injured n=3; intact n=3, control n=5). No statistical significance was observed between different groups.

Ex-vivo multi-axial testing reveals structural and material remodeling following lymphatic injury. To investigate the effect of overloads on the biomechanical properties of lymphatic vessels post-lymphatic injuries, biaxial testing was performed on the isolated vessels from both injured and intact contralateral vessels. The results suggest that the biomechanical properties of injured vessels are different from the intact contralateral vessels (*n=6 vessels).* As shown in Fig. 5.6 and 5.7, vessels distal to the injured site seems to be stiffer compared to the contralateral vessel on the opposite side. Fitting biomechanical properties using a three-fiber family model (Eq. (12); chapter 3) suggests that material properties of a ligated vessel and intact contralateral are different.

5.5 Discussion

Post-surgical lymphedema is a challenging disease associated with dysfunctional lymphatics and clinically manifested by tissue swelling and fibrosis in patients who have

undergone cancer therapies and surgeries [194–196]. Although our understanding of the lymphatic system has been significantly improved over the past decade, the disease etiology still remains unknown [197]. Since the clinical manifestation of the disease can be delayed months to years after the surgery, the general notion is that lymphatic remodeling might occur months to years before the disease onset [40]. Despite efforts to study lymphedema onset and progression, much remains unknown. Particularly, the mechanics of lymphatic vessels in disease is an area that remains to be investigated, despite its importance in lymphatic remodeling. One challenge is the scarcity of successful animal models of lymphedema. For example, mouse models of lymphatic injuries from the tail have been a successful model helping us grow our knowledge of postsurgical lymphedema [50–52], however, the diminutive size of vessels compared to other species has been an obstacle to study mechanics. Here, we introduced a novel rat tail model representing a long chain of lymphatic vessels with a larger size. In addition, since the human lymphatic network is composed of coordinated chains of vessels to efficiently pump lymph, the study of lymphatic function or dysfunction in the context of a lymphatic chain provides more insight into the function or dysfunction of the lymphatic system [74,174]. The rat tail model provides a unique anatomy due to the close arrangement of parallel collectors compared to other tissue beds. That could be an advantage to study lymphatic vessel remodeling compared to vessels from beds where greater distances between collectors are present. Overall, the size and accessibility of lymphatic vessels from rat tails make it suitable to bridge the gap in our knowledge of lymphatic biomechanics in health and disease, while still taking advantage of a small animal model.

Recent histological assessments in a novel mouse model of lymphatic injury have shown that lymphatic vessels exhibit abnormal structure following lymphatic ligation [54]. The vessel located at the distal side of the wound showed dilated lumen and abnormal valve morphology associated with permanent decline in lymphatic pumping generation. Using our novel animal model we tested and showed the feasibility of surgical lymphatic ligation in the rat tail as a novel system model to study the remodeling of collecting lymphatic vessels following lymphatic injury. Our animal model was aimed to provide a novel microsurgical animal model to study structural and material remodeling of collecting lymphatic vessels. Our in-vivo imaging and histological analysis suggest that vessels distal to the ligation site undergo structural and functional remodeling. This observation supports the previous clinical observations of lymphatic remodeling following lymphatic injury. For example, a biopsy study of lymphedema patients has suggested lymphatic vessels the collecting vessels undergo sclerosis and muscle proliferation especially in the later stages of lymphedema.

Our *in-vivo* imaging demonstrates a remodeling/lymphangiogenic response reroutes injured vessels to dermal initial lymphatic to either bypass the injured site or connect an injured vessel to intact contralateral. This has significant clinical implications as it suggests that vessels that show a higher density of the collateral formation exhibit a more noticeable loss of lymphatic function. Historically, it is believed that an impaired regeneration process after surgical insult, in particular, an impaired collateral formation of lymphatic vessels, drives the lymphedema onset and progression [189]. More recent studies suggest a chronic inflammatory response may play a key role in the disease pathophysiology. Our study suggests that both injured and contralateral vessels are subject to overloads following lymphatic injury.

Specifically, collateral formation exposes distal vessels to overloads (pressure) as the collateral formation would increase resistance to lymph flow and thus distal vessels would need to work harder to transport lymph. Conversely, rerouting to the uninjured vessel exposes contralateral vessels to a larger volume of lymph (lymph flow overload) to compensate for the injured vessels. This could happen either via the lymphatic rerouting or a connection via the network of initial lymphatics distal the injured site.

The current study paves the way for future studies to investigate the mechanics of lymphatic vessels in disease. The rat tail model has the potential to serve as a novel animal model for the study of lymphatic remodeling following surgery and swelling, similar to the currently available mice models. The size of rat tail lymphatic vessels (~300μ) is suitable for mechanical tests, unlike mouse lymphatics models in which these types of tests are very challenging. In addition, the location of the vessel in rat tails is also very accessible and requires fewer incisions compared to thoracic and mesenteric lymphatics. These vessels are all afferent (pre-nodal), hence they mainly drain and pump interstitial fluid from the rat tail. Further, the vessels are located adjacent to the skin which makes the tail very suitable for *in vivo* imaging techniques of lymphatic function such as the near-infrared technique. For example, our previous computational-experimental study showed that the maximum pressure generation to overcome the challenging pressure gradient along a chain is a function of the lymphangion number in a chain and consequently, the maximum pressure generation measured in rat tails increases from the tip toward the base of the tail [74]. The above-mentioned advantages of rat tail lymphatics and the aforementioned biomechanical tests make the rat tail model a potential candidate for developing an animal model to study the role of mechanics in lymphatic disease.

CHATER 6. CONCLUSIONS AND FUTURE DIRECTION

The overall objective of this study was to utilize a combined experimental-computational approach to study the effect of mechanical loads on the lymphatic function and long-term remodeling associated with the mechanical overloads post-lymphatic injury. We developed a novel rat tail model to study lymphatic biomechanics. We believe that this animal model can serve the lymphatic field to provide a better understanding of the roles that lymphatic biomechanics play in health and disease. Using the rat tail model, we made the observation that the lymphatic vessels are under pre-axial stretch *in-situ.* We used ex-vivo experiment on the isolated lymph at vessels from the rat tail to test our hypothesis that the axial stretch is a modulator of lymphatic function. We also used two-photon imaging to quantify the orientation of collagen fibers in the collecting lymphatic vessels from the rat tail. Analyzing imaging data using the curvelet denoising filter and an automated fiber extraction technique revealed that the most collagen fibers are aligned in the longitudinal direction. Further, immunostaining of lymphatic muscle cells showed that most muscle cells are aligned in the circumferential direction, however, actin fiber alignment can be heterogeneous. Second, ex-vivo experiments on the isolate lymphatic vessels were performed to study the effect of exogenous NO on the lymphatic contractility. Further, we performed biaxial testing on the isolated lymphatic vessels from the rat tail. We extended a previously developed constitutive framework to model the effect of exogenous NO on the lymphatic contractility. This constitutive framework enables us to study the response of lymphatic vessels to different mechanical and biomechanical stimuli. We also used near-infrared (NIR) technique along with the application of dermal NO donor to study the effect of NO

on the lymphatic contractility in the context of a lymphangion chain *in-vivo*. These experiments confirmed that the maximum pressure that can be achieved along with a lymphangion chain increase with the tail length and decreases with the application of dermal NO. We also performed simulations for a lymphangion chain to show that the change in lymphatic muscle force production can explain the in-vivo observations. Third, we used the rat tail to develop a novel lymphatic injury model to test our hypothesis that the lymphatic vessels remodel in response to injury and associated mechanical overloads. In this novel animal model, large segments of rat tail lymphatic vessels were excised from one side of the tail while the contralateral vessel on the opposite side was kept intact. Using longitudinal NIR imaging we showed that a remodeling response reroutes the injured vessel to the dermal lymphatic vessels. Interestingly, most of the injured vessels connected to an intact lymphatic vessel to bypass lymphatic injury. The results of biaxial testing and histological assessments suggest that the vessels distal to the injured site change their biomechanical and material properties.

APPENDIX. A NIR IMAGING

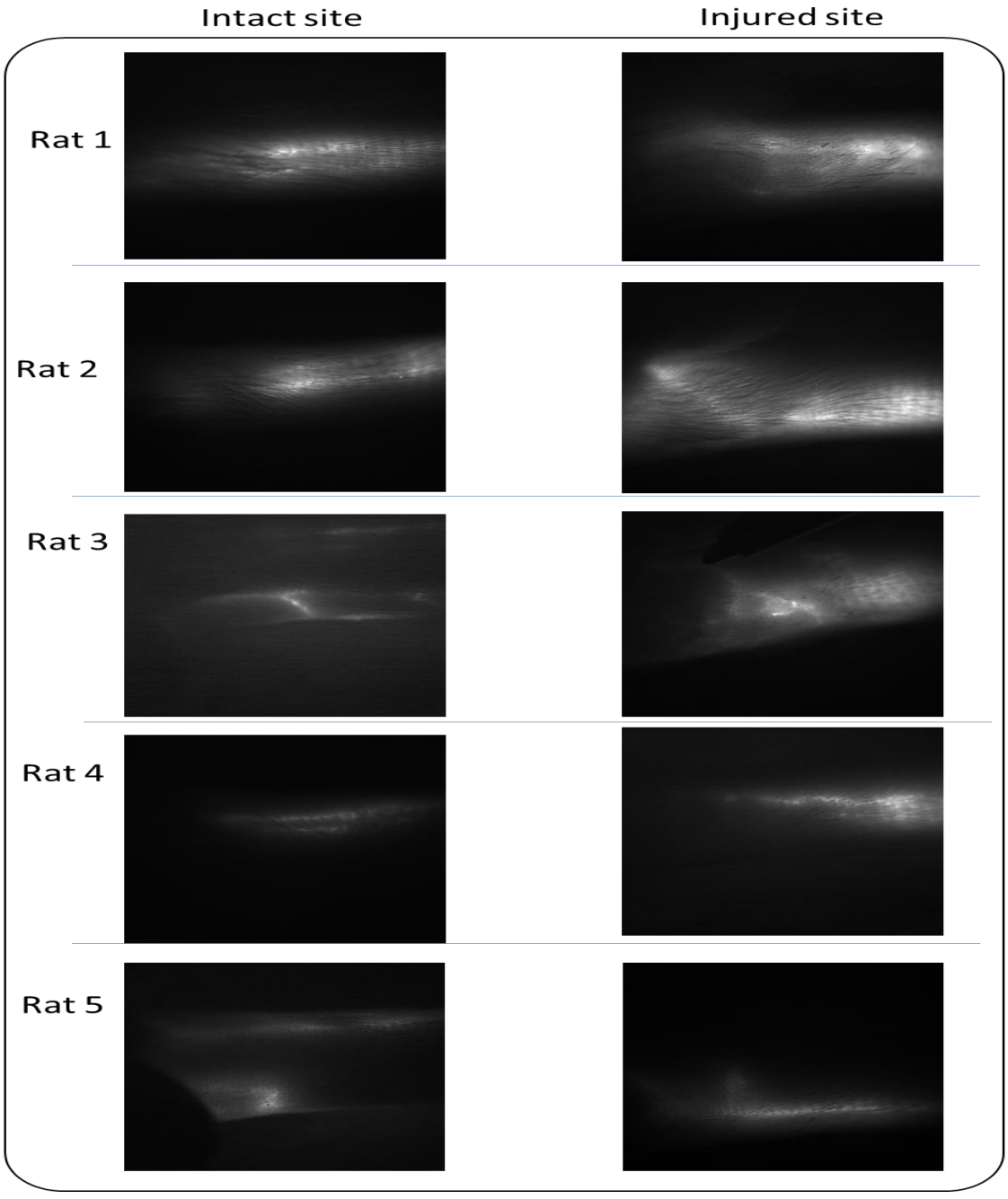

Fig. S1 NIR imaging of rat lymphatic vasculature 4 week post surgery.

APPENDIX. B LYMPHANGION MATLAB CODE

1. **Simulation Script:**

```
%**************Lymphangion G&R
Code******************
%***************** V3***
11/20/2016*********************
clear;
% close all;
for l=1:1
    Variables;
%%%%%%%%%%
i=1;
PEX=0;
nlymph=1
while i<2

pa=3+0*(i-1)*0.5;%inlet pressure
pb=3+(i-1)*1;%outlet pressure
inlet_pressure(i)=pa;
outlet_pressure(i)=pb;
factor=1%0*(1+0.2*(i-1));
[mean_Q2,Qout,mean_tau_w
,mean_sigma_w,mean_diameter,Q1,Q2,r,Q_1,Q_2]=Ma
in(pa,pb,nlymph,factor,PEX)
k=1:nlymph;
mWSS(i,k)=mean_tau_w(k); %Mean Wall Shear
Stress ()
mHoop_Stress(i,k)=mean_sigma_w(k); %Mean Hoop
Stress ()
% mTransmural_Pressure(i)=mean_P;  % Mean
Transmural Pressure [mmHg]
% mFlow(i)=mean_Q; % Mean Flow Rate (mL/min)

% mFlow_v1(i)=mean_Q1; % Mean Flow Rate 2nd
Valve(mL/min)
```

```
mFlow_v2(i)=mean_Q2 ;% Mean Flow Rate 1st
Valve(mL/min)
Qoutflow(:,i)=Qout
if mFlow_v2(i)<-0.00001
    break
end
mD(i,k)=mean_diameter(k);
% mSD(i)=systolic_diameter;
% mDD(i)=diastolic_diameter;
i=i+1
end
%  i=1:40
%  mFlow_v2(i)=mean(Qoutflow(:,i))

colors = {'k','b','k','g','y','c','m'};
types = {'o','*','+','s','x','.','d'};
linetypes={'-','--',':','-','--'};
 m=1
msize=3
figure (8)
hold on
plot((outlet_pressure-
inlet_pressure),mWSS,'LineWidth',1.5,'Color',co
lors{m},'LineStyle',linetypes{m},'MarkerSize',m
size,'Marker',types{m});
xlabel('(Outflow Pressure)-(Inflow Pressure)
[mmHg]','FontWeight','bold','FontSize',20,...
    'FontName','Times New Roman');
ylabel('Mean WSS
(dyne/cm^2)','FontWeight','bold','FontSize',20,
...
    'FontName','Times New Roman');
set(gca,'FontName','Helvica','FontSize',13,'Fon
tWeight','bold',...
'LineWidth',1.5)
% % legend('Collapsible','3 point Model
(Bertram 2014)','Poiseuille')
%
```

```
% figure (9)
% hold on
% plot((outlet_pressure-
inlet_pressure),mFlow,'LineWidth',1.5,'Color',c
olors{m},'LineStyle',linetypes{m},'MarkerSize',
msize,'Marker',types{m});
% xlabel('(Outflow Pressure)-(Inflow Pressure)
[mmHg]','FontWeight','bold','FontSize',20,...
%     'FontName','Times New Roman');
% ylabel('Mean Flow
(mL/min)','FontWeight','bold','FontSize',20,...
%     'FontName','Times New Roman');
%
set(gca,'FontName','Helvica','FontSize',13,'Fon
tWeight','bold',...
% 'LineWidth',1.5)
% figure (10)
% hold on
% plot((outlet_pressure-
inlet_pressure),mTransmural_Pressure,'LineWidth
',1.5,'Color',colors{m},'LineStyle',linetypes{m
},'MarkerSize',msize,'Marker',types{m});
% xlabel('(Outflow Pressure)-(Inflow Pressure)
[mmHg]','FontWeight','bold','FontSize',20,...
%     'FontName','Times New Roman');
% ylabel('Mean Transmural Presssure
[mmHg]','FontWeight','bold','FontSize',20,...
%     'FontName','Times New Roman');
%
set(gca,'FontName','Helvica','FontSize',13,'Fon
tWeight','bold',...
% 'LineWidth',1.5)
figure (11)
hold on
plot((outlet_pressure-
inlet_pressure),mHoop_Stress,'LineWidth',1.5,'C
olor',colors{m},'LineStyle',linetypes{m},'Marke
rSize',msize,'Marker',types{m});
```

```
xlabel('(Outflow Pressure)-(Inflow Pressure)
[mmHg]','FontWeight','bold','FontSize',20,...
    'FontName','Times New Roman');
ylabel('Mean Total Hoop Stress
(dyne/cm^2)','FontWeight','bold','FontSize',20,
...
    'FontName','Times New Roman');
set(gca,'FontName','Helvica','FontSize',13,'Fon
tWeight','bold',...
'LineWidth',1.5)
% figure (12)
% hold on
% plot((outlet_pressure-
inlet_pressure),mD,'LineWidth',1.5,'Color',colo
rs{m},'LineStyle',linetypes{m},'MarkerSize',msi
ze,'Marker',types{m});
% xlabel('(Outflow Pressure)-(Inflow Pressure)
[mmHg]','FontWeight','bold','FontSize',20,...
%     'FontName','Times New Roman');
% ylabel('Mean Diameter
(\mum)','FontWeight','bold','FontSize',20,...
%     'FontName','Times New Roman');
%
set(gca,'FontName','Helvica','FontSize',13,'Fon
tWeight','bold',...
% 'LineWidth',1.5)
%
% figure (13)
% hold on
% plot((outlet_pressure-
inlet_pressure),mSD,'LineWidth',1.5,'Color',col
ors{m},'LineStyle',linetypes{m},'MarkerSize',ms
ize,'Marker',types{m});
% % xlabel('(Outflow Pressure)-(Inflow
Pressure)
[mmHg]','FontWeight','bold','FontSize',20,...
% %     'FontName','Times New Roman');
```

```
% % ylabel('Mean Systolic Diameter
(\mum)','FontWeight','bold','FontSize',20,...
% %     'FontName','Times New Roman');
% %
set(gca,'FontName','Helvica','FontSize',13,'Fon
tWeight','bold',...
% % 'LineWidth',1.5)
% %
%
%
% %figure (14)
% hold on
% plot((outlet_pressure-
inlet_pressure),mDD,'LineWidth',1.5,'Color',col
ors{m},'LineStyle',linetypes{m},'MarkerSize',ms
ize,'Marker',types{m});
% xlabel('(Outflow Pressure)-(Inflow Pressure)
[mmHg]','FontWeight','bold','FontSize',20,...
%     'FontName','Times New Roman');
% ylabel('Mean Diastolic& Systolic Diameters
(\mum)','FontWeight','bold','FontSize',20,...
%     'FontName','Times New Roman');
%
set(gca,'FontName','Helvica','FontSize',13,'Fon
tWeight','bold',...
% 'LineWidth',1.5)
%
% figure (15)
% hold on
% plot((outlet_pressure-
inlet_pressure),mFlow_v1,'LineWidth',1.5,'Color
',colors{m},'LineStyle',linetypes{m},'MarkerSiz
e',msize,'Marker',types{m});
% xlabel('(Outflow Pressure)-(Inflow Pressure)
[mmHg]','FontWeight','bold','FontSize',20,...
%     'FontName','Times New Roman');
% ylabel('1st Valve Mean Flow
(mL/min)','FontWeight','bold','FontSize',20,...
```

```
%     'FontName','Times New Roman');
%
set(gca,'FontName','Helvica','FontSize',13,'Fon
tWeight','bold',...
% 'LineWidth',1.5)
figure (16)
hold on
plot((outlet_pressure-
inlet_pressure),mFlow_v2,'LineWidth',1.5,'Color
',colors{m},'LineStyle',linetypes{m},'MarkerSiz
e',msize,'Marker',types{m});
xlabel('(Outflow Pressure)-(Inflow Pressure)
[mmHg]','FontWeight','bold','FontSize',15,...
    'FontName','Times New Roman');
ylabel('2nd Valve Mean Flow
(mL/min)','FontWeight','bold','FontSize',15,...
    'FontName','Times New Roman');
set(gca,'FontName','Helvica','FontSize',13,'Fon
tWeight','bold',...
'LineWidth',1.5)

if l==1
 save('n=1H=100pe00')
    elseif l==2
 save('n=1H=100pe05')
    elseif l==3
 save('n=1H=100pe10')
     elseif l==4
 save('n=1H=100pe15')
     elseif l==5
         save('n=1H=100pe20')
 end
end
```

2. cmodel script:

```
function [p_mod, fz, lq, lr, tq, tq_pas,
tq_act, tz, h] = cmodel(ri,Tact,pex)

Variables;
%%%%%%%%%%%%%%%%%%%%%%%%%%%%%%%%%%%%%%%%%%%%%%%
%%%%%%%

% lz = 1.15;
% samp = 1; %Number of vessels in the chain
%
% % Applied loads
% % pa = 2*980;  %2.1916*980;    % dynes/cm^2
(1 cmH2O = 980 dynes/cm^2);
%
% % Fluid properties
% visc = 0.01;        %*0.0001;
% rho = 1;            %g/cm^3;
%
% % Valve resistance parameters (Bertram et al
2013)
% RVn = 600*100;          %
(dynes/cm^2)/(ml/sec)
% RVx = 12*10^7;      % (dynes/cm^2)/(ml/sec)
% Po =0;
% so=0.2; % non-dimensioanl
%
%
%
%    lz = 1.15;
% samp = 1; %Number of vessels in the chain
%
%
%
% % Fluid properties
% visc = 0.01;        %
```

```
%
%
%
%
%
% % Active constitutive model parameters (Alex
Caulk  2015)
%
% lq_max =1.15;
% lq_o =0.6119;
% lq_high = 2*lq_max-lq_o;
% slope0 = 13.0981;
% int = -4574.4;
%
% % Vessel geometry
% Ro0 = 804/2*0.0001;
% H0 = 58*0.0001*1.0;
% L = 0.3046;
% H= H0;
% Ro= Ro0;
% Ri = Ro - H;
% % Passive
% b =1.9235e+04;
% b11 =1.9083e+03;
% b21 =27.2123;
% b12 = 4.7515e+04;
% b22 = 4.8137;
% b13 = 2.7769e+03;
% b23 =34.9830;
% alpha1 =1.5708;
% alpha2 = 0;
% alpha3 =  0.8492;
% alpha4 =  -0.8492;
%
%
% %%%%T act Values%%%%%%%
% T_tonic=30000/2;
% % T_phasic=80000;
```

```
% % TT=486348.7903/5;
% % b=0.05
% % T_tonic=38000+0*TT*b/(1+b);
%  T_phasic=225000;
%
%
%%%%%%%%%%%%%%%%%%%%%%%%%%%%%%%%%%%%%%%%%%%%%%%
%%%%%%%
% ww=2; % contraction time
% tr=6;% %referactory time (11.3;%2.62 )
%
%%%%%%%%%%%%%%%%%%%%%%%%%%%%%%%%%%%%%%%%%%%%%%%
%%%%%%%

for i = 1:length(ri)
    %Calculate loaded thickness from
incompressibility

    coef_c = -1*H(i)*(2*Ri(i)+H(i))/lz;
    coef_b = 2*ri(i);
    coef_a = 1;
    D1 = [coef_a, coef_b, coef_c];
    E1 = roots(D1);
    F1 = E1(2);
    h(i) = F1';

    % Kinematics
    lq(i) = (ri(i)+h(i)/2)/(Ri(i)+H(i)/2);
    lr(i) = 1/(lq(i)*lz);
    Fqq = lq(i);
    Fzz = lz;
    Frr = lr(i);
    Crr = Frr^2;
    Cqq = Fqq^2;
    Czz = Fzz^2;
    Err = (Crr-1)/2;
    Eqq = (Cqq-1)/2;
    Ezz = (Czz-1)/2;
```

```
    lambda2_k1 = Cqq*(sin(alpha1))^2 +
Czz*(cos(alpha1))^2;
    lambda2_k2 = 0*Cqq*(sin(alpha2))^2 +
Czz*(cos(alpha2))^2;
    lambda2_k3 = Cqq*(sin(alpha3))^2 +
Czz*(cos(alpha3))^2;
    lambda2_k4 = Cqq*(sin(alpha4))^2 +
Czz*(cos(alpha4))^2;

    %Strain energy function proposed by
Holzapfel for four fiber families
    tr_hat = 2*Crr*b;
    tq_hat = 2*Cqq*(b +
b11/2*exp(b21*(lambda2_k1-
1)^2)*(Cqq*(sin(alpha1))^4 +
Czz*(sin(alpha1))^2*(cos(alpha1))^2 -
(sin(alpha1))^2) + ...
        0*b12/2*exp(b22*(lambda2_k2-
1)^2)*(Cqq*(sin(alpha2))^4 +
Czz*(sin(alpha2))^2*(cos(alpha2))^2 -
(sin(alpha2))^2) + ...
        b13*exp(b23*(lambda2_k3-
1)^2)*(Cqq*(sin(alpha3))^4 +
Czz*(sin(alpha3))^2*(cos(alpha3))^2 -
(sin(alpha3))^2));
    tz_hat = 2*Czz*(b +
b11/2*exp(b21*(lambda2_k1-
1)^2)*(Cqq*(sin(alpha1))^2*(cos(alpha1))^2 +
Czz*(cos(alpha1))^4 - (cos(alpha1))^2) + ...
        0*b12/2*exp(b22*(lambda2_k2-
1)^2)*(Cqq*(sin(alpha2))^2*(cos(alpha2))^2 +
Czz*(cos(alpha2))^4 - (cos(alpha2))^2) + ...
        b13*exp(b23*(lambda2_k3-
1)^2)*(Cqq*(sin(alpha3))^2*(cos(alpha3))^2 +
Czz*(cos(alpha3))^4 - (cos(alpha3))^2));

    % Calculate active stress
```

```
    tq_pas(i) = tq_hat - tr_hat;
    tz(i) = tz_hat - tr_hat;

    % Calculate active stress
    if lq(i) <= lq_high && lq(i) >= lq_o;
        tq_act(i) = Tact(i)*lq(i)*(1-((lq_max-
lq(i))/(lq_max-lq_o))^2);
    else
        tq_act(i) = 0;
    end



    tq(i) = tq_act(i) + tq_pas(i);

    p_mod(i) = h(i)/ri(i)*(tq(i) + pex) + pex;
    fz(i) = pi*h(i)*(2*ri(i)+h(i))*tz(i);

end
```

3. **Diameter_Initial Script:**

```
function error=
Diameter_Initial(R,nlymph,Tact,p_mod,pex)
for k=1:nlymph
error(k)= (cmodel(R(k),Tact(k),pex(k)) -
p_mod(k))*10000;
end



% error(1)= (cmodel(R(1),Tact(1)) -
p_mod(1))*10000;
% error(2)= (cmodel(R(2),Tact(2)) -
p_mod(2))*10000;
```

4. **diameterp Script:**

```
function F =
diameterp(p,pa,pb,Tact,R0,dt,nLymph,pex)
Variables;


for i=1:nLymph
if nLymph == 1
    F(1)=cmodel((p(3)/1),Tact(1),pex(1))-
(p(1)+p(2))/2;
    F(2)=p(2)-
p(1)+(8*visc*L/(pi*(p(3)/1)^4))*(((pa-
p(1))/(RVn + RVx*(1/(1+exp(so*((pa-p(1))-
Po))))))+((p(2)-pb)/(RVn +
RVx*(1/(1+exp(so*((p(2)-pb)-Po)))))))/2;
    F(3)=(L*pi*((p(3)/1)^2-R0(1)^2)/dt+(-
1*((pa-p(1))/(RVn + RVx*(1/(1+exp(so*((pa-
p(1))-Po))))))+((p(2)-pb)/(RVn +
RVx*(1/(1+exp(so*((p(2)-pb)-Po)))))));

elseif nLymph==2
    F(1)=cmodel((p(3)/1),Tact(1),pex(1))-
(p(1)+p(2))/2;
    F(2)=p(2)-
p(1)+(8*visc*L/(pi*(p(3)/1)^4))*(((pa-
p(1))/(RVn + RVx*(1/(1+exp(so*((pa-p(1))-
Po))))))+((p(2)-p(4))/(RVn +
RVx*(1/(1+exp(so*((p(2)-p(4))-Po)))))))/2;
    F(3)=L*pi*((p(3)/1)^2-R0(1)^2)+dt*(-1*((pa-
p(1))/(RVn + RVx*(1/(1+exp(so*((pa-p(1))-
Po))))))+((p(2)-p(4))/(RVn +
RVx*(1/(1+exp(so*((p(2)-p(4))-Po)))))));
    F(4)=cmodel((p(6)/1),Tact(2),pex(2))-
(p(4)+p(5))/2;
    F(5)=p(5)-
p(4)+(8*visc*L/(pi*(p(6)/1)^4))*(((p(2)-
p(4))/(RVn + RVx*(1/(1+exp(so*((p(2)-p(4))-
```

```
Po))))))+((p(5)-pb)/(RVn +
RVx*(1/(1+exp(so*((p(5)-pb)-Po)))))))/2;
    F(6)=L*pi*((p(6)/1)^2-R0(2)^2)+dt*(-
1*((p(2)-p(4))/(RVn + RVx*(1/(1+exp(so*((p(2)-
p(4))-Po))))))+((p(5)-pb)/(RVn +
RVx*(1/(1+exp(so*((p(5)-pb)-Po)))))));

else

        fac=1;
     F(1)=fac*(cmodel((p(3)/1),Tact(1),pex(1))-
(p(1)+p(2))/2);
    F(2)=fac*(p(2)-
p(1)+(8*visc*L/(pi*(p(3)/1)^4))*(((pa-
p(1))/(RVn + RVx*(1/(1+exp(so*((pa-p(1))-
Po))))))+((p(2)-p(4))/(RVn +
RVx*(1/(1+exp(so*((p(2)-p(4))-Po)))))))/2);
    F(3)=fac*((L*pi*((p(3)/1)^2-R0(1)^2)+dt*(-
1*((pa-p(1))/(RVn + RVx*(1/(1+exp(so*((pa-
p(1))-Po))))))+((p(2)-p(4))/(RVn +
RVx*(1/(1+exp(so*((p(2)-p(4))-Po)))))))));

for i=2:nLymph-1

    F(3*i-
2)=fac*(cmodel((p(3*i)/1),Tact(i),pex(i))-
(p(3*i-2)+p(3*i-1))/2);
    F(3*i-1)=fac*(p(3*i-1)-p(3*i-
2)+(8*visc*L/(pi*(p(3*i)/1)^4))*(((p(3*i-4)-
p(3*i-2))/(RVn + RVx*(1/(1+exp(so*((p(3*i-4)-
p(3*i-2))-Po))))))+((p(3*i-1)-p(3*i+1))/(RVn +
RVx*(1/(1+exp(so*((p(3*i-1)-p(3*i+1))-
Po)))))))/2);
    F(3*i)=fac*((L*pi*((p(3*i)/1)^2-
R0(i)^2)+dt*(-1*((p(3*i-4)-p(3*i-2))/(RVn +
RVx*(1/(1+exp(so*((p(3*i-4)-p(3*i-2))-
Po))))))+((p(3*i-1)-p(3*i+1))/(RVn +
```

```
RVx*(1/(1+exp(so*((p(3*i-1)-p(3*i+1))-
Po)))))))));

end
  F(3*nLymph-
2)=fac*(cmodel((p(3*nLymph)/1),Tact(nLymph),pex
(nLymph))-(p(3*nLymph-2)+p(3*nLymph-1))/2);
    F(3*nLymph-1)=fac*(p(3*nLymph-1)-
p(3*nLymph-
2)+(8*visc*L/(pi*(p(3*nLymph)/1)^4))*(((p(3*nLy
mph-4)-p(3*nLymph-2))/(RVn +
RVx*(1/(1+exp(so*((p(3*nLymph-4)-p(3*nLymph-
2))-Po)))))+((p(3*nLymph-1)-pb)/(RVn +
RVx*(1/(1+exp(so*((p(3*nLymph-1)-pb)-
Po)))))))/2);
    F(3*nLymph)=fac*((L*pi*((p(3*nLymph)/1)^2-
R0(nLymph)^2)+dt*(-1*((p(3*nLymph-4)-
p(3*nLymph-2))/(RVn +
RVx*(1/(1+exp(so*((p(3*nLymph-4)-p(3*nLymph-
2))-Po)))))+((p(3*nLymph-1)-pb)/(RVn +
RVx*(1/(1+exp(so*((p(3*nLymph-1)-pb)-
Po)))))))));


end
end
end
```

5. **fandv Script:**

```
function F = fandv(p,pm,pa,pb,Rf,nlymph)
Variables;

if nlymph==1
     F(1)=pm(1)-(p(1)+p(2))/2;
     F(2)=p(2)-p(1)+Rf(1)*(((pa-p(1))/(RVn +
RVx*(1/(1+exp(so*((pa-p(1))-Po)))))+((p(2)-
```

```
pb)/(RVn + RVx*(1/(1+exp(so*((p(2)-pb)-
Po)))))))/2;
else
for k=1:nlymph

    if k==1
        F(1)=pm(1)-(p(1)+p(2))/2;
        F(2)=p(2)-p(1)+Rf(1)*(((pa-p(1))/(RVn +
RVx*(1/(1+exp(so*((pa-p(1))-Po))))))+((p(2)-
p(3))/(RVn + RVx*(1/(1+exp(so*((p(2)-p(3))-
Po)))))))/2;
    elseif k==nlymph
    F(2*k-1)=pm(k)-(p(2*k-1)+p(2*k))/2;
    F(2)=p(2*k)-p(2*k-1)+Rf(k)*(((p(2*k-2)-
p(2*k-1))/(RVn + RVx*(1/(1+exp(so*((p(2*k-2)-
p(2*k-1))-Po))))))+((p(2*k)-pb)/(RVn +
RVx*(1/(1+exp(so*((p(2*k)-pb)-Po)))))))/2;

    else
    F(2*k-1)=pm(k)-(p(2*k-1)+p(2*k))/2;
    F(2*k)=p(2*k)-p(2*k-1)+Rf(k)*(((p(2*k-2)-
p(2*k-1))/(RVn + RVx*(1/(1+exp(so*((p(2*k-2)-
p(2*k-1))-Po))))))+((p(2*k)-p(2*k+1))/(RVn +
RVx*(1/(1+exp(so*((p(2*k)-p(2*k+1))-
Po)))))))/2;

    end
end
end
```

6. **Main Script:**

```
function [mean_Q2,Qout,mean_tau_w
,mean_sigma_w,mean_diameter,Q1,Q2,r,Q_1,Q_2,Vol
umeo,p_cmH2O] =
Main_Ligation(pa_mmhg,pb_mmhg,nlymph,~,PEX)
```

```
Variables;


x0(1:nlymph)=.01 ;%Initial Guess for
Diameter(cm)
pa=pa_mmhg*1333.2239;
pb=pb_mmhg*1333.2239; %inflow&outflow pressure
[mmHg]
%N=201% number of time steps
dt=0.01;%2*ww/(N-1); %time step
NN=4%number of cycle
N=NN*(ww+tr)/dt+1;
l=1:ww/dt+1;
m=1:nlymph
phi=0.1
Tp(l,m)=( 1- cos(phi*(m-1)+2*pi*1/ww*(dt*(l-
1))))*T_phasic/2+ T_tonic
Tt(1:tr/dt,1:nlymph)=T_tonic
Ta=[Tp' Tt' Tp' Tt' Tp' Tt' Tp' Tt']
Ta=Ta'

for i=1:N
    if i==1
        k=1:nlymph
p_mod=(pa+pb)/2;
p_mod(k)=pa+(pb-pa)*k/(nlymph*2)
;%%%%%%%%%%%%%%%%%%%%%%%%this parameter dictates
initial diameter-pressure
Tact(k)=T_tonic;
pex(k)=PEX;
f =
@(R)Diameter_Initial(R,nlymph,Tact,p_mod,pex);
[R,fval] = lsqnonlin(f,x0);
for k=1:nlymph
pm(k)=cmodel(R(k),Tact(k),pex(k));
Rf(k)=8*visc*L/(pi*R(k)^4);
end
```

```
r(i,:)=R;

for k=1:nlymph
    if nlymph==1
    xo(1)=(pa+pm(1))/2;
    xo(2)=(pb+pm(1))/2;
    else
    if (k==1)
        xo(1)=(pa+pm(1))/2;
        xo(2)=(pb+pm(nlymph))/2;
    elseif (k==nlymph)
        xo(2*k-1)=(pm(k)+pm(k-1))/2;
        xo(2*k)=(pm(k)+pb)/2;
    else
        xo(2*k-1)=(pm(k)+pm(k-1))/2;
        xo(2*k)=(pm(k)+pm(k+1))/2;
    end
    end
end
xo;
Rf;
% x0 = [(pa+pm)/2,(pb+pm)/2];
f = @(p)fandv(p,pm,pa,pb,Rf,nlymph);
% x0 = [0,0];
% x = fsolve(fun,x0)fandv(p,pm,pa,pb,Rf)
[x,fval]=lsqnonlin(f,xo);
% [y,ffval]=lsqnonlin(f,x0);

% g = @(p)fandvb(p,pm,pa,pb,Rf);
% x0 = [0,0];
% % x = fsolve(fun,x0)fandv(p,pm,pa,pb,Rf)
% [z,fval] = fsolve(g,x0);
% [w,ffval]=lsqnonlin(g,x0);
% p1=z(1);
% p2=z(2);
for k=1:nlymph
p1(i,k)=x(2*k-1);
p2(i,k)=x(2*k);
```

```
end
[Q1,Q2] = valveflow(pa,pb,p1,p2,nlymph);
% p1=x(1);
% p2=x(2);
% [Q11,Q22] = valveflow(pa,pb,p1,p2);
time(i)=0;

for k=1:nlymph
p_t(i,k)=cmodel(R(k),Tact(k),pex(k));
T(i,k)=Tact(k);
end

    else
         i

        ddt=dt*(i-1);
        time(i)=ddt;
%      ( 1-  cos(2*pi*ww*(ddt)))
phi=0.1
 for k=1:nlymph;
     Tact(k)=Ta(i,k)
%       Tact(k)=( 1- cos(phi*(k-
1)+2*pi*1/ww*(ddt)))*T_phasic/2+ T_tonic;
      T(i,k)=Tact(k);
        pex(k)=0*( 1-  cos(phi*(k-
1)+2*pi*1/ww*(ddt)))*PEX+PEX;
        Pex(i,k)=pex(k);
 end

     for  k=1:nlymph
       R(i,k)=r(i-1,k) ;
       Ro(k)= R(i,k);
       x1(3*k-1) = p1(i-1,k);
       x1(3*k-2) = p2(i-1,k);
       x1(3*k) = R(i,k);
     end
      f =
@(p)diameterp(p,pa,pb,Tact,Ro,dt,nlymph,pex);
```

```
        [x,fval] = lsqnonlin(f,x1);
         k=1:nlymph
        r(i,k)= x(3*k);
        p1(i,k)=x(3*k-2);
        p2(i,k)=x(3*k-1);
        p11(k)=p1(i,k);
        p22(k)= p2(i,k);
        R_t(i,k)=r(i,k);
        rr=r(i,k);
        for k=1:nlymph
    %    p_t(i,k)=cmodel(r(i,k),T(i,k),pex(k));
        [p_t(i,k),fz(i,k), lq(i,k), lr(i,k),
tq(i,k), tq_pas(i,k), tq_act(i,k), tz(i,k),
h(i,k)]=cmodel(r(i,k),T(i,k),pex(k));

       end
%      [p_t(i),fz(i), lq(i), lr(i), tq(i),
tq_pas(i), tq_act(i), tz(i),
h(i)]=cmodel(R_t,Tact);

       [Q1,Q2] =
valveflow(pa,pb,p11,p22,nlymph);
%        qq(i)=Q1
%        qqq(i)=Q2
        k=1:nlymph
        Q_1(i,k)=Q1(1,k);
        Q_2(i,k)=Q2(1,k);
        Q_m(i,k)=(Q_1(i,k)+ Q_2(i,k))*0.5;

% figure (30)
% plot(Q_1)
%
% figure (31)
% plot(Q_2)

end
% % figure (29)
% % plot(r)
```

```
%
% figure (32)
% plot(p_t)

end


k=1:nlymph
wss(:,k) = 4*visc*Q_m(:,k)./(pi*r(:,k).^3);
mean_tau_w(k) = mean(wss(201:N,k)); %
mean_sigma_w(k) = mean(tq(201:N,k)); %
Volume=pi*r(201:N,k).^2*L*lz;
Volumeo=pi*r(:,k).^2*L*lz;
mean_Q2 = mean(60*Q_2(201:N,nlymph)); % Mean
Flow Rate (mL/min)
Qout=60*Q_2(201:N,nlymph);

colors = {'k','b','k','g','y','c','m'};
types = {'o','*','+','s','x','.','d'};
linetypes={'-','--',':','-','--'};
m=1;
msize=0.3;
hold on
figure (1)
r_micron=10000*r;
k=1:nlymph
mean_diameter(k)=2*mean(r_micron(201:N,k));
plot(time,2*r_micron,'LineWidth',1.5,'Color',co
lors{m},'LineStyle',linetypes{m},'MarkerSize',m
size,'Marker',types{m});
xlabel('Time
(s)','FontWeight','bold','FontSize',25,...
    'FontName','Times New Roman');
ylabel('Diameter
(\mum)','FontWeight','bold','FontSize',25,...
    'FontName','Times New Roman');
set(gca,'FontName','Helvica','FontSize',13,'Fon
tWeight','bold',...
```

```
'LineWidth',1.5);
legend('Collapsible','3 point Model (Bertram
2014)','Poiseuille')
% legend()
% % legend()

hold on
figure (2)
plot(time,T/10000,'LineWidth',1.5,'Color',color
s{m},'LineStyle','-');
xlabel('Time
(s)','FontWeight','bold','FontSize',25,...
    'FontName','Times New Roman');
ylabel('Activation
Parameter(kdyne/cm^2)','FontWeight','bold','Fon
tSize',25,...
    'FontName','Times New Roman');
set(gca,'FontName','Helvica','FontSize',13,'Fon
tWeight','bold',...
'LineWidth',1.5)


hold on
figure (3)
p_cmH2O=p_t/980.665;
plot(time,p_cmH2O,'LineWidth',1.5,'Color',color
s{m},'LineStyle',linetypes{m},'MarkerSize',msiz
e,'Marker',types{m});
xlabel('Time
(s)','FontWeight','bold','FontSize',25,...
    'FontName','Times New Roman');
ylabel('Pressure(cmH_2O)','FontWeight','bold','
FontSize',25,...
    'FontName','Times New Roman');
set(gca,'FontName','Helvica','FontSize',13,'Fon
tWeight','bold',...
'LineWidth',1.5)
```

```
legend('Q_{avg}(Collapsible)')
legend('Collapsible','3 point Model (Bertram
2014)','Poiseuille')
% legend('3 point Model (Bertram 2014)')
% legend('Poiseuille')


hold on
figure (4)
%Q_1 (mL/s)
plot(time,Q_1*60,'LineWidth',1.5,'Color',colors
{m},'LineStyle',linetypes{m},'MarkerSize',msize
,'Marker',types{m});
xlabel('Time
(s)','FontWeight','bold','FontSize',25,...
    'FontName','Times New Roman');
ylabel('1st Valve Flow
Rate(mL/min)','FontWeight','bold','FontSize',25
,...
    'FontName','Times New Roman');
set(gca,'FontName','Helvica','FontSize',13,'Fon
tWeight','bold',...
'LineWidth',1.5)
legend('Collapsible','3 point Model (Bertram
2014)','Poiseuille')
% legend('3 point Model (Bertram 2014)')
% legend('Poiseuille')


hold on
figure (5)
plot(time,Q_2*60,'LineWidth',1.5,'Color',colors
{m},'LineStyle',linetypes{m},'MarkerSize',msize
,'Marker',types{m});
xlabel('Time
(s)','FontWeight','bold','FontSize',25,...
    'FontName','Times New Roman');
```

```
ylabel('2nd Valve Flow
Rate(mL/min)','FontWeight','bold','FontSize',25
,...
    'FontName','Times New Roman');
set(gca,'FontName','Helvica','FontSize',13,'Fon
tWeight','bold',...
'LineWidth',1.5)
legend('Collapsible','3 point Model (Bertram
2014)','Poiseuille')
% legend('3 point Model (Bertram 2014)')
% legend('Poiseuille')


hold on
figure (6)
hold on
plot(time,Q_m*60,'LineWidth',1.5,'Color',colors
{m},'LineStyle',linetypes{m},'MarkerSize',msize
,'Marker',types{m});
xlabel('Time
(s)','FontWeight','bold','FontSize',25,...
    'FontName','Times New Roman');
ylabel('Average Flow
Rate(mL/min)','FontWeight','bold','FontSize',25
,...
    'FontName','Times New Roman');
set(gca,'FontName','Helvica','FontSize',13,'Fon
tWeight','bold',...
'LineWidth',1.5)
legend('Collapsible','3 point Model (Bertram
2014)','Poiseuille')

hold on

figure (7)
hold on
plot(Volumeo(401:size(Volumeo,1)),p_cmH2O(401:s
ize(Volumeo,1)),'LineWidth',1.5,'Color',colors{
```

```
m},'LineStyle',linetypes{m},'MarkerSize',msize,
'Marker',types{m});
xlabel('Volume(mL)','FontWeight','bold','FontSi
ze',25,...
    'FontName','Times New Roman');
ylabel('Pressure(cmH_2O)Volume(mL)','FontWeight
','bold','FontSize',25,...
    'FontName','Times New Roman');
set(gca,'FontName','Helvica','FontSize',13,'Fon
tWeight','bold',...
'LineWidth',1.5)
legend('Collapsible','3 point Model (Bertram
2014)','Poiseuille')
```

7. Variables Script

```
lz = 1.10;
samp = 1; %Number of vessels in the chain

% Applied loads
% pa = 2*980;  %2.1916*980;    % dynes/cm^2 (1
cmH2O = 980 dynes/cm^2);

% Fluid properties
visc = 0.01;        %*0.0001;
rho = 1;            %g/cm^3;

% Valve resistance parameters (Bertram et al
2013)
% RVn = 600*100;          %
(dynes/cm^2)/(ml/sec)
% RVx = 12*10^7;      % (dynes/cm^2)/(ml/sec)
% Po =0;
% so=0.2; % non-dimensioanl

RVn = 6*10^4;           % (dynes/cm^2)/(ml/sec)
RVx = 10^7;      %10^5% (dynes/cm^2)/(ml/sec)
```

```
Po =0;
so=0.1; % non-dimensioanl



% Fluid properties
visc = 0.01;         %



% Active constitutive model parameters (Alex
Caulk  2015)

lq_max =1.85;
lq_o =0.85;
 lq_high = 2*lq_max-lq_o;
% slope0 = 13.0981;
% int = -4574.4;

% Vessel geometry
Ro0 = 252/2*0.0001;
H0 = 19*0.0001;
L = 0.276;
H= H0;
Ro= Ro0;
Ri = Ro - H;
% Passive
b =5.02*10^-7*10^4;
b11 =4.94*10^4;
b21 =5.78*10^-4*10^4;
b12 = 0;
b22 = 0;
b13 = 1.9*10^4;
b23 =5.93*10^-4*10^4;
alpha1 =0;
alpha2 = 0;
```

```
alpha3 =  25.28*3.14/180;
alpha4 =  -alpha3;

C=0.8
%%%%T act Values%%%%%%%%
T_tonic=C*(0.87*3*10^4)
% T_phasic=80000;
% TT=486348.7903/5;
% b=0.05
% T_tonic=38000+0*TT*b/(1+b);
 T_phasic=C*1.6498*10^4

 ww=2;
%  tr=1;
 tr=8
```

REFERENCES

1. Swartz MA. 2001 The physiology of the lymphatic system. *Adv. Drug Deliv. Rev.* **50**, 3–20. (doi:10.1016/S0169-409X(01)00150-8)

2. Gashev AA, Davis MJ, Delp MD, Zawieja DC. 2004 Regional variations of contractile activity in isolated rat lymphatics. *Microcirculation* **11**, 477–492. (doi:10.1080/10739680490476033\nCNFRNP6UXERYYRUV [pii])

3. Bohlen HG, Wang W, Gashev A, Gasheva O, Zawieja D. 2009 Phasic contractions of rat mesenteric lymphatics increase basal and phasic nitric oxide generation in vivo. *Am. J. Physiol. Heart Circ. Physiol.* **297**, H1319-28. (doi:10.1152/ajpheart.00039.2009)

4. Bohlen HG, Wang W, Gashev A, Gasheva O, Zawieja D. 2009 Phasic contractions of rat mesenteric lymphatics increase basal and phasic nitric oxide generation in vivo. *Am. J. Physiol. Heart Circ. Physiol.* **297**, H1319-28. (doi:10.1152/ajpheart.00039.2009)

5. Muthuchamy M, Gashev A, Boswell N, Dawson N, Zawieja D. 2003 Molecular and functional analyses of the contractile apparatus in lymphatic muscle. *FASEB J.* **17**, 920–922. (doi:10.1096/fj.02-0626fje)

6. Wang W, Nepiyushchikh Z, Zawieja DC, Chakraborty S, Zawieja SD, Gashev A a, Davis MJ, Muthuchamy M. 2009 Inhibition of myosin light chain phosphorylation decreases rat mesenteric lymphatic contractile activity. *Am. J. Physiol. Heart Circ. Physiol.* **297**, H726-34. (doi:10.1152/ajpheart.00312.2009)

7. Dixon JB, Greiner ST, Gashev A a, Cote GL, Moore JE, Zawieja DC. 2006 Lymph flow, shear stress, and lymphocyte velocity in rat mesenteric prenodal lymphatics. *Microcirculation* **13**, 597–610. (doi:10.1080/10739680600893909)

8. Davis MJ, Scallan JP, Wolpers JH, Muthuchamy M, Gashev a. a., Zawieja DC. 2012 Intrinsic increase in lymphangion muscle contractility in response to elevated afterload. *AJP Hear. Circ. Physiol.* **303**, H795–H808. (doi:10.1152/ajpheart.01097.2011)

9. Gashev A a, Davis MJ, Zawieja DC. 2002 Inhibition of the active lymph pump by flow in rat mesenteric lymphatics and thoracic duct. *J. Physiol.* **540**, 1023–1037. (doi:10.1113/jphysiol.2001.016642)

10. Zhang R-Z, Gashev AA, Zawieja DC, Davis MJ. In press. Length-tension relationships of small arteries, veins, and lymphatics from the rat mesenteric microcirculation.

11. Moriondo A, Solari E, Marcozzi C, Negrini D. 2016 Lymph flow pattern in pleural

diaphragmatic lymphatics during intrinsic and extrinsic isotonic contraction. *Am. J. Physiol. Heart Circ. Physiol.* **310**, H60-70. (doi:10.1152/ajpheart.00640.2015)

12. Beckett E a H, Hollywood M a, Thornbury KD, McHale NG. 2007 Spontaneous electrical activity in sheep mesenteric lymphatics. *Lymphat. Res. Biol.* **5**, 29–43. (doi:10.1089/lrb.2007.5104)

13. Allen JM, McHale NG. 1986 Neuromuscular transmission in bovine mesenteric lymphatics. *Microvasc. Res.* **31**, 77–83. (doi:10.1016/0026-2862(86)90008-7)

14. McHale NG, Roddie IC, Thornbury KD. 1980 Nervous modulation of spontaneous contractions in bovine mesenteric lymphatics. *J. Physiol.* **309**, 461–472. (doi:10.1113/jphysiol.1980.sp013520)

15. Kornuta JA, Nepiyushchikh Z, Gasheva OY, Mukherjee A, David C. In press. Effects of dynamic shear and transmural pressure on wall shear stress sensitivity in collecting lymphatic vessels. **3915**.

16. Gashev AA, Davis MJ, Zawieja DC. 2002 Inhibition of the active lymph pump by flow in rat mesenteric lymphatics and thoracic duct. *J. Physiol.* **540**, 1023–1037. (doi:10.1113/jphysiol.2001.016642)

17. Gashev AA, Zhang R-Z, Muthuchamy M, Zawieja DC, Davis MJ. 2012 Regional Heterogeneity of Length–Tension Relationships in Rat Lymph Vessels. (doi:10.1089/lrb.2011.0013)

18. Zawieja DC. 2009 Contractile physiology of lymphatics. *Lymphat. Res. Biol.* **7**, 87–96. (doi:10.1089/lrb.2009.0007)

19. Kume T. 2015 Lymphatic vessel development: Fluid flow and valve-forming cells. *J. Clin. Invest.* **125**, 2924–2926. (doi:10.1172/JCI83189)

20. Sweet DT *et al.* 2015 Lymph flow regulates collecting lymphatic vessel maturation in vivo. *J. Clin. Invest.* **125**, 2995–3007. (doi:10.1172/JCI79386)

21. Davis MJ, Rahbar E, Gashev AA, Zawieja DC, Moore JE. 2011 Determinants of valve gating in collecting lymphatic vessels from rat mesentery. *Am. J. Physiol. Heart Circ. Physiol.* **301**, H48-60. (doi:10.1152/ajpheart.00133.2011)

22. Stacker S a, Williams SP, Karnezis T, Shayan R, Fox SB, Achen MG. 2014 Lymphangiogenesis and lymphatic vessel remodelling in cancer. *Nat. Rev. Cancer* **14**, 159–172. (doi:10.1038/nrc3677)

23. Mihara M *et al.* In press. Pathological Steps of Cancer-Related Lymphedema: Histological Changes in the Collecting Lymphatic Vessels after Lymphadenectomy. (doi:10.1371/journal.pone.0041126)

24. Taher M, Nakao S, Zandi S, Melhorn MI, Hayes KC, Hafezi-Moghadam A. 2016

Phenotypic transformation of intimal and adventitial lymphatics in atherosclerosis: A regulatory role for soluble VEGF receptor 2. *FASEB J.* **30**, 2490–2499. (doi:10.1096/fj.201500112)

25. Trevaskis NL, McEvoy CL, Mcintosh MP, Edwards GA, Shanker RM, Charman WN, Porter CJH. 2010 The role of the intestinal lymphatics in the absorption of two highly lipophilic cholesterol ester transfer protein inhibitors (CP524,515 and CP532,623). *Pharm. Res.* **27**, 878–893. (doi:10.1007/s11095-010-0083-0)

26. Martel C *et al.* 2013 Lymphatic vasculature mediates macrophage reverse cholesterol transport in mice. *J. Clin. Invest.* **123**, 1571–1579. (doi:10.1172/JCI63685)

27. Klotz L *et al.* 2015 Cardiac lymphatics are heterogeneous in origin and respond to injury. *Nature* **522**, 62–67. (doi:10.1038/nature14483)

28. Cui Y. 2010 The role of lymphatic vessels in the heart. *Pathophysiology*. **17**, 307–314. (doi:10.1016/j.pathophys.2009.07.006)

29. Kholová I, Dragneva G, Čermáková P, Laidinen S, Kaskenpää N, Hazes T, Čermáková E, Šteiner I, Ylä-Herttuala S. 2011 Lymphatic vasculature is increased in heart valves, ischaemic and inflamed hearts and in cholesterol-rich and calcified atherosclerotic lesions. *Eur. J. Clin. Invest.* **41**, 487–497. (doi:10.1111/j.1365-2362.2010.02431.x)

30. Dashkevich A, Bloch W, Antonyan A, Fries JUW, Geissler HJ. 2009 Morphological and quantitative changes of the initial myocardial lymphatics in terminal heart failure. *Lymphat. Res. Biol.* **7**, 21–27. (doi:10.1089/lrb.2008.1010)

31. El-Chemaly S, Pacheco-Rodriguez G, Ikeda Y, Malide D, Moss J. 2009 Lymphatics in idiopathic pulmonary fibrosis: new insights into an old disease. *Lymphat. Res. Biol.* **7**, 197–203. (doi:10.1089/lrb.2009.0014)

32. El-Chemaly S, Levine SJ, Moss J. 2008 Lymphatics in lung disease. In *Annals of the New York Academy of Sciences*, pp. 195–202. (doi:10.1196/annals.1413.017)

33. Das S, Skobe M. 2008 Lymphatic vessel activation in cancer. In *Annals of the New York Academy of Sciences*, pp. 235–241. (doi:10.1196/annals.1413.021)

34. Alitalo a, Detmar M. 2012 Interaction of tumor cells and lymphatic vessels in cancer progression. *Oncogene* **31**, 4499–4508. (doi:10.1038/onc.2011.602)

35. Ran S, Volk L, Hall K, Flister MJ. 2010 Lymphangiogenesis and lymphatic metastasis in breast cancer. *Pathophysiology*. **17**, 229–251. (doi:10.1016/j.pathophys.2009.11.003)

36. Steven Alexander J, Chaitanya GV, Grisham MB, Boktor M. 2010 Emerging roles of lymphatics in inflammatory bowel disease. *Ann. N. Y. Acad. Sci.* **1207**.

(doi:10.1111/j.1749-6632.2010.05757.x)

37. Becker F, Yi P, Al-Kofahi M, Ganta VC, Morris J, Alexander JS. 2014 Lymphatic dysregulation in intestinal inflammation: new insights into inflammatory bowel disease pathomechanisms. *Lymphology* **47**, 3–27.

38. Rockson SG. 2009 The Unique Biology of Lymphatic Edema. *Lymphat. Res. Biol.* **7**, 97–100. (doi:10.1089/lrb.2009.7202)

39. Rockson SG. 2013 The lymphatics and the inflammatory response: lessons learned from human lymphedema. *Lymphat. Res. Biol.* **11**, 117–20. (doi:10.1089/lrb.2013.1132)

40. Rahbar E, Akl T, Coté GL, Moore JE, Zawieja DC. 2014 Lymph transport in rat mesenteric lymphatics experiencing edemagenic stress. *Microcirculation* **21**, 359–367. (doi:10.1111/micc.12112)

41. Bains SK *et al.* 2015 A constitutional predisposition to breast cancer-related lymphoedema and effect of axillary lymph node surgery on forearm muscle lymph flow. *Breast* **24**, 68–74. (doi:10.1016/j.breast.2014.11.010)

42. Liao S *et al.* 2011 Impaired lymphatic contraction associated with immunosuppression. *Proc Natl Acad Sci U S A* **108**, 18784–18789. (doi:10.1073/pnas.1116152108)

43. Warren AG, Brorson H, Borud LJ, Slavin S a. 2007 Lymphedema: a comprehensive review. *Ann. Plast. Surg.* (doi:10.1097/01.sap.0000257149.42922.7e)

44. Red-Horse K. 2008 Lymphatic Vessel Dynamics in the Uterine Wall. *Placenta* **29**, 55–59. (doi:10.1016/j.placenta.2007.11.011)

45. Lachance PA, Hazen A, Sevick-Muraca EM. 2013 Lymphatic vascular response to acute inflammation. *PLoS One* **8**, e76078. (doi:10.1371/journal.pone.0076078\nPONE-D-13-09737 [pii])

46. Slavin SA, Van den Abeele AD, Losken A, Swartz MA, Jain RK. 1999 Return of lymphatic function after flap transfer for acute lymphedema. *Ann. Surg.* **229**, 421–427. (doi:10.1097/00000658-199903000-00017)

47. Oashi K, Furukawa H, Oyama A, Funayama E, Hayashi T, Saito A, Yamamoto Y. 2012 A New Model of Acquired Lymphedema in the Mouse Hind Limb A Preliminary Report. *Ann. Plast. Surg.* **69**, 565–568. (doi:10.1097/SAP.0b013e31821ee3dd)

48. Cheung L, Han J, Beilhack A, Joshi S, Wilburn P, Dua A, An A, Rockson SG. 2006 An experimental model for the study of lymphedema and its response to therapeutic lymphangiogenesis. *Biodrugs* **20**, 363–370. (doi:10.2165/00063030-200620060-00007)

49. Zampell JC, Elhadad S, Avraham T, Weitman E, Aschen S, Yan A, Mehrara BJ. 2012 Toll-like receptor deficiency worsens inflammation and lymphedema after lymphatic injury. *Am. J. Physiol. Physiol.* (doi:10.1152/ajpcell.00284.2011)

50. Avraham T, Zampell JC, Yan A, Elhadad S, Weitman ES, Rockson SG, Bromberg J, Mehrara BJ. 2013 Th2 differentiation is necessary for soft tissue fibrosis and lymphatic dysfunction resulting from lymphedema. *FASEB J.* **27**, 1114–1126.

51. García Nores GD *et al.* 2018 CD4+T cells are activated in regional lymph nodes and migrate to skin to initiate lymphedema. *Nat. Commun.* **9**. (doi:10.1038/s41467-018-04418-y)

52. Savetsky IL, Torrisi JS, Cuzzone DA, Ghanta S, Albano NJ, Gardenier JC, Joseph WJ, Mehrara BJ. 2014 Obesity increases inflammation and impairs lymphatic function in a mouse model of lymphedema. *Am. J. Physiol. Circ. Physiol.* **307**, H165–H172.

53. Zampell JC, Elhadad S, Avraham T, Weitman E, Aschen S, Yan A, Mehrara BJ. 2012 Toll-like receptor deficiency worsens inflammation and lymphedema after lymphatic injury. *Am. J. Physiol. - Cell Physiol.* **302**.

54. Weiler MJ, Cribb MT, Nepiyushchikh Z, Nelson TS, Dixon JB. 2019 A novel mouse tail lymphedema model for observing lymphatic pump failure during lymphedema development. *Sci. Rep.* (doi:10.1038/s41598-019-46797-2)

55. Tobbia D, Semple J, Baker A, Dumont D, Semple A, Johnston M. 2009 Lymphedema development and lymphatic function following lymph node excision in sheep. *J. Vasc. Res.* (doi:10.1159/000194273)

56. Leighton RL, Suter PF. 1979 Primary lymphedema of the hindlimb in the dog. *J. Am. Vet. Med. Assoc.*

57. Honkonen KM, Visuri MT, Tervala T V., Halonen PJ, Koivisto M, Lähteenvuo MT, Alitalo KK, Ylä-Herttuala S, Saaristo AM. 2013 Lymph node transfer and perinodal lymphatic growth factor treatment for lymphedema. *Ann. Surg.* (doi:10.1097/SLA.0b013e31826ed043)

58. Rutkowski JM, Moya M, Johannes J, Goldman J, Swartz MA. 2006 Secondary lymphedema in the mouse tail: Lymphatic hyperplasia, VEGF-C upregulation, and the protective role of MMP-9. *Microvasc. Res.* **72**, 161–171. (doi:10.1016/j.mvr.2006.05.009)

59. Tian W *et al.* 2017 Leukotriene B-4 antagonism ameliorates experimental lymphedema. *Sci. Transl. Med.* **9**. (doi:10.1126/scitranslmed.aal3920)

60. Bertram CD, Macaskill C, Davis MJ, Moore Jr. JE. 2014 Development of a model of a multi-lymphangion lymphatic vessel incorporating realistic and measured parameter values. *Biomech. Model. Mechanobiol.* **13**, 401–416.

(doi:10.1007/s10237-013-0505-0)

61. Bertram CD, Macaskill C, Moore JE. 2011 Simulation of a Chain of Collapsible Contracting Lymphangions With Progressive Valve Closure. *J. Biomech. Eng.* **133**, 011008. (doi:10.1115/1.4002799)

62. Jamalian S, Bertram CD, Richardson WJ, Moore JE. 2013 Parameter sensitivity analysis of a lumped-parameter model of a chain of lymphangions in series. , 1709–1717. (doi:10.1152/ajpheart.00403.2013)

63. Jamalian S, Jafarnejad M, Zawieja SD, Bertram CD, Gashev AA, Zawieja DC, Davis MJ, Moore Jr. JE. 2017 Demonstration and Analysis of the Suction Effect for Pumping Lymph from Tissue Beds at Subatmospheric Pressure. *Sci. Rep.* **7**. (doi:10.1038/s41598-017-11599-x)

64. Bertram CD *et al.* 2016 Consequences of intravascular lymphatic valve properties: a study of contraction timing in a multi-lymphangion model. *Am. J. Physiol. Heart Circ. Physiol.* **310**, H847-60. (doi:10.1152/ajpheart.00669.2015)

65. Jamalian S, Davis MJ, Zawieja DC, Moore JE. 2016 Network Scale Modeling of Lymph Transport and Its Effective Pumping Parameters. *PLoS One* **11**, e0148384. (doi:10.1371/journal.pone.0148384)

66. Kunert C, Baish JW, Liao S, Padera TP, Munn LL. 2015 Mechanobiological oscillators control lymph flow -- revised. *Nature* , 14–17. (doi:10.1073/pnas.1508330112)

67. Baish JW, Kunert C, Padera TP, Munn LL. 2016 Synchronization and Random Triggering of Lymphatic Vessel Contractions. *PLOS Comput. Biol.* **12**, e1005231. (doi:10.1371/journal.pcbi.1005231)

68. Margaris KN, Black R a. 2012 Modelling the lymphatic system : challenges and opportunities. *J R Soc Interface* **9**, 601–612. (doi:10.1098/rsif.2011.0751)

69. Grande KJ, Cochran RP, Reinhall PG, Kunzelma KS. 1998 Stress variations in the human aortic root and valve: The role of anatomic asymmetry. *Ann. Biomed. Eng.* **26**, 534–545. (doi:10.1114/1.122)

70. Caulk AW, Nepiyushchikh Z V., Shaw R, Dixon JB, Gleason RL. 2015 Quantification of the passive and active biaxial mechanical behaviour and microstructural organization of rat thoracic ducts. *J. R. Soc. Interface* **12**, 20150280. (doi:10.1098/rsif.2015.0280)

71. Caulk AW, Dixon · J Brandon, Gleason RL. In press. A lumped parameter model of mechanically mediated acute and long-term adaptations of contractility and geometry in lymphatics for characterization of lymphedema. *Biomech. Model. Mechanobiol.* (doi:10.1007/s10237-016-0785-2)

72. Kunert C, Baish JW, Liao S, Padera TP, Munn LL. 2015 Reply to Davis: Nitric oxide regulates lymphatic contractions. *Proc. Natl. Acad. Sci.* **113**, E106–E106. (doi:10.1073/pnas.1522233113)

73. Davis MJ. 2015 Is nitric oxide important for the diastolic phase of the lymphatic contraction/relaxation cycle? *Proc. Natl. Acad. Sci.* **113**, E105–E105. (doi:10.1073/pnas.1521707113)

74. Razavi MS, Nelson TS, Nepiyushchikh Z, Gleason RL, Dixon JB. 2017 The relationship between lymphangion chain length and maximum pressure generation established through in vivo imaging and computational modeling. *Am. J. Physiol. Circ. Physiol.* **313**, H1249–H1260. (doi:10.1152/ajpheart.00003.2017)

75. Caulk AW, Nepiyushchikh Z V, Shaw R, Dixon JB, Gleason Jr. RL. 2015 Quantification of the passive and active biaxial mechanical behaviour and microstructural organization of rat thoracic ducts. *J. R. Soc. Interface* **12**. (doi:10.1098/rsif.2015.0280)

76. Eisenhoffer J, Kagal a, Klein T, Johnston MG. 1995 Importance of valves and lymphangion contractions in determining pressure gradients in isolated lymphatics exposed to elevations in outflow pressure. *Microvasc. Res.* **49**, 97–110. (doi:10.1006/mvre.1995.1008)

77. Gashev, Anatoliy; David Z. 2001 Physiology of Human Lymphatic Contractions.

78. Weid P Von Der, Zawieja DC. 2004 Lymphatic smooth muscle : the motor unit of lymph drainage. **36**, 1147–1153. (doi:10.1016/j.biocel.2003.12.008)

79. Chakraborty S, Davis MJ, Muthuchamy M. 2015 Emerging trends in the pathophysiology of lymphatic contractile function. *Semin. Cell Dev. Biol.* **38**, 55–66. (doi:10.1016/j.semcdb.2015.01.005)

80. Mizuno R, Dornyei G, Koller A, Kaley G. 1997 Myogenic responses of isolated lymphatics: modulation by endothelium. *Microcirculation* **4**, 413–420.

81. Gleason RL, Gray SP, Wilson E, Humphrey JD. 2004 A multiaxial computer-controlled organ culture and biomechanical device for mouse carotid arteries. *J. Biomech. Eng.* **126**, 787–795. (doi:10.1115/1.1824130)

82. Gashev A a *et al.* 2009 Methods for lymphatic vessel culture and gene transfection. *Microcirculation* **16**, 615–628. (doi:10.1080/10739680903120778)

83. Bredfeldt JS *et al.* 2014 Computational segmentation of collagen fibers from second-harmonic generation images of breast cancer. *J. Biomed. Opt.* **19**, 016007. (doi:10.1117/1.JBO.19.1.016007)

84. Carpenter AE *et al.* 2006 CellProfiler: Image analysis software for identifying and quantifying cell phenotypes. *Genome Biol.* (doi:10.1186/gb-2006-7-10-r100)

85. Hayashi a, Johnston MG, Nelson W, Hamilton S, McHale NG. 1987 Increased intrinsic pumping of intestinal lymphatics following hemorrhage in anesthetized sheep. *Circ. Res.* **60**, 265–72. (doi:10.1161/01.RES.60.2.265)

86. Boulanger BR, Lloyd SJ, Walker M, Johnston MG. 1994 Intrinsic pumping of mesenteric lymphatics is increased after hemorrhage in awake sheep. *Circ Shock* **43**, 95–101.

87. Davis MJ, Scallan JP, Wolpers JH, Muthuchamy M, Gashev AA, Zawieja DC. 2012 Intrinsic increase in lymphangion muscle contractility in response to elevated afterload. *Am. J. Physiol. Circ. Physiol.* **303**, H795–H808. (doi:10.1152/ajpheart.01097.2011)

88. Stewart H, Dongaonkar RM, Nguyen TL, Quick CM, Hardy J, Laine GA, Wilson E. 2013 changes in transmural pressure Adaptation of mesenteric lymphatic vessels to prolonged. *Am J Physiol Hear. Circ Physiol Am. J. Physiol. -Heart Circ. Physiol.* **305**, 203–210. (doi:10.1152/ajpheart.00677.2012)

89. Shirasawa Y, Benoit JN. 2003 Stretch-induced calcium sensitization of rat lymphatic smooth muscle. *Am. J. Physiol. Circ. Physiol.* **285**, H2573–H2577. (doi:10.1152/ajpheart.00002.2003)

90. Davis MJ, Davis AM, Lane MM, Ku CW, Gashev AA. 2009 Rate-sensitive contractile responses of lymphatic vessels to circumferential stretch. *J. Physiol.* **587**, 165–182. (doi:10.1113/jphysiol.2008.162438)

91. von der Weid P-Y, Lee S, Imtiaz MS, Zawieja DC, Davis MJ. 2014 Electrophysiological Properties of Rat Mesenteric Lymphatic Vessels and their Regulation by Stretch. *Lymphat. Res. Biol.* **12**, 66–75. (doi:10.1089/lrb.2013.0045)

92. Telinius N, Majgaard J, Mohanakumar S, Pahle E, Nielsen J, Hjortdal V, Aalkjaer C, Boedtkjer DB. 2017 Spontaneous and Evoked Contractility of Human Intestinal Lymphatic Vessels. *Lymphat. Res. Biol.* **15**, 17–22. (doi:10.1089/lrb.2016.0039)

93. Gashev AA. 2008 Lymphatic vessels: Pressure- and flow-dependent regulatory reactions. *Ann. N. Y. Acad. Sci.* **1131**, 100–109. (doi:10.1196/annals.1413.009)

94. Dongaonkar RM, Stewart RH, Laine G, Davis MJ, Zawieja DC, Quick CM. 2009 Venomotion modulates lymphatic pumping in the bat wing. *Am. J. Physiol. Hear. Circ. Physiol.* **296**, H2015-21. (doi:10.1152/ajpheart.00418.2008)

95. Hargens a R, Zweifach BW. 1977 Contractile stimuli in collecting lymph vessels. *Am. J. Physiol.* **233**, H57-65. (doi:10.1152/ajpheart.1977.233.1.H57)

96. McHale NG, Roddie IC. 1976 The effect of transmural pressure on pumping activity in isolated bovine lymphatic vessels. *J. Physiol.* **261**, 255–269. (doi:10.1113/jphysiol.1976.sp011557)

97. GASHEV* AA, DAVIS* MJ, DELP† MD, ZAWIEJA* DC. 2004 Regional Variations of Contractile Activity in Isolated Rat Lymphatics. *Microcirculation* **11**, 477–492. (doi:10.1080/10739680490476033)

98. Zhang R, Gashev AA, Zawieja DC, Davis MJ. 2007 Length-tension relationships of small arteries, veins, and lymphatics from the rat mesenteric microcirculation. *Am. J. Physiol. Circ. Physiol.* **292**, H1943–H1952. (doi:10.1152/ajpheart.01000.2005)

99. Ferguson M, Williams U, Leff A, Mitchell R. 1993 Length-tension characteristics of bovine tracheobronchial lymphatic smooth muscle. *Lymphology* **26**, 19.

100. Gashev AA, Zhang R-Z, Muthuchamy M, Zawieja DC, Davis MJ. 2012 Regional Heterogeneity of Length–Tension Relationships in Rat Lymph Vessels. *Lymphat. Res. Biol.* **10**, 14–19. (doi:10.1089/lrb.2011.0013)

101. Abu-Hijleh MF, Habbal OA, Moqattash ST. 1995 The role of the diaphragm in lymphatic absorption from the peritoneal cavity. *J. Anat.* **186 (Pt 3**, 453–67.

102. Negrini D, Moriondo A. 2013 Pleural function and lymphatics. *Acta Physiol.* **207**, 244–259. (doi:10.1111/apha.12016)

103. Davis MJ, Davis AM, Ku CW, Gashev AA. 2009 Myogenic constriction and dilation of isolated lymphatic vessels. *Am. J. Physiol. Circ. Physiol.* **296**, H293–H302. (doi:10.1152/ajpheart.01040.2008)

104. McHale NG, Allen JM. 1983 The effect of external Ca2+ concentration on the contractility of bovine mesenteric lymphatics. *Microvasc. Res.* **26**, 182–192. (doi:10.1016/0026-2862(83)90069-9)

105. Souza-Smith FM, Kurtz KM, Molina PE, Breslin JW. 2010 Adaptation of mesenteric collecting lymphatic pump function following acute alcohol intoxication. *Microcirculation* **17**, 514–524. (doi:10.1111/j.1549-8719.2010.00050.x)

106. Telinius N, Majgaard J, Kim S, Katballe N, Pahle E, Nielsen J, Hjortdal V, Aalkjaer C, Boedtkjer DB. 2015 Voltage-gated sodium channels contribute to action potentials and spontaneous contractility in isolated human lymphatic vessels. *J. Physiol.* **593**, 3109–3122. (doi:10.1113/jp270166)

107. Lee S, Roizes S, von der Weid P-Y. 2014 Distinct roles of L- and T-type voltage-dependent Ca2+ channels in regulation of lymphatic vessel contractile activity. *J. Physiol.* **592**, 5409–5427. (doi:10.1113/jphysiol.2014.280347)

108. Atchison DJ, Johnston MG. 1997 Role of extra- and intracellular Ca2+ in the lymphatic myogenic response. *Am. J. Physiol. Integr. Comp. Physiol.* **272**, R326–R333.

109. Ohtani Y, Ohtani O. 2001 Postnatal development of lymphatic vessels and their

smooth muscle cells in the rat diaphragm: a confocal microscopic study. *Arch. Histol. Cytol.* (doi:10.1679/aohc.64.513)

110. Von Der Weid PY. 2001 Review article: lymphatic vessel pumping and inflammation - the role of spontaneous constrictions and underlying electrical pacemaker potentials. *Aliment. Pharmacol. Ther.* **15**, 1115–1129. (doi:10.1046/j.1365-2036.2001.01037.x)

111. Moriondo A, Solari E, Marcozzi C, Negrini D. 2013 Spontaneous activity in peripheral diaphragmatic lymphatic loops. *Am. J. Physiol. Circ. Physiol.* **305**, H987–H995. (doi:10.1152/ajpheart.00418.2013)

112. Telinius N, Drewsen N, Pilegaard H, Kold-Petersen H, de Leval M, Aalkjaer C, Hjortdal V, Boedtkjer DB. 2010 Human thoracic duct in vitro: diameter-tension properties, spontaneous and evoked contractile activity. *Am. J. Physiol. Circ. Physiol.* **299**, H811–H818. (doi:10.1152/ajpheart.01089.2009)

113. Lee SH, Wen HJ, Shen CL. 1993 Ultrastructure of the monkey thoracic duct and the cisterna chyli. *J. Anat.* **182 (Pt 2**, 205–12. (doi:10.1088/0963-0252/22/2/025020)

114. Athanasiou D *et al.* 2017 The passive biomechanics of human pelvic collecting lymphatic vessels. *PLoS One* **12**, 1–12. (doi:10.1371/journal.pone.0183222)

115. Rahbar E, Weimer J, Gibbs H, Yeh AT, Bertram CD, Davis MJ, Hill MA, Zawieja DC, Moore Jr. JE. 2012 Passive Pressure-Diameter Relationship and Structural Composition of Rat Mesenteric Lymphangions. *Lymphat. Res. Biol.* **10**, 152–163. (doi:10.1089/lrb.2011.0015)

116. Arkill KP, Moger J, Winlove CP. 2010 The structure and mechanical properties of collecting lymphatic vessels: An investigation using multimodal nonlinear microscopy. *J. Anat.* **216**, 547–555. (doi:10.1111/j.1469-7580.2010.01215.x)

117. Davis MJ, Davis AM, Lane MM, Ku CW, Gashev AA. 2009 Rate-sensitive contractile responses of lymphatic vessels to circumferential stretch. *J. Physiol.* **587**, 165–182. (doi:10.1113/jphysiol.2008.162438)

118. Davis MJ, Rahbar E, Gashev AA, Zawieja DC, Moore Jr. JE. 2011 Determinants of valve gating in collecting lymphatic vessels from rat mesentery. *Am. J. Physiol. Circ. Physiol.* **301**, H48–H60. (doi:10.1152/ajpheart.00133.2011)

119. Chakraborty S, Zawieja S, Wang W, Zawieja DC, Muthuchamy M. 2010 Lymphatic system: a vital link between metabolic syndrome and inflammation. In *Lymphatics in the Digestive System: Physiology, Health, and Disease*, pp. E94–E102. (doi:10.1111/j.1749-6632.2010.05752.x)

120. Ohhashi T, Azuma T, Sakaguchi M. 1980 Active and passive mechanical characteristics of bovine mesenteric lymphatics. *Am. J. Physiol.* **239**, H88-95.

121. Scallan JP, Wolpers JH, Davis MJ. 2013 Constriction of isolated collecting lymphatic vessels in response to acute increases in downstream pressure. *J. Physiol.* **591**, 443–59. (doi:10.1113/jphysiol.2012.237909)

122. Gashev AA, Zhang R-Z, Muthuchamy M, Zawieja DC, Davis MJ. 2012 Regional Heterogeneity of Length-Tension Relationships in Rat Lymph Vessels. *Lymphat. Res. Biol.* **10**, 14–19. (doi:10.1089/lrb.2011.0013)

123. Zhang R, Gashev AA, Zawieja DC, Lane MM, Davis MJ. 2007 Length-Dependence of Lymphatic Phasic Contractile Activity Under Isometric and Isobaric Conditions. *Microcirculation* **14**, 613–625. (doi:10.1080/10739680701436160)

124. Gashev AA. 2002 Physiologic aspects of lymphatic contractile function: current perspectives. *Ann. N. Y. Acad. Sci.* **979**, 178–187; discussion 188-196. (doi:10.1111/j.1749-6632.2002.tb04878.x)

125. Gasheva OY, Zawieja DC, Gashev A a. 2006 Contraction-initiated NO-dependent lymphatic relaxation: a self-regulatory mechanism in rat thoracic duct. *J. Physiol.* **575**, 821–32. (doi:10.1113/jphysiol.2006.115212)

126. Bakker EN, Sipkema P. 1997 Components of acetylcholine-induced dilation in isolated rat arterioles. *Am. J. Physiol.* **273**, H1848-53.

127. Nizamutdinova IT, Maejima D, Nagai T, Meininger CJ, Gashev AA. 2017 Histamine as an Endothelium-Derived Relaxing Factor in Aged Mesenteric Lymphatic Vessels. *Lymphat. Res. Biol.* **15**, 136–145. (doi:10.1089/lrb.2016.0062)

128. von der Weid PY. 1998 ATP-sensitive K+ channels in smooth muscle cells of guinea-pig mesenteric lymphatics: role in nitric oxide and beta-adrenoceptor agonist-induced hyperpolarizations. *Br. J. Pharmacol.* **125**, 17–22. (doi:10.1038/sj.bjp.0702026)

129. Imtiaz MS, Zhao J, Hosaka K, von der Weid P-Y, Crowe M, van Helden DF. 2007 Pacemaking through Ca2+ stores interacting as coupled oscillators via membrane depolarization. *Biophys. J.* **92**, 3843–3861. (doi:10.1526/biophysj.106.095687)

130. Gashev AA, Zawieja DC. 2010 Hydrodynamic regulation of lymphatic transport and the impact of aging. *Pathophysiol. Off. J. Int. Soc. Pathophysiol.* **17**, 277–287. (doi:10.1016/j.pathophys.2009.09.002)

131. Bohlen HG, Gasheva OY, Zawieja DC. 2011 Nitric oxide formation by lymphatic bulb and valves is a major regulatory component of lymphatic pumping. *Am. J. Physiol. Heart Circ. Physiol.* **301**, H1897-906. (doi:10.1152/ajpheart.00260.2011)

132. Scallan JP, Davis MJ. 2013 Genetic removal of basal nitric oxide enhances contractile activity in isolated murine collecting lymphatic vessels. *J. Physiol.* **591**, 2139–56. (doi:10.1113/jphysiol.2012.250662)

133. Mizuno R, Koller a, Kaley G. 1998 Regulation of the vasomotor activity of lymph microvessels by nitric oxide and prostaglandins. *Am. J. Physiol.* **274**, R790-6.

134. Gashev A a, Davis MJ, Delp MD, Zawieja DC. 2004 Regional variations of contractile activity in isolated rat lymphatics. *Microcirculation* **11**, 477–92. (doi:10.1080/10739680490476033)

135. Kornuta JA, Nepiyushchikh Z, Gasheva OY, Mukherjee A, Zawieja DC, Dixon JB. 2015 Effects of dynamic shear and transmural pressure on wall shear stress sensitivity in collecting lymphatic vessels. *Am. J. Physiol. Integr. Comp. Physiol.* **309**, R1122–R1134. (doi:10.1152/ajpregu.00342.2014)

136. Gashev AA, Davis MJ, Zawieja DC. 2002 Inhibition of the active lymph pump by flow in rat mesenteric lymphatics and thoracic duct. *J. Physiol.* **540**, 1023–1037. (doi:10.1113/jphysiol.2002.016642)

137. Elias RM, Johnston MG. 1990 Modulation of lymphatic pumping by lymph-borne factors after endotoxin administration in sheep. *J. Appl. Physiol.* **68**, 199–208.

138. Ferguson MK, Defilippi VJ. 1994 NITRIC-OXIDE AND ENDOTHELIUM-DEPENDENT RELAXATION IN TRACHEOBRONCHIAL LYMPH VESSELS. *Microvasc. Res.* **47**, 308–317. (doi:10.1006/mvre.1994.1024)

139. Shirasawa Y, Ikomi F, Ohhashi T. 2000 Physiological roles of endogenous nitric oxide in lymphatic pump activity of rat mesentery in vivo. *Am. J. Physiol. Liver Physiol.* **278**, G551–G556.

140. vonderWeid PY, Crowe MJ, VanHelden DF. 1996 Endothelium-dependent modulation of pacemaking in lymphatic vessels of the guinea-pig mesentery. *J. Physiol.* **493**, 563–575. (doi:10.1113/jphysiol.1996.sp021404)

141. Yokoyama S, Ohhashi T. 1993 Effects of acetylcholine on spontaneous contractions in isolated bovine mesenteric lymphatics. *Am J Physiol* **264**, H1460-4.

142. Hagendoorn J *et al.* 2004 Endothelial nitric oxide synthase regulates microlymphatic flow via collecting lymphatics. *Circ. Res.* **95**, 204–209. (doi:10.1161/01.RES.0000135549.72828.24)

143. Liao S *et al.* 2011 Impaired lymphatic contraction associated with immunosuppression. *Proc. Natl. Acad. Sci.* **108**, 18784–18789. (doi:10.1073/pnas.1116152108)

144. Datar SA *et al.* 2014 Altered reactivity and nitric oxide signaling in the isolated thoracic duct from an ovine model of congenital heart disease with increased pulmonary blood flow. *Am J Physiol Hear. Circ Physiol* **306**, H954-62. (doi:10.1152/ajpheart.00841.2013)

145. Walter U. 1989 PHYSIOLOGICAL-ROLE OF CGMP AND CGMP-DEPENDENT

PROTEIN-KINASE IN THE CARDIOVASCULAR-SYSTEM. *Rev. Physiol. Biochem. Pharmacol.* **113**, 41–88.

146. Aratow M, Hargens AR, Meyer JU, Arnaud SB. 1991 POSTURAL RESPONSES OF HEAD AND FOOT CUTANEOUS MICROVASCULAR FLOW AND THEIR SENSITIVITY TO BED REST. *Aviat. Sp. Environ. Med.* **62**, 246–251.

147. Warner TD, Mitchell JA, Sheng H, Murad F. 1994 Effects of cyclic GMP on smooth muscle relaxation. *Adv. Pharmacol.* **26**, 171–194. (doi:10.1016/s1054-3589(08)60054-x)

148. OHHASHI. 1994 Nitric Oxide and the Lymphatic System. *Japanses J. Physiol.* (doi:10.2170/jjphysiol.44.327)

149. Gasheva OY, Gashev AA, Zawieja DC. 2013 Cyclic guanosine monophosphate and the dependent protein kinase regulate lymphatic contractility in rat thoracic duct. *J. Physiol.* **591**, 4549–4565. (doi:10.1113/jphysiol.2013.258681)

150. Bohlen HG, Zhou X, Unthank JL, Miller SJ, Bills R. 2009 Transfer of nitric oxide by blood from upstream to downstream resistance vessels causes microvascular dilation. *Am. J. Physiol. Circ. Physiol.* **297**, H1337–H1346. (doi:10.1152/ajpheart.00171.2009)

151. Sunemoto HT, Komi FI, Hhashi TO. 2003 Flow-Mediated Release of Nitric Oxide from Lymphatic Endothelial Cells of Pressurized Canine Thoracic Duct. **53**, 157–163.

152. Gashev AA, Davis MJ, Zawieja DC. 2002 Inhibition of the active lymph pump by flow in rat mesenteric lymphatics and thoracic duct. *J. Physiol.* **540**, 1023–1037. (doi:10.1113/jphysiol.2002.016642)

153. Kesler CT, Liao S, Munn LL, Padera TP. 2013 Lymphatic vessels in health and disease. *Wiley Interdiscip. Rev. Syst. Biol. Med.* **5**, 111–124. (doi:10.1002/wsbm.1201)

154. Grossi L, D'Angelo S. 2005 Sodium nitroprusside: Mechanism of NO release mediated by sulfhydryl-containing molecules. *J. Med. Chem.* **48**, 2622–2626. (doi:10.1021/jm049857n)

155. Kurtz KH, Moor AN, Souza-Smith FM, Breslin JW. 2014 Involvement of H1 and H2 receptors and soluble guanylate cyclase in histamine-induced relaxation of rat mesenteric collecting lymphatics. *Microcirculation* **21**, 593–605. (doi:10.1111/micc.12138)

156. Torrisi JS *et al.* 2016 Inhibition of Inflammation and iNOS Improves Lymphatic Function in Obesity. *Sci. Rep.* **6**, 1–12. (doi:10.1038/srep19817)

157. Breslin JW, Yang Y, Scallan JP, Sweat RS, Adderley SP, Murfee WL. 2018

Lymphatic Vessel Network Structure and Physiology. *Compr. Physiol.* **9**, 207–299. (doi:10.1002/cphy.c180015)

158. Muthuchamy M, Zawieja D. 2008 Molecular regulation of lymphatic contractility. In *Annals of the New York Academy of Sciences*, pp. 89–99. (doi:10.1196/annals.1413.008)

159. Scallan JP, Wolpers JH, Davis MJ. 2013 Constriction of isolated collecting lymphatic vessels in response to acute increases in downstream pressure. *J. Physiol.* **591**, 443–459. (doi:10.1113/jphysiol.2012.237909)

160. Wan W, Yanagisawa H, Gleason Jr RL. 2010 Biomechanical and Microstructural Properties of Common Carotid Arteries from Fibulin-5 Null Mice. (doi:10.1007/s10439-010-0114-3)

161. Caulk AW, Dixon JB, Gleason RL. 2016 A lumped parameter model of mechanically mediated acute and long-term adaptations of contractility and geometry in lymphatics for characterization of lymphedema. *Biomech. Model. Mechanobiol.* , 1–18. (doi:10.1007/s10237-016-0785-2)

162. Ferruzzi J, Bersi MR, Humphrey JD. 2013 Biomechanical phenotyping of central arteries in health and disease: Advantages of and methods for murine models. *Ann. Biomed. Eng.* (doi:10.1007/s10439-013-0799-1)

163. Ferruzzi J, Vorp D a, Humphrey JD. 2011 On constitutive descriptors of the biaxial mechanical behaviour of human abdominal aorta and aneurysms. *J. R. Soc. Interface* **8**, 435–450. (doi:10.1098/rsif.2010.0299)

164. Yin FC, Chew PH, Zeger SL. 1986 An Approach to Quantification Stress-Strain of Biaxial Tissue Data. *J Biomech* **19**, 27–37.

165. Kamenskiy A, Seas A, Deegan P, Poulson W, Anttila E, Sim S, Desyatova A, MacTaggart J. 2017 Constitutive description of human femoropopliteal artery aging. *Biomech. Model. Mechanobiol.* **16**, 681–692. (doi:10.1007/s10237-016-0845-7)

166. DiCiccio TJ, Efron B. 1996 Bootstrap confidence intervals. *Stat. Sci.* , 189–212.

167. Davison AC, Hinkley DV. 1997 *Bootstrap methods and their application*. Cambridge university press.

168. Mohammad S. Razavi , Julie Leonard-Duke , Rebecca Hardie, J. Brandon Dixon RG. 2019 Axial Stretch Modulates Lymphatic Contractility: Organization of Lymphatic Smooth Muscle Cells and Collagen Fibers in Collecting Lymphatic Vessels from Rat Tail. *Sci. Reports (Under Rev.*

169. Baek S, Gleason RL, Rajagopal KR, Humphrey JD. 2007 Theory of small on large: Potential utility in computations of fluid-solid interactions in arteries. *Comput. Methods Appl. Mech. Eng.* **196**, 3070–3078. (doi:10.1016/j.cma.2006.06.018)

170. Scallan JP, Davis MJ. 2013 Genetic removal of basal nitric oxide enhances contractile activity in isolated murine collecting lymphatic vessels. *J. Physiol.* **591**, 2139–2156. (doi:10.1113/jphysiol.2012.250662)

171. Chatterjee V, Gashev AA. 2014 Mast Cell-Directed Recruitment of MHC Class II Positive Cells and Eosinophils Towards Mesenteric Lymphatic Vessels in Adulthood and Elderly. *Lymphat. Res. Biol.* **12**, 37–47. (doi:10.1089/lrb.2013.0031)

172. Razavi M, Nelson TS, Nepiyushchikh Z, Gleason RL, Dixon JB. 2017 The relationship between lymphangion chain length and maximum pressure generation established through in vivo imaging and computational modeling. *Am. J. Physiol. - Hear. Circ. Physiol.* , ajpheart.00003.2017. (doi:10.1152/ajpheart.00003.2017)

173. Weiler M, Kassis T, Dixon JB. 2012 Sensitivity analysis of near-infrared functional lymphatic imaging. *Opt. Diagnostics Sens. XII Towar. Point-of-Care Diagnostics; Des. Perform. Valid. Phantoms Used Conjunction with Opt. Meas. Tissue IV* **8229**, 82290A. (doi:10.1117/12.906447)

174. Bertram CD, Macaskill C, Moore Jr. JE. 2011 Simulation of a Chain of Collapsible Contracting Lymphangions With Progressive Valve Closure. *J. Biomech. Eng. Asme* **133**. (doi:10.1115/1.4002799)

175. Bertram CD, Macaskill C, Davis MJ, Moore JE. 2014 Development of a model of a multi-lymphangion lymphatic vessel incorporating realistic and measured parameter values. *Biomech. Model. Mechanobiol.* **13**, 401–416. (doi:10.1007/s10237-013-0505-0)

176. Taylor P, Bertram CD, Macaskill C, Jr JEM. 2006 Computer Methods in Biomechanics and Biomedical Engineering Incorporating measured valve properties into a numerical model of a lymphatic vessel. , 37–41. (doi:10.1080/10255842.2012.753066)

177. Nelson TS, Akin RE, Weiler MJ, Kassis T, Kornuta JA, Dixon JB. 2014 Minimally invasive method for determining the effective lymphatic pumping pressure in rats using near-infrared imaging. *Am. J. Physiol. Integr. Comp. Physiol.* (doi:10.1152/ajpregu.00369.2013)

178. Weiler M, Kassis T, Dixon JB. 2012 Sensitivity analysis of near-infrared functional lymphatic imaging. *Opt. Diagnostics Sens. XII Towar. Point-of-Care Diagnostics; Des. Perform. Valid. Phantoms Used Conjunction with Opt. Meas. Tissue IV* **8229**, 82290A. (doi:10.1117/12.906447)

179. Davis MJ, Scallan JP, Wolpers JH, Muthuchamy M, Gashev AA, Zawieja DC. 2012 Intrinsic increase in lymphangion muscle contractility in response to elevated afterload. *Am. J. Physiol. Circ. Physiol.* **303**, H795–H808. (doi:10.1152/ajpheart.01097.2011)

180. Gashev AA, Davis MJ, Delp MD, Zawieja DC. 2004 Regional variations of

contractile activity in isolated rat lymphatics. *Microcirculation* **11**, 477–492. (doi:10.1080/10739680490476033\nCNFRNP6UXERYYRUV [pii])

181. Scallan JP, Davis MJ. 2013 Genetic removal of basal nitric oxide enhances contractile activity in isolated murine collecting lymphatic vessels. *J. Physiol.* **591**, 2139–2156. (doi:10.1113/jphysiol.2012.250662)

182. Kwon S, Agollah GD, Wu G, Sevick-Muraca EM. 2014 Spatio-temporal changes of lymphatic contractility and drainage patterns following lymphadenectomy in mice. *PLoS One* (doi:10.1371/journal.pone.0106034)

183. Saul ME, Thomas PA, Dosen PJ, Isbister GK, O'Leary MA, Whyte IM, McFadden SA, Van Helden DF. 2011 A pharmacological approach to first aid treatment for snakebite. *Nat. Med.* (doi:10.1038/nm.2382)

184. Weiler M, Dixon JB. 2013 Differential transport function of lymphatic vessels in the rat tail model and the long-term effects of indocyanine green as assessed with near-infrared imaging. *Front. Physiol.* (doi:10.3389/fphys.2013.00215)

185. Duran WN, Breslin JW, Sanchez FA. 2010 The NO cascade, eNOS location, and microvascular permeability. *Cardiovasc. Res.* **87**, 254–261. (doi:10.1093/cvr/cvq139)

186. Cintolesi V *et al.* 2016 Constitutively Enhanced Lymphatic Pumping in the Upper Limbs of Women Who Later Develop Breast Cancer-Related Lymphedema. **14**, 50–61. (doi:10.1089/lrb.2016.0005)

187. Unno N, Nishiyama M, Suzuki M, Tanaka H, Yamamoto N, Sagara D, Mano Y, Konno H. 2010 A novel method of measuring human lymphatic pumping using indocyanine green fluorescence lymphography. *J. Vasc. Surg.* (doi:10.1016/j.jvs.2010.04.067)

188. Surgery P, Surgery R. 2017 Lymphedema : A comprehensive review. (doi:10.1097/01.sap.0000257149.42922.7e)

189. Kataru RP, Baik JE, Park HJ, Wiser I, Rehal S, Shin JY, Mehrara BJ. 2019 Regulation of Immune Function by the Lymphatic System in Lymphedema. *Front. Immunol.* **10**, 470. (doi:10.3389/fimmu.2019.00470)

190. Rockson SG, Keeley V, Kilbreath S, Szuba A, Towers A. 2019 Cancer-associated secondary lymphoedema. *Nat. Rev. Dis. Prim.* **5**. (doi:10.1038/s41572-019-0072-5)

191. Hayes SC, Janda M, Cornish B, Battistutta D, Newman B. 2008 Lymphedema after breast cancer: Incidence, risk factors, and effect on upper body function. *J. Clin. Oncol.* **26**, 3536–3542. (doi:10.1200/JCO.2007.14.4899)

192. Rutkowski JM, Moya M, Johannes J, Goldman J, Swartz MA. 2006 Secondary lymphedema in the mouse tail: Lymphatic hyperplasia, VEGF-C upregulation, and

the protective role of MMP-9. *Microvasc. Res.* (doi:10.1016/j.mvr.2006.05.009)

193. Aschen S, Zampell JC, Elhadad S, Weitman E, De Brot M, Mehrara BJ. 2012 Regulation of Adipogenesis by Lymphatic Fluid Stasis: Part II. Expression of Adipose Differentiation Genes. *Plast. Reconstr. Surg.* **129**, 838–847. (doi:10.1097/PRS.0b013e3182450b47)

194. Stanton AWBB, Modi S, Mellor RH, Levick JR, Mortimer PS. 2009 Recent advances in breast cancer-related lymphedema of the arm: lymphatic pump failure and predisposing factors. *Lymphat. Res. Biol.* **7**, 29–45. (doi:10.1089/lrb.2008.1026)

195. Rockson SG, Rivera KK. 2008 Estimating the population burden of lymphedema. In *Annals of the New York Academy of Sciences*, pp. 147–154. (doi:10.1196/annals.1413.014)

196. Mehrara BJ, Zampell JC, Suami H, Chang DW. 2011 Surgical management of lymphedema: past, present, and future. *Lymphat. Res. Biol.* **9**, 159–167.

197. Breslin JW, Yang Y, Scallan JP, Sweat RS, Adderley SP, Murfee WL. 2018 Lymphatic Vessel Network Structure and Physiology. *Compr. Physiol.* **9**, 207–299. (doi:10.1002/cphy.c180015)